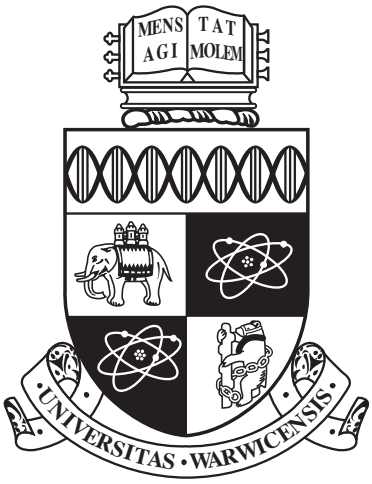

Efficient simulation of internal multiscale gas flows

by

Alexander Patronis

Thesis

Submitted to the University of Warwick

for the degree of

Doctor of Philosophy

School of Engineering

April 2015

WARWICK

Contents

List of Tables

List of Figures

Acknowledgments

First and foremost, I would like to thank my supervisor, Duncan Lockerby, for his invaluable support, general ability, and willingness to humour my critique of his figures. Without his help and patience this work would have just been OK.

I am also grateful for the support of colleagues at various institutions – in particular, thanks to Craig White for developing and providing the dsmcFoam source code, to Matthew Borg for his general help with all things OpenFOAM, and to Dave Stephenson for his wise words and surprisingly good memory.

I thank Nicolas Hadjiconstantinou and Gregg Radtke for providing the source code of the low-variance deviational simulation Monte Carlo method.

I also thank Marcos Rojas-Cárdenas, Irina Graur, Pierre Perrier, and J. Gilbert Méolans for providing raw experimental data for the purposes of validation.

Finally, I owe special gratitude to my family for their continuous and unconditional love and support: to my mother for her overly-optimistic attitude, to my father for the interest he feigned in my research, to my sister for being a constant source of concern, and to Laura for her encouragement and mushroom Stroganoff.

The author's work has been supported by the Engineering and Physical Sciences Research Council (EPSRC) grants EP/I011927/1 and EP/K038664/1.

Declarations

This thesis is submitted to the University of Warwick in support of my application for the degree of Doctor of Philosophy. It has been composed by myself and has not been submitted in any previous application for any degree. The work presented (including data generated and data analysis) was carried out by the author.

Parts of this thesis have been published by the author:

The multiscale and numerical methodology of Chapter 2 is published in

A. Patronis and D. A. Lockerby. Multiscale simulation of non-isothermal microchannel gas flows. *Journal of Computational Physics*, 270:532–543, 2014

A. Patronis, D. A. Lockerby, M. K. Borg, and J. M. Reese. Hybrid continuum-molecular modelling of multiscale internal gas flows. *Journal of Computational Physics*, 255:558–571, 2013

A. Patronis and D. A. Lockerby. Multiscale simulation of Knudsen-pump channel flows, *12th International Conference on Nanochannels, Microchannels, and Minichannels, 2014, Chicago, USA.*

A. Patronis, D. A. Lockerby, M. K. Borg, and J. M. Reese. Multiscale simulation of internal rarefied gas flows, *11th International Conference on Nanochannels, Microchannels, and Minichannels, 2013, Sapporo, Japan.*

The multiscale and numerical methodology of Chapter 4 is published in

D. A. Lockerby, A. Patronis, M. K. Borg, and J. M. Reese. Asynchronous coupling of hybrid models for efficient simulation of multiscale systems. *Journal of Computational Physics*, 284:261–272, 2015

Abstract

We develop, validate, and apply an efficient multiscale method for the simulation of a large class of low-speed internal rarefied gas flows, which are critical to a range of future technologies. The method is based on an existing multiscale approach for the simulation of small-scale dense-fluid flows of high-aspect ratio, but has been extended to support fluid compressibility, non-isothermal conditions, three-dimensional domains, and transience. Furthermore, the method is able to treat a broader range of flows: periodic, non-periodic, body-force-driven, pressure-driven, thermally-driven, and shear-driven. It also incorporates pseudospectral methods, and so boasts excellent convergence characteristics and accuracy.

All verification cases presented herein are designed to be amenable to solution by a full molecular treatment (where scale separation is not exploited). The computationally demanding simulation technique known as direct simulation Monte Carlo (DSMC) is employed to obtain reference solutions, allowing for comparison with those computed by the multiscale method: excellent agreement is observed throughout. The unsteady (time-marching) implementation of the method, which allows for the resolution of transient flows, is validated by comparison with time-dependent experimental data. Again, agreement is excellent.

The computational efficiency of the multiscale method is exceptional. It provides efficiency gains of multiple orders of magnitude, relative to full molecular simulations (by the DSMC method); in some cases, the multiscale method allows for the solution of otherwise computationally intractable problems. Note, highly-scale-separated systems are simulated with even greater efficiency.

Following the experimental validation of the method, it is applied to the study of thermal-transpiration compressors (and implicitly Knudsen compressors). We characterise the effectiveness of these devices by considering the maximum pressure difference attainable for various combinations of (realistic) thermodynamic and geometric conditions. The development time required to obtain this pressure difference, which is also considered as a performance indicator, is also computed.

Nomenclature

Latin

A	$[\mathrm{m}^2]$	cross-sectional area
A'	$[\mathrm{m}^2]$	total area
C	[-]	performance improvement
$\mathbf{F}$	$[\mathrm{N\,kg}^{-1}]$	external force per unit mass
$\mathcal{F}$	[-]	micro model
G	[-]	measure of computational intensity
$\mathcal{J}$	[-]	collision integral (non-linear)
L	[m]	characteristic length
L_s	[m]	streamwise length
L_x	[m]	length in x-direction
L_y	[m]	length in y-direction
$\mathcal{L}$	[-]	collision integral (linear)
M	[-]	number of models
$\dot{M}$	$[\mathrm{kg\,s}^{-1}]$	macroscopic mass flow rate
$\mathcal{M}$	$[\mathrm{kg\,s}^{-1}]$	mass flow rate measured by the dsmcFoam solver
N	[-]	number of representative particles
$N_{\texttt{ang.}}$	[-]	number of discrete solid angles
$N_{\texttt{cha.}}$	[-]	number of parallel capillaries
N_s	[-]	number of cells in the streamwise direction
$N_{\texttt{sam.}}$	[-]	number of samples
$N_{\texttt{vel.}}$	[-]	number of grid points
$\mathcal{N}$	[-]	number of deviational particles
P	[-]	probability of a collision
Q	$[\mathrm{kg\,s}^{-1}]$	mass flow rate (dimensional, shear driven)
Q_T	[-]	mass flow rate (dimensionless, thermally-driven)
Q_p	[-]	mass flow rate (dimensionless, pressure-driven)

R	$[\mathrm{J\,kg^{-1}\,K^{-1}}]$	specific gas constant
R_x	[m]	radius of curvature in x
R_y	[m]	radius of curvature in y
S	[-]	degree of scale separation
T	[K]	temperature
$\mathcal{T}$	[-]	number of time steps (development)
$\mathbb{T}$	[Pa]	shear stress tensor
U	$[\mathrm{m\,s^{-1}}]$	characteristic velocity
$\mathbf{U}$	$[\mathrm{m\,s^{-1}}]$	velocity vector field with components $u\,, v\,, w$
V	$[\mathrm{m^3}]$	volume
W	[-]	ratio of real particles to representative particles
$\mathcal{W}$	[-]	deviational particle weighting
$\mathcal{X}$	[-]	micro data
a	$[\mathrm{m\,s^{-2}}]$	external acceleration
a'	$[\mathrm{m^2}]$	tessellated area
$\boldsymbol{c}$	$[\mathrm{m\,s^{-1}}]$	velocity vector
c_0	$[\mathrm{m\,s^{-1}}]$	most probable thermal speed $\sqrt{2RT}$
c_r	$[\mathrm{m\,s^{-1}}]$	relative speed between colliding particles
d	[m]	molecular diameter or side length
f	[-]	distribution function
$\mathbf{f}$	$[\mathrm{N\,m^{-3}}]$	body force per unit volume
j, k	[-]	constants of proportionality
k_B	$[\mathrm{m^2\,kg\,s^{-2}\,K^{-1}}]$	Boltzmann constant
ℓ	[-]	index (iteration)
m	[kg]	molecular mass
$\dot{m}$	$[\mathrm{kg\,s^{-1}}]$	mass flow rate
n	$[\mathrm{m^{-3}}]$	number density
p	[Pa]	pressure
$\boldsymbol{q}$	$[\mathrm{W\,m^{-2}}]$	heat flux vector
r	[m]	radius or inradius
s	[-]	streamwise direction
s_p	[-]	particle sign

t	[s]	time
x, y, z	[m]	Cartesian coordinates
$\boldsymbol{x}$	[m]	position vector

Greek

ΔT	[K]	temperature difference
Δp	[Pa]	pressure difference
$\Delta \tilde{p}$	[Pa]	maximum pressure difference
Δt	[s]	time step
$\Delta t_{1/2}$	[s]	half-time step
Δx	[m]	cell size (spatial discretisation)
Λ	[-]	state variable
Ξ	[-]	approximately the number of deviational particles per cell
Π	[-]	number of subdomains
Φ	[$\mathrm{Pa\,m^{-1}}$]	pressure-gradient correction
γ	[m]	wall thickness
δ	[-]	rarefaction parameter
ϵ	[-]	departure from equilibrium
ϵ_w	[-]	relative statistical error in streamwise velocity w
$\zeta_{\texttt{tol.}}$	[-]	convergence criterion tolerance
η	[-]	packing density
κ	[-]	adiabatic index
λ	[m]	mean free path
μ	[Pa s]	dynamic viscosity
ν	[$\mathrm{m^2\,s^{-1}}$]	kinematic viscosity
ξ	[-]	the number of representative particles per cell
ρ	[$\mathrm{kg\,m^{-3}}$]	mass density
σ	[-]	standard deviation
σ_T	[$\mathrm{m^2}$]	collision cross section
σ_w	[-]	standard deviation of the streamwise velocity w
$\boldsymbol{\sigma}$	[Pa]	viscous stress tensor
τ	[s]	characteristic time scale
$\overline{\tau}$	[s]	mean free time

$\widetilde{\tau}$	[s^{-1}]	characteristic time constant
υ	[-]	Knudsen number based on wall thickness
ϕ	variable	scaled streamwise gradients
ω	[-]	viscosity index

Subscripts

0	equilibrium value
B	boundary
`DS`	direct simulation Monte Carlo
L	scale separation (length)
`LV`	low-variance deviational simulation Monte Carlo
T	temperature
c	cold
`cell`	cell
`coll.`	collision
d	deviational
f	representation (full-domain)
h	hot
i, j, k	index
m	representation (multiscale)
p	pressure
`ref.`	reference value
t	scale separation (time)
`tran.`	transport

Superscripts

ℓ	index (iteration)
n	time step

Acronyms

DSMC	direct simulation Monte Carlo
HMM	heterogeneous multiscale method
IMM	internal-flow multiscale method
LVDSMC	low-variance deviational simulation Monte Carlo
VHS	variable hard sphere

Chapter 1

Introduction and background

Assume that we are interested in the behaviour of the low-speed flow of a rarefied gas in the high-aspect-ratio conduit shown in Fig. 1.1. Flows of this type are of critical importance to a range of future micro/nano-technologies, such as: micro-heat exchangers for cooling integrated circuits, micro-jet actuators for flow control in aerospace, hand-held gas chromatography systems, micro-reactors to generate small quantities of chemicals, and a host of other 'lab-on-a-chip' devices. Clearly, due to the many advantages associated with their use (reduction in the total resources required, high system performance per unit cost and mass, ease of mass production, high system reliability through redundancy, etc.), such systems are being developed for applications in many industrial sectors (e.g. medicine, aeronautics, defence, etc.).

To understand how such flows may be modelled numerically, we must appreciate that a rarefied gas cannot be modelled using the Navier-Stokes-Fourier equations of continuum gas dynamics; to do so would require the system to be in *local thermodynamic equilibrium*. For this to be true, the frequency of intermolecular collisions must be sufficient to effectively equilibrate the molecular distribution (for consistency with local macroscopic properties). More explicitly, the typical frequencies of a flow must be sufficiently small compared to the mean collision rate; alternatively, in terms of length scales, macroscopic gradients must be sufficiently large compared to the average distance travelled by molecules between successive collisions (the mean free path λ). This condition is unsatisfied when treating gas flows at small scales, i.e. the characteristic length scale is of the order of (or exceeds) the mean free path. The implications form the motivation for the work presented in this thesis, and require us to seek other means by which we can efficiently model the low-speed flow of a rarefied gas in high-aspect-ratio conduits.

The degree of gas rarefaction, and the departure from local thermodynamic equilibrium, is expressed by the Knudsen number:

$$\mathrm{Kn} = \frac{\lambda}{L}\,, \tag{1.1}$$

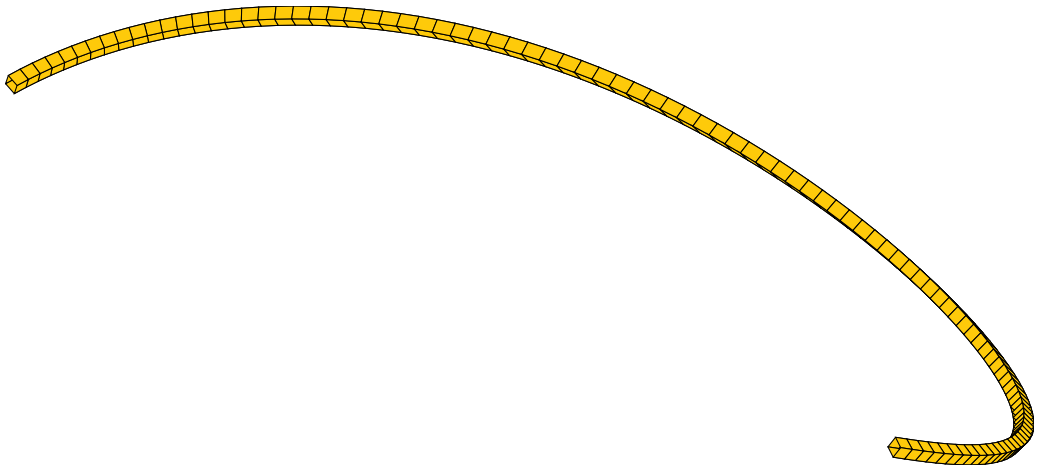

Figure 1.1: Generic high-aspect-ratio conduit with square cross section.

where L is the characteristic length of the system. It is this dimensionless parameter that we will use to identify a number of flow regimes, and quantify the validity of various models. For $\mathrm{Kn} \ll 1$, the various conventional continuum based methods are applicable. This condition does not hold when $L \to 0$, or $\lambda \to \infty$. If $\mathrm{Kn} \geq \mathcal{O}(1)$, the Boltzmann equation must be invoked to understand and compute the flow. Therefore, in regard to Fig. 1.1, if the characteristic length, i.e. the height of the conduit, is on the order of (or smaller than) λ, we must obtain a solution to the flow problem according to the Boltzmann equation: a task that requires considerable computational effort (in the form of main memory and processing requirements). Before the Boltzmann equation is presented, and the numerical challenges of its solution are described, the flow regimes are defined [Struchtrup, 2005]:

$\mathrm{Kn} < 10^{-2}$
: **The continuum limit:** the Navier-Stokes equations (or Euler equations for lower Kn) with classical no-slip boundary conditions are applicable.

$10^{-2} \lesssim \mathrm{Kn} \lesssim 10^{-1}$
: **The slip regime:** the Navier-Stokes equations remain applicable, but rarefaction effects at walls (the velocity 'slip' and temperature 'jump') must be accounted for by the appropriate boundary conditions.

$10^{-1} \lesssim \mathrm{Kn} \lesssim 10$
: **The transition regime:** not in local thermodynamic equilibrium, and intermolecular collisions are considered. The Boltzmann equation is solved.

$\mathrm{Kn} \gtrsim 10$
: **The free molecular limit:** relative to surface interactions, intermolecular collisions are negligible. The (collisionless) Boltzmann equation is solved.

Note, the limits of these regimes are only approximate. For $10^{-1} \lesssim \mathrm{Kn} \lesssim 1$, the gas can be modelled as a continuous medium by refined continuum models [Burnett, 1936; Reinecke and Kremer, 1990; Shavaliyev, 1993].

As even rarefied gases are likely to consist of a vast number of particles, classical Newtonian mechanics cannot be used for their simulation. Instead, the Boltzmann equation [Boltzmann, 1872], which is central to the *kinetic theory of gases*, is used to describe the behaviour of a dilute gas. The quantity of primary interest is the *single particle distribution function* $f(\boldsymbol{x}, \boldsymbol{c}, t)$, where t is the time, and $\boldsymbol{x} = \{x_1, x_2, x_3\}$ and $\boldsymbol{c} = \{c_1, c_2, c_3\}$ are the particle position and velocity vectors, respectively. Therefore, $f(\boldsymbol{x}, \boldsymbol{c}, t)$ is a function of seven variables and is such that the number of particles N in the interval $\{\boldsymbol{x}, \boldsymbol{x} + \mathrm{d}\boldsymbol{x}\}$ with velocities $\{\boldsymbol{c}, \boldsymbol{c} + \mathrm{d}\boldsymbol{c}\}$ (occupying the six-dimensional phase space element $\mathrm{d}\boldsymbol{x}\,\mathrm{d}\boldsymbol{c}$) at t is [Struchtrup, 2005]

$$\mathrm{d}N = f(\boldsymbol{x}, \boldsymbol{c}, t)\ \mathrm{d}\boldsymbol{x}\,\mathrm{d}\boldsymbol{c}\,. \tag{1.2}$$

We can see how the discretisation of phase space affects accuracy, since we only know the state of a particle within the finite size of the element. The low-order velocity moments of $f(\boldsymbol{x}, \boldsymbol{c}, t)$ give various macroscopic parameters at position $\boldsymbol{x}$ and time t, such as mass density ρ, flow velocity $\mathbf{U} = (u, v, w)$, temperature T, pressure p, etc.

The integro-differential equation for f (functional dependencies are omitted for clarity) known as the Boltzmann equation is introduced:

$$\frac{\partial f}{\partial t} + \boldsymbol{c} \cdot \frac{\partial f}{\partial \boldsymbol{x}} + \mathbf{F} \cdot \frac{\partial f}{\partial \boldsymbol{c}} = \mathcal{J}[f, f]\ , \tag{1.3}$$

where $\mathbf{F}$ is an external force per unit mass, and $\mathcal{J}[f, f]$ is a non-linear integral, known as the collision integral, that describes the change of f due to intermolecular binary collisions. Note, with an increase in Kn, intermolecular collisions, and therefore $\mathcal{J}[f, f]$, become decreasingly relevant. The Boltzmann equation describes the spatio-temporal evolution of an ideal gas, and its complexity (which is primarily due to the nature of the collision integral) is such that solutions are not easily obtained.

Before discussing methods for the solution of the Boltzmann equation, we demonstrate why it is necessary by describing two distinct transport phenomena associated with rarefied gas dynamics. The first is observed as a clear minimum in the pressure-driven (dimensionless) flow rate in a conduit as the degree of rarefaction (Kn) increases. The Navier-Stokes equations with no-slip boundary conditions predict a vanishing flow as $\mathrm{Kn} \to \infty$. The second manifests as the apparent violation of the second law of thermodynamics, causing gas transport to occur from (relatively) low to high temperature regions: an effect known as thermal transpiration.

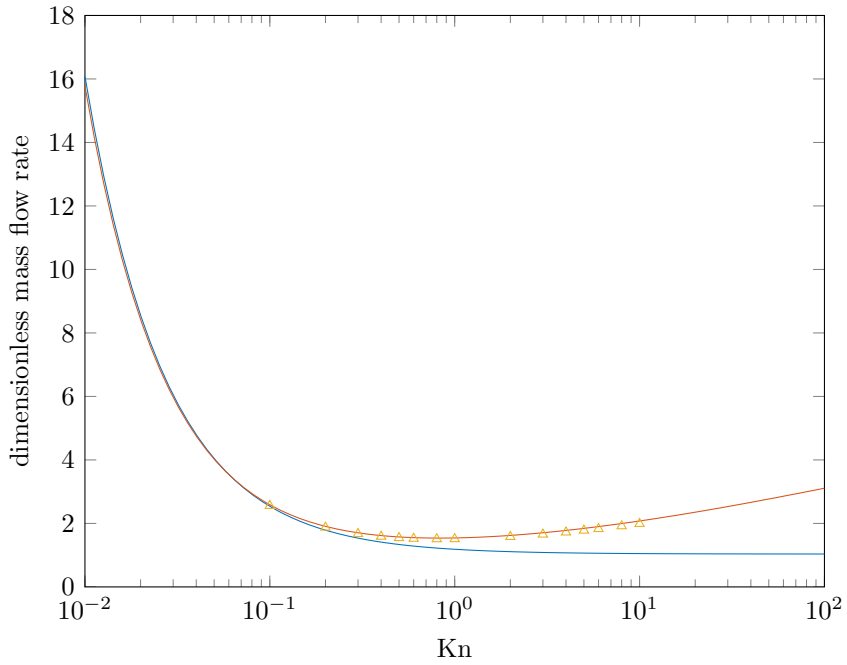

Figure 1.2: The Knudsen minimum as captured by solving (deterministically) the Bhatnagar-Gross-Krook (BGK) [Bhatnagar et al., 1954] model equation (——), and Doi [2010] (△). The Navier-Stokes equations with first-order slip boundary conditions (——) fails to predict the correct behaviour as $\mathrm{Kn} \to \infty$.

When a constant pressure difference drives a rarefied gas through a conduit, the dimensionless flow rate exhibits a characteristic minimum between continuum and transition regimes (see Fig. 1.2). This phenomenon, referred to as the Knudsen minimum [Knudsen, 1909a], is commonly used to benchmark solvers for the simulation of rarefied gas flows. Generally, 'coarse-grained' (macroscale) models, such as the Navier-Stokes equations with slip (or no-slip) boundary conditions, are unable to capture this minimum (see Lockerby et al. [2004] for a discussion of slip).

Thermal transpiration is a phenomenon which induces the steady flow of a rarefied gas solely by the application of a streamwise temperature gradient. This flow vanishes as $\mathrm{Kn} \to 0$. The physical mechanism for this effect is attributed to the momentum exchange that occurs between gas molecules and a surface over which a temperature gradient exists [Sone, 2000]. Consider a stationary gas in the vicinity of a surface; a streamwise temperature gradient is imposed on this surface. Molecules impinging on a small surface area $\mathrm{d}A$ are undistributed during their collisionless free flight (of the order of λ), and thus keep the properties acquired at their origin. Therefore, the average thermal speed of molecules arriving from (relatively) hot regions is greater than that of molecules arriving from (relatively) cold regions. Due to the resulting imbalance in the momentum transferred to $\mathrm{d}A$, a reactionary force is imparted on the gas in the direction of low to high temperature regions.

To reiterate, the equations of Navier-Stokes and Fourier lose their validity as the characteristic length scale becomes comparable to the mean free path; these models are unable to capture non-equilibrium effects, such as those described above. While other (more refined) generalised continuum models (such as the Burnett [Burnett, 1936] and super-Burnett [Chapman and Cowling, 1991] equations, which can be obtained from the Chapman-Enskog expansion of the Boltzmann equation to second and third order [Struchtrup, 2005]) may be used to describe flows in the transition regime (to an extent), they suffer from some degree of physical inaccuracy, or are too computationally intensive to analyse numerically [Agarwal et al., 2001]. Furthermore, much work is still required to assess the physical relevance, range of applicability, and accuracy of these methods [Saint-Raymond, 2009].

The Boltzmann equation accurately describes rarefied gas flows (under the assumptions of binary collisions and molecular chaos), but the computational effort required for its solution cannot be overstated. Note, we use the term 'solution' in a broad sense, as the exceptionally popular direct simulation Monte Carlo (DSMC) method [Bird, 1994] (used extensively herein) is not the application of standard numerical analysis to the Boltzmann equation (for its numerical solution); it is a direct physical simulation of the motion of representative molecules, and is consistent

with the Boltzmann equation [Bird, 1970; Wagner, 1992]. Broadly speaking, general methods for the solution of the Boltzmann equation are computationally intensive, and it is often the case that high performance computing facilities are required for the timely computation of solutions. This presents a challenge, as scientists and engineers concerned with the design of small-scale (or low-pressure) devices, where rarefied gas flows are typical, require the use of these methods. In some cases, particularly when dealing with near-equilibrium flows in non-trivial multi-dimensional internal geometries, these methods are inefficient, or even computationally intractable. For the efficient numerical study of rarefied flows, we must limit the use of these methods. This is possible by exploiting the spatial and temporal scale separation of certain problems to form a multiscale method that couples the physics of multiple models with their associated benefits. Simply stated, when convenient and efficient coarse-grained (macro) models fail as a result of their limited accuracy, we may utilise more general (micro) models (i.e. the Boltzmann equation) in a controlled manner (limiting computational intensity) to supplement or replace the former.

1.1 Multiscale modelling

As alluded to in the preceding section, a hierarchy of physical models of varying fidelity and validity exist for the treatment of gas flows. The validity of these models, when considered independently, is quantified by parameters such as the Knudsen number (Kn), Reynolds number (Re), and Mach number (Ma). Based on these parameters, a flow system tends to be described by employing a single valid model. The computational effort required for the solution of these models is highly variable, and generally we would like to minimise our use of those which are computationally intensive. Through the coupling of multiple models (that constitute the aforementioned hierarchy), we adopt a multiscale representation, effectively employing detailed (computationally intensive) micro models only where (and when) efficient macro models are inadequate. By doing so, we limit the use of computationally intensive methods that would otherwise be used to fully describe a system in thermodynamic non-equilibrium. Note, the term micro is used herein to define regions where non-equilibrium effects are resolved; other regions are termed macro.

Consider the flow of a rarefied gas in a generic internal-flow geometry, as depicted in Fig. 1.3a. As mentioned previously, the Boltzmann equation can be solved (numerically or indirectly via the direction simulation of representative molecules) to model a (rarefied) gas. Let us consider the well-established direct simulation Monte Carlo method, which is used extensively for the scientific study of rarefied gas flows.

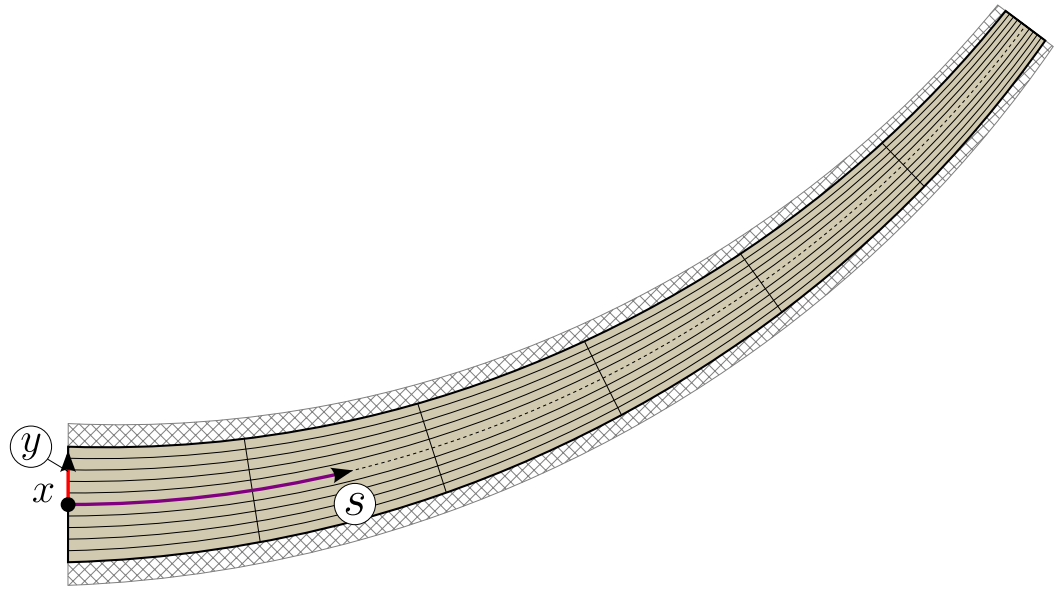

(a) A generic internal-flow geometry.

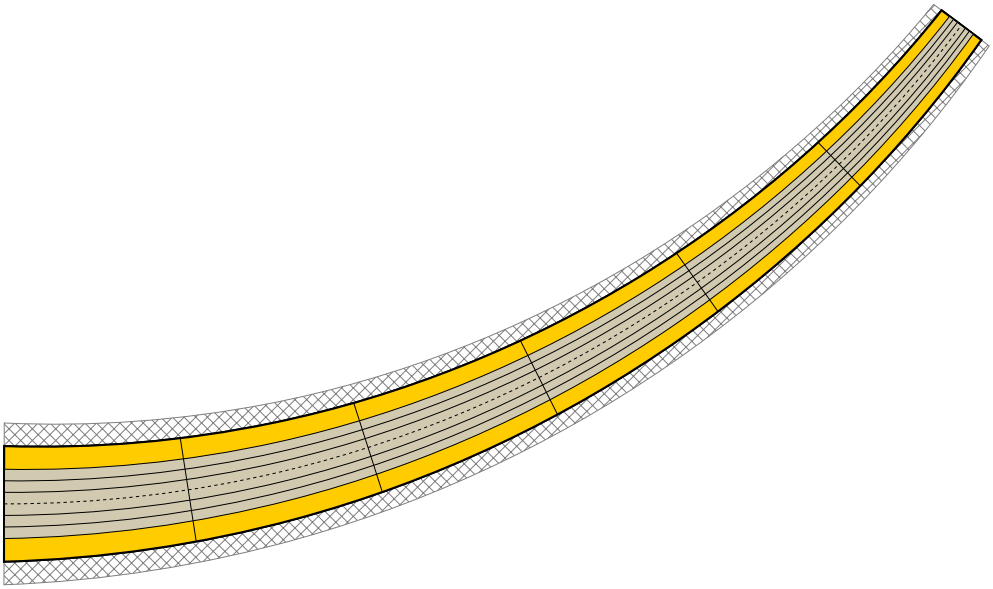

(b) The domain decomposition method.

Figure 1.3: Various frameworks for multiscale (multiphysics, multifidelity) modelling applied to a generic internal-flow geometry. A costly micro solver is employed for the solution of a micro model in micro domains. A macro solver, with less computational overhead, is used for the solution of a macro model in macro domains.

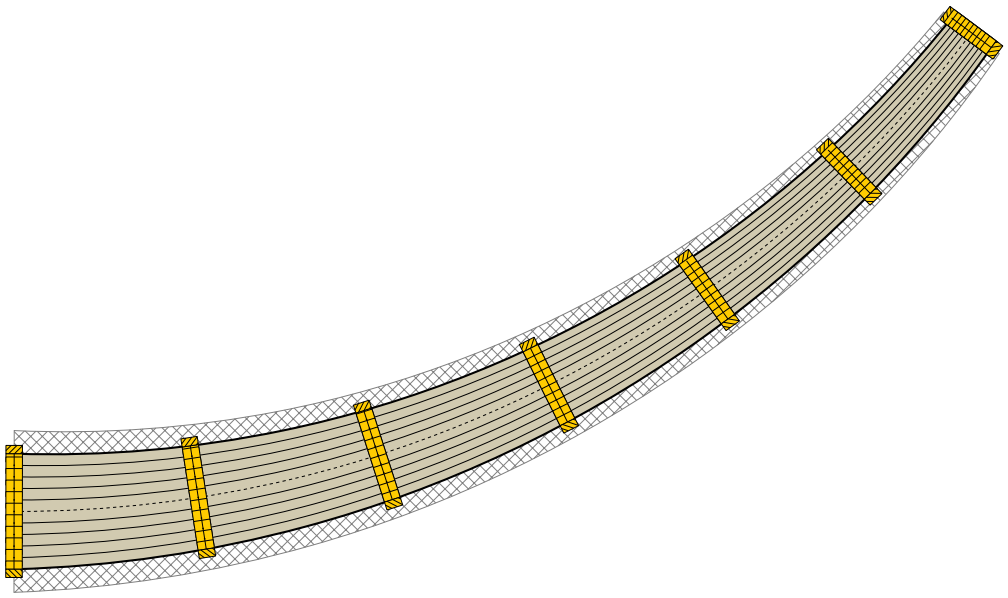

(c) The heterogeneous multiscale method [Ren and E, 2005].

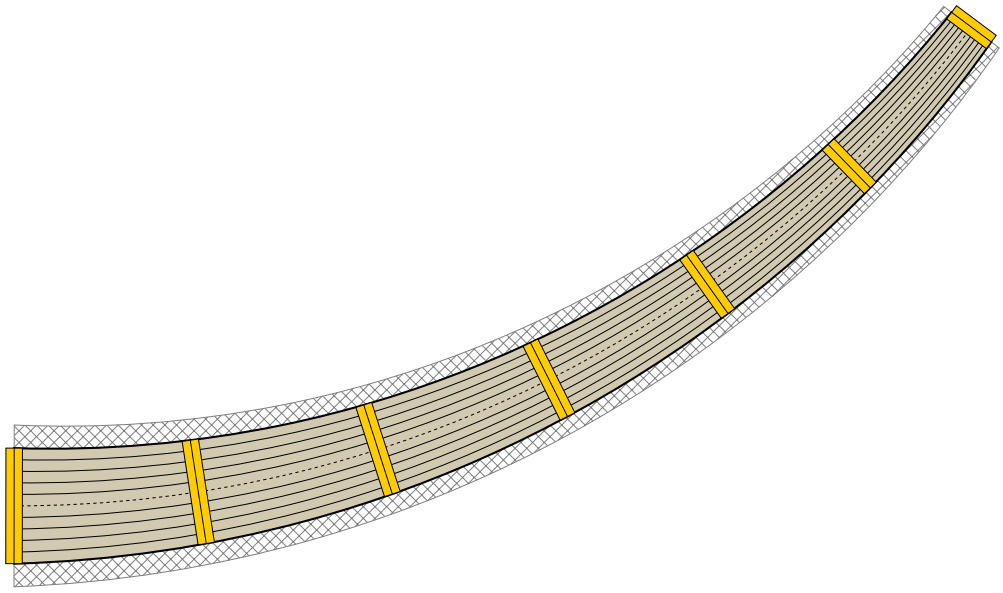

(d) The internal-flow multiscale method [Borg et al., 2013a].

Figure 1.3: Various frameworks for multiscale (multiphysics, multifidelity) modelling applied to a generic internal-flow geometry. A costly micro solver is employed for the solution of a micro model in micro domains. A macro solver, with less computational overhead, is used for the solution of a macro model in macro domains.

This method 'directly simulates' the Boltzmann equation by statistically modelling the behaviour of representative molecules, and can be applied to accurately resolve the flow within the conduit. Although it is widely used to simulate rarefied flows at small scales, the computational intensity of the method is considerable, and (generally) far exceeds that of the familiar solvers of computational fluid dynamics (CFD). If we choose to use this method alone, a full and unnecessarily detailed description of the flow field is obtained at great computational expense. Alternatively, a multiscale method may be applied for the efficient and accurate solution of the problem.

The classification system of Abdulle et al. [2012] is used to distinguish between various multiscale problems. Those which involve localised non-equilibrium effects are labelled as type I problems. To independently model regions where (costly) micro (molecular) resolution is essential, the (physical) computational domain is decomposed; a macro model adequately describes the flow in all other regions. Micro and macro solvers are coupled at an interface. Type II problems require the micro model to inform the macro model (e.g. for constitutive relations or boundary conditions). Such problems may be solved efficiently by embedding micro subdomains within the macro domain. Type III problems are similar to type II, but they involve the high-aspect-ratio non-equilibrial flow through conduits. Such flows are highly confined, and the size of the Knudsen layer (where non-equilibrium effects manifest near a solid surface) tends to be of the order of the characteristic length (which we take to be the height) of the conduit, i.e. the entire flow field is non-equilibrial. In the following section, we discuss (candidate) general frameworks for the design of a multiscale method capable of solving type III problems (the focus of this thesis).

1.1.1 The domain decomposition method

Suppose we are able to identify the regions of a computational (physical) domain where the localised non-equilibrium effects of a type I problem are dominant. To resolve these, a micro model is solved using a micro solver. All other regions are accurately described by a macro model; the computational effort required for its solution is minimal in comparison. By coupling micro and macro solvers (through fluxes or state variables) the flow field is resolved accurately and efficiently. This basic strategy is what defines the *domain decomposition method*: a relatively simple general framework for the design of multiscale methods (with various micro/macro solver combinations, and levels of sophistication) that has been applied extensively for the study of rarefied gas flows [Hash and Hassan, 1996; Le Tallec and Mallinger, 1997; Roveda et al., 1998; Tiwari and Klar, 1998; Wijesinghe and Hadjiconstantinou, 2004; Wijesinghe et al., 2004; Wu et al., 2006; Schwartzentruber et al., 2007].

Because the literature covers a vast range of applications of the domain decomposition method, we will only assess its suitability by considering the main features that distinguish it (which are common to all applications). The domain is decomposed to form subdomains in which disparate models are solved. These subdomains are coupled at an interface, where the most conceptually elegant applications facilitate the communication of models of the same nature. For example, the coupling of multiple particle-based methods [Burt and Boyd, 2009a,b], or the direct numerical solution of the Boltzmann equation with kinetic schemes that are derived by taking moments of the Boltzmann equation (see Sone [2007] for details).

The success of this approach is dependent on the chosen coupling strategy and the imposition of suitable boundary conditions. In general, the boundary conditions of each subdomain are set through the bi-directional exchange of information between the solvers. At the micro/macro interface, which can been treated as a shared boundary or zone, it is essential that the behaviour of the flow described by independent models is consistent; even the subtlest inconsistencies can produce significant errors. This presents a challenge, as we must parametrise the validity of each model, and form a breakdown criteria that is typically dependent on the problem. In addition, it is necessary to derive micro boundary conditions from macroscopic properties in the correct manner. For example, if the DSMC method and Navier-Stokes equations are loosely coupled at an interface, particle velocities should generally be sampled from the Chapman-Enskog distribution [Chapman and Cowling, 1991; Garcia and Alder, 1998] (defined using macroscopic properties), as we are attempting to treat a near-equilibrium flow at the micro/macro interface (where the Maxwellian distribution is not suitable). The solution is not always so straightforward, as in the case of dense fluids (see Hadjiconstantinou [2005]).

Despite the success of the domain decomposition method, it should be avoided when investigating certain classes of flow [Hadjiconstantinou, 2005]. As illustrated in Fig. 1.3b, by the application of the domain decomposition method to the generic (highly-confined high-aspect-ratio) flow geometry shown in Fig. 1.3a, the computational domain is decomposed to form two separate micro subdomains (assuming a two-dimensional macro domain). In order to capture near-wall phenomena, such as the velocity slip and temperature jump, these subdomains must extend the entire length of the conduit. Consequently, to avoid the excessive use of the computationally intensive micro solver, the maximum length of the conduit must be restricted. Moreover, as the Knudsen number increases and the Knudsen layer expands further into the bulk, we eventually find that the macro model is invalid everywhere; the efficiency of the domain decomposition method is completely diminished.

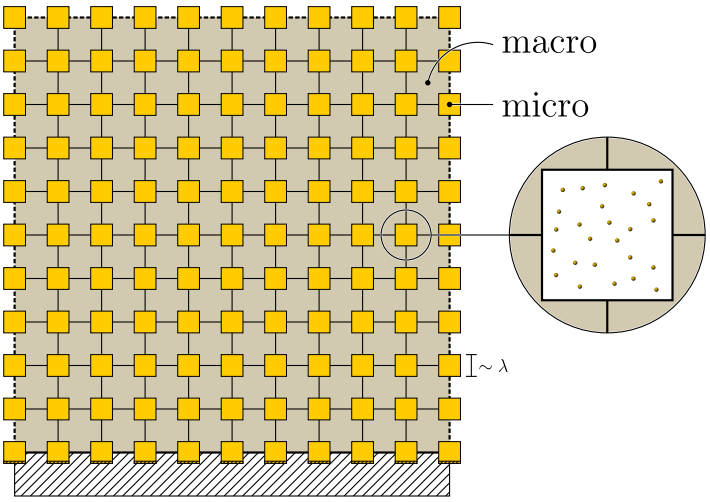

Figure 1.4: The heterogeneous multiscale method [E et al., 2007]: the general configuration. Micro subdomains are embedded at the grid points of the macro domain.

1.1.2 The heterogeneous multiscale method

Type II problems require the use of a micro model to inform the macro model; the micro model provides molecular resolution to derive accurate transport coefficients, boundary conditions, or constitutive relations used by the macro model. Such problems can be solved by the application of the *heterogeneous multiscale method* (HMM) [E et al., 2007; E and Li, 2004; Ren and E, 2005], which is outlined in the following.

A macro solver operates on a grid with resolution that is consistent with the flow gradients in that dimension of the (physical macro) domain (illustrated in Fig. 1.3a). At the nodes of this grid we evaluate some macro model (possibly the continuum formulation of conservation of mass, momentum, and energy), using some numerical method (macro solver), to obtain a macroscopic description of the flow field. While this configuration is sufficient when treating a flow system in local thermodynamic equilibrium, it must be supplemented otherwise. Therefore, rarefied gas flows through such geometries can be resolved by supplementing the incomplete macro model with information derived from a micro model, which accounts for the deficiencies in the former. Effectively, we embed micro subdomains (which are physically decoupled from the macro domain) at the grid points of the macro domain, as seen in Fig. 1.4. The size of a micro subdomain is such that we can guarantee accuracy. Those which exist in the core of the macro domain make use of periodic boundary conditions, solely. It is also important to note that micro-solver instances do not communicate directly; all communication is facilitated by the macro solver.

A potential coupling strategy, based on the work of Kessler et al. [2010], is presented in the context of an example case: the viscous stress tensor $\boldsymbol{\sigma}$ and heat flux vector $\boldsymbol{q}$ of the generalised conservation equations,

$$\frac{\partial \rho}{\partial t} + \nabla\cdot(\rho\mathbf{U}) = 0\,, \tag{1.4}$$

$$\frac{\partial}{\partial t}(\rho\mathbf{U}) + \nabla\cdot(\rho\mathbf{U}\mathbf{U}) = -\nabla p + \nabla\cdot\boldsymbol{\sigma}\,, \tag{1.5}$$

$$\frac{\partial}{\partial t}(\rho E) + \nabla\cdot(\rho E\mathbf{U}) = -\nabla(p\mathbf{U}) + \nabla\cdot(\boldsymbol{\sigma}\cdot\mathbf{U}) - \nabla\cdot\boldsymbol{q}\,, \tag{1.6}$$

are calculated from the molecular velocity fluctuations of DSMC subdomain instances, which are initialised such that macroscopic properties are consistent between models. As previously defined, ρ is the mass density, p is the pressure, t is the time, $\mathbf{U} = (u, v, w)$ is the flow velocity; ρE is the total energy. A similar set of equations can be derived from a molecular viewpoint by taking moments of the Boltzmann equation. Terms that relate the motion of particles to the macroscopic behaviour of the fluid are obtained by comparison of these two sets of equations (the reader is referred to Kessler et al. [2010] for details). The inadequate constitutive relations of the macro model for $\boldsymbol{\sigma}$ and $\boldsymbol{q}$, specifically the Navier-Newton viscosity model and Fourier's law of heat conduction, may be replaced with expressions for $\boldsymbol{\sigma}$ and $\boldsymbol{q}$ based on micro dynamics. When the distribution function f is known at time t, these accurate closure relations can be solved explicitly.

Unsteady (transient) problems require greater attention, as multiple time scales become relevant. In the simplest case, two time scales exist: the time scale over which (1) the micro model equilibrates, and (2) the macroscopic properties of the system evolve. If these are of the same order, time-scale separation cannot be used to improve computational efficiency. Generally, however, the characteristic micro time scale is many orders of magnitude smaller, allowing us to apply a time-step coupling scheme for the accelerated solution of the problem. The exploitation of time-scale separation is discussed in Chapter 4 and Lockerby et al. [2013].

Let us apply the HMM to the generic flow geometry shown in Fig. 1.3a. Figure 1.3c illustrates that the HMM is not suitable where the molecular scale (e.g. the mean free path) is comparable to the transverse scale; micro subdomains, which have a minimum size of the order of λ, are forced to overlap. The efficiency of the HMM suffers significantly as a result. Note, depending on the macro solver, the underlying grid of the macro domain must be reasonably fine to ensure accuracy and numerical stability. As the Knudsen number increases and the overlapping of subdomains is exacerbated, we begin to encounter another, more serious issue:

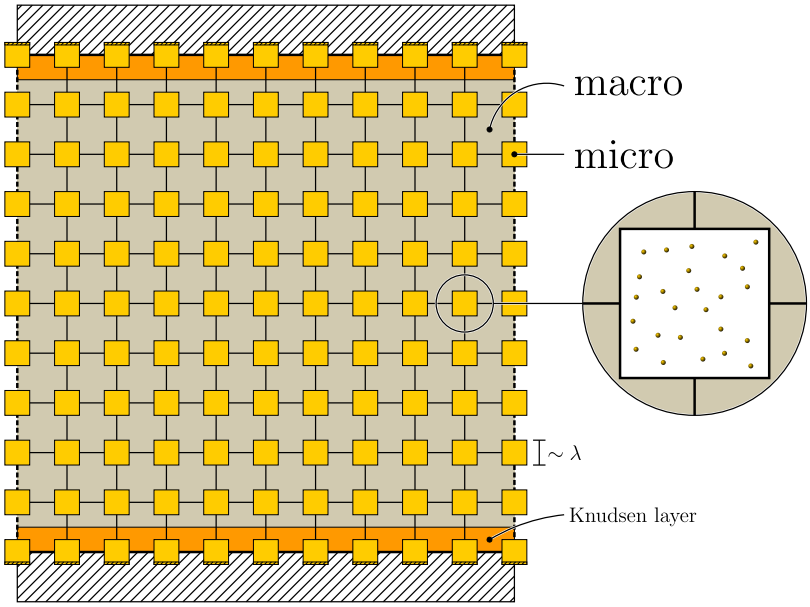

(a) The heterogeneous multiscale method. When Kn is small, the Knudsen layer only exists near the walls of the conduit, and the HMM is adequate.

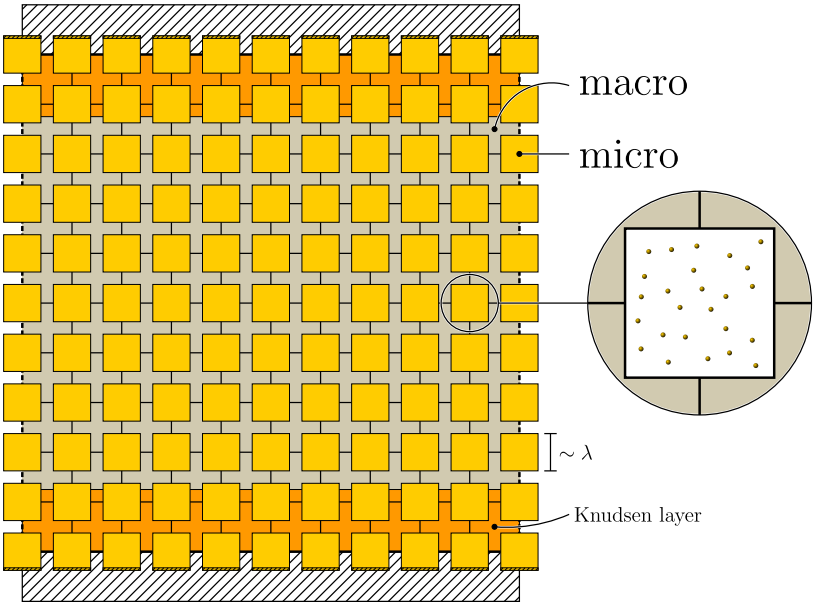

(b) The heterogeneous multiscale method. As Kn $\to \infty$, the Knudsen layer expands into the bulk. Even for a moderate Knudsen number, as shown in the above, the HMM becomes ill-suited. Subdomains in the bulk will not capture the non-equilibrium effects that manifest in the Knudsen layer.

Figure 1.5: Limitations of the heterogeneous multiscale method [E et al., 2007] when applied to highly confined non-equilibrial flows, as the Knudsen number is increased.

subdomains in the bulk (whose state is dictated by local macroscopic properties) are not able to capture non-equilibrium effects in the expanding Knudsen layer (see Fig. 1.5). The HMM may even be ill-suited to treat flows where $\mathrm{Kn} \gtrsim \mathcal{O}(0.1)$. For the solution of problems by the HMM, the macro model must provide (locally) accurate values of state variables to constrain the micro model. This is not possible when the bulk flow is non-equilibrial. It is for these reasons that the HMM, when applied to study flows within highly-confined small-scale conduits, is less accurate and less efficient than a full microscopic treatment. Again, we must seek an alternative.

1.1.3 The internal-flow multiscale method

Hitherto, we have shown that general continuum models (for example, the Navier-Stokes equations) cannot be used (reliably) to model rarefied gas flows, and that the Boltzmann equation must be invoked. However, the numerical methods for the (unnecessarily detailed) solution of the Boltzmann equation are computationally intensive to employ. By coupling micro (i.e. the Boltzmann equation) and macro (i.e. continuum formulations of conservation of mass, momentum, and energy) models, a multiscale approach minimises the computational effort required. Many multiscale methods exist, but only recently has one been introduced that allows for the treatment of non-equilibrial flows in high-aspect-ratio conduits (type III problems): the internal-flow multiscale method (IMM) of Borg et al. [2013a], that was originally intended to model incompressible dense-fluid flows in small-scale devices. As a degree of length-scale separation exists between macroscopic variations in the streamwise direction (s) and microscopic processes occurring in the transverse plane (xy-plane), these flows are multiscale. As such, (equispaced) micro subdomains (in Borg et al. [2013a]) that span the entire cross section of the conduit (representing the local cross-sectional geometry of the macro domain), as illustrated in Fig. 1.3d, are distributed in the s-direction. In Borg et al. [2013a], the number of micro subdomains Π is attributed to the discretisation of the macro domain. All subdomains may be visualised as rectangular cuboids, with periodicity is enforced in the streamwise direction. Like those of the HMM, the micro subdomains are constrained by the macro model. Unlike the HMM, however, the macro model is not supplemented by the micro model. Instead, coupling is enabled by enforcing mass conservation, since, for a steady-state flow, the mass flow rate in each subdomain must be equal:

$$\langle \dot{m}_i \rangle = \text{const.} = \dot{M} \qquad \text{for } i = 1, 2, \ldots, \Pi\,, \tag{1.7}$$

where $\langle \dot{m}_i \rangle$ is the mass flow rate in the i th of Π subdomains. Chevrons denote that the mass flow rate is measured directly, and $\dot{M}$ is the macroscopic mass flow rate.

Because a streamwise-periodic subdomain cannot accommodate a streamwise gradient, an equivalent body force is used to emulate a pressure gradient; this body force (a pressure-gradient correction Φ_i) generates a mass flow rate $\langle \dot{m}_i \rangle$ in the i th subdomain. Through an iterative algorithm, Φ_i is updated to satisfy equation (1.7).

The dimensionless number indicating the degree of length-scale separation is

$$S_L = \min \left\{ \left| \frac{\mathrm{d}L_x}{\mathrm{d}s} \right|^{-1}, \left| \frac{\mathrm{d}L_y}{\mathrm{d}s} \right|^{-1}, \left| \frac{L_x}{\Lambda} \frac{\mathrm{d}\Lambda}{\mathrm{d}s} \right|^{-1}, \left| \frac{L_y}{\Lambda} \frac{\mathrm{d}\Lambda}{\mathrm{d}s} \right|^{-1}, \left| \frac{R_x}{L_x} \right|, \left| \frac{R_y}{L_y} \right| \right\}, \quad (1.8)$$

where L_x and L_y are length scales in the transverse directions that characterise the cross-sectional geometry, Λ is a state variable (e.g., temperature), and R_x and R_y are the radii of curvature of the centre streamline. As $S_L \to 1$, the number of subdomains Π must be increased. Conversely, as $S_L \to \infty$ (increasing length-scale separation), Π can be reduced. Although Π is highly dependent on S_L, the direct relationship between S_L and Π is case dependent; a general relation does not exist.

If $S_L \gg 1$ it can be assumed that, in small streamwise sections of the conduit, the walls are parallel to the centre streamline (and consequently all other local streamlines). This allows for the simulation domain to be represented by streamwise-periodic subdomains (with boundaries that do not converge or diverge). Therefore, S_L effectively determines the applicability of the IMM. Depending on the capabilities of the micro solver utilised, these subdomains are three-dimensional (with a length $\mathcal{O}(\lambda)$ in the s-direction) as illustrated in 1.3d, or two-dimensional, where the subdomains are cross-sectional slices with no dimension in the s-direction.

The concept of gearing ($\mathcal{G}$), which permits a compromise between computational efficiency and resolution, was introduced in Borg et al. [2013a]:

$$\mathcal{G} = \frac{L_s}{\Pi \, \delta s} \quad (1.9)$$

where L_s is the streamwise length of the macro domain and δs is the streamwise length of a subdomain. This is an exceptionally attractive feature of the IMM. As $\mathcal{G}$ is increased, Π is reduced (for a fixed δs which is sufficient such that spurious wrap-around effects do not occur) for greater computational economy at the expense of accuracy (the numerical approximation of the continuous integral of Φ by Simpson's rule suffers). By reducing $\mathcal{G}$ the accuracy is improved, since Π is increased at the expense of computational effort. The domain decomposition method discussed previously does not allow for such a level of control; this is a feature of the IMM (and implicitly the HMM). As mentioned, the computational cost of the latter is directly proportional to L_s, restricting the problems it can treat.

1.1.4 Sequential and concurrent coupling

We end our discussion of multiscale methods by considering the suitability of sequential and concurrent coupling. If we limit our attention to type III problems, which the IMM is tailored to treat, it is relatively straightforward to determine whether information derived from the micro model can be pre-calculated (to allow for sequential coupling). We must simply assess the number of variables (degrees of freedom) that define the value of the mass flow rate $\langle \dot{m}_i \rangle$ (in the i th of Π subdomains). If $\langle \dot{m}_i \rangle$ can be regarded as a function of few variables, computations (which are intended to be repeated) are tackled efficiently by resorting to a lookup table approach. It is important to remember, however, that the intensive use of the micro solver is still required to pre-calculate micro data, which must span many parameter values for accurate interpolation. Because we rarely encounter problems which are sufficiently simple, concurrent coupling, by which the micro solver is instructed to return data on demand, is the technique used in this thesis.

1.2 Solution of the Boltzmann equation

The analytical solution of the Boltzmann equation is limited to collisionless, relatively trivial flow problems. The need to discretise phase space, as well as physical space, is the primary reason for the complexity of its solution. If we just consider the position $\boldsymbol{x}$ and velocity $\boldsymbol{c}$, a six-dimensional representation of phase space is required (assuming three-dimensional physical space). Modelling other parameters, such as the internal energy modes, increases the dimensionality of phase space. The analytical solution of equation (1.3) for engineering relevant flows is completely intractable. Therefore, the numerical solution of the Boltzmann equation is sought.

1.2.1 Deterministic methods

Most deterministic solvers used for the solution of the Boltzmann equation rely on the discretisation of the distribution function f with respect to the velocity $\boldsymbol{c}$ (to evaluate the five-fold collision integral $\mathcal{J}$). This approach defines the discrete velocity or discrete ordinate method: continuous and infinite velocity space is truncated and discretised to form a set of discrete velocities. However, the direct numerical solution of the Boltzmann equation is (still) computationally intensive; for monatomic gases, the computational effort required to evaluate the collision operator is usually $\mathcal{O}\left(N_{\mathtt{vel.}}^7\right)$, at the very least, where $N_{\mathtt{vel.}}$ is the number of grid points in each dimension of velocity space [Wu et al., 2015]. Because the accuracy of the solution is dependent on $N_{\mathtt{vel.}}$, the discretisation of velocity space cannot be coarse.

Many modifications which attempt to reduce the computational effort associated with evaluating the collision integral (by reducing the number of operations) have been proposed. For instance, Morris et al. [2011] use a Monte Carlo method to randomly sample a set of collision partners for each point in velocity space (strictly speaking this is not a fully deterministic method). Kolobov et al. [2007] note that the use of so-called Korobov sequences also reduces the number of operations.

The fast spectral method proposed by Mouhot and Pareschi [2006], which has been extended to treat other collision kernels [Wu et al., 2013, 2014, 2015], is a numerical scheme for the collision integral $\mathcal{J}[f, f]$. The computational effort required to evaluate the collision operator can be reduced to $\mathcal{O}\left(N_{\mathtt{ang.}}^2 N_{\mathtt{vel.}}^3 \log N_{\mathtt{vel.}}\right)$, where $N_{\mathtt{ang.}}$ is the number of discrete solid angles in each dimension of velocity space. These methods are computationally efficient and are exceedingly accurate, owing to their use of spectral methods. They would certainly be useful for the simulation of gas flows at small-scales, used either independently or in conjugation with the IMM to eliminate the streamwise dimension in $\boldsymbol{x}$ and simplify the computation of f.

1.2.2 The direct simulation Monte Carlo method

As an alternative to deterministic methods for the solution of the Boltzmann equation, let us consider the stochastic particle-based simulation method known as the direct simulation Monte Carlo (DSMC) method [Bird, 1994]. It is widely regarded as a reliable, flexible, and efficient method (in the case of multi-dimensional flows) for the direct simulation of the Boltzmann equation, with other rarefied gas models frequently using DSMC as a benchmark for comparison. A large number of representative molecules (N) are tracked through a computational mesh as they interact with walls and each other. These representative molecules (which may be referred to as DSMC particles) represent a number of real molecules. This offers a degree of control over the computational intensity of the method, but, as will be discussed in the following, also affects the statistical uncertainty in sampled quantities.

The DSMC method decouples the transport and collision of particles, effectively simulating the left- and right-hand sides of equation (1.3) in two separate steps, for a time step Δt. Assuming that $\mathbf{F} = 0$, the particles are translated simply according to $\boldsymbol{x}(t + \Delta t) = \boldsymbol{x}(t) + \boldsymbol{c}(t)\,\Delta t$. This step also involves generation or deletion of particles (if applicable), and particle-surface/boundary interaction. The type of surface (impermeable boundary) dictates the behaviour of a reflecting particle, and commonly we deal with either specular or diffuse reflection. The post-collision velocities of a diffusely reflected particle are sampled from an equilibrium (or Maxwellian) distribution function based on the temperature T of the surface.

Following the transport step, pairs of particles within the same computational cell are randomly selected to collide. Therefore, the spatial discretisation of the physical domain is determined as a function of λ, since it would be physically inaccurate to allow particles separated by many mean free paths to collide. In general, and for the simulations presented in this thesis, the maximum cell dimension $\Delta x = \lambda/3$. Similarly, the mean free time ($\bar{\tau} = \lambda/\bar{c}_r$, where $\bar{c}_r$ is the mean (relative) speed of collisions) limits $\Delta t\,(\ll \bar{\tau})$, as particles should be advected without colliding. It has been rigorously shown that as $N \to \infty$ and the discretisation parameters tend to zero ($\Delta t \to 0$ and $\Delta x \to 0$), the DSMC method provides solutions to the Boltzmann equation [Wagner, 1992]. A computational mesh is also required for the statistical sampling of macroscopic quantities; once a steady-state condition is achieved, the appropriate microscopic properties are averaged over a number of time steps to obtain low-noise cell-centred values of macroscopic properties. If the problem is unsteady, an ensemble average (the number of realisations required to obtain the desired fractional error in macroscopic properties has been characterised by Hadjiconstantinou et al. [2003]) is required to improve estimates.

In dilute gases, intermolecular collisions are assumed to always be binary. The exact dynamics of a collision are dependent on the molecular model selected, with those that are more realistic varying the collision cross section σ_T as a function of the relative speed (c_r) between colliding molecules (which includes monatomic, diatomic, and polyatomic molecules). Figure 1.6 shows the effective cylinder of volume $\sigma_T c_r \Delta t$ that is formed by sweeping the collision cross section along the trajectory of a particle. During the interval Δt, a collision will occur if the centre of any other particle exists within the cylinder; the probability that a collision will occur between two molecules is $P = W\sigma_T c_r \Delta t / V_{\texttt{cell}}$, where W is the number of real molecules represented by a DSMC particle, and $V_{\texttt{cell}}$ is the volume of a cell.

All DSMC simulations presented in this thesis make use of the variable hard sphere (VHS) model, where the molecular diameter d is a function of c_r [Bird, 1994]:

$$d = d_{\texttt{ref.}} \left(c_{r,\,\texttt{ref.}}/c_r\right)^{\omega - 1/2} . \tag{1.10}$$

The subscript '`ref.`' denotes reference values, and ω is the viscosity index. This model is able to reproduce the correct temperature dependence of viscosity:

$$\mu = \mu_{\texttt{ref.}} \left(T/T_{\texttt{ref.}}\right)^{\omega} , \tag{1.11}$$

where μ is the dynamic viscosity. For a thorough review of the various molecular models, and the DSMC method, the reader is referred to Bird [1994, 2013].

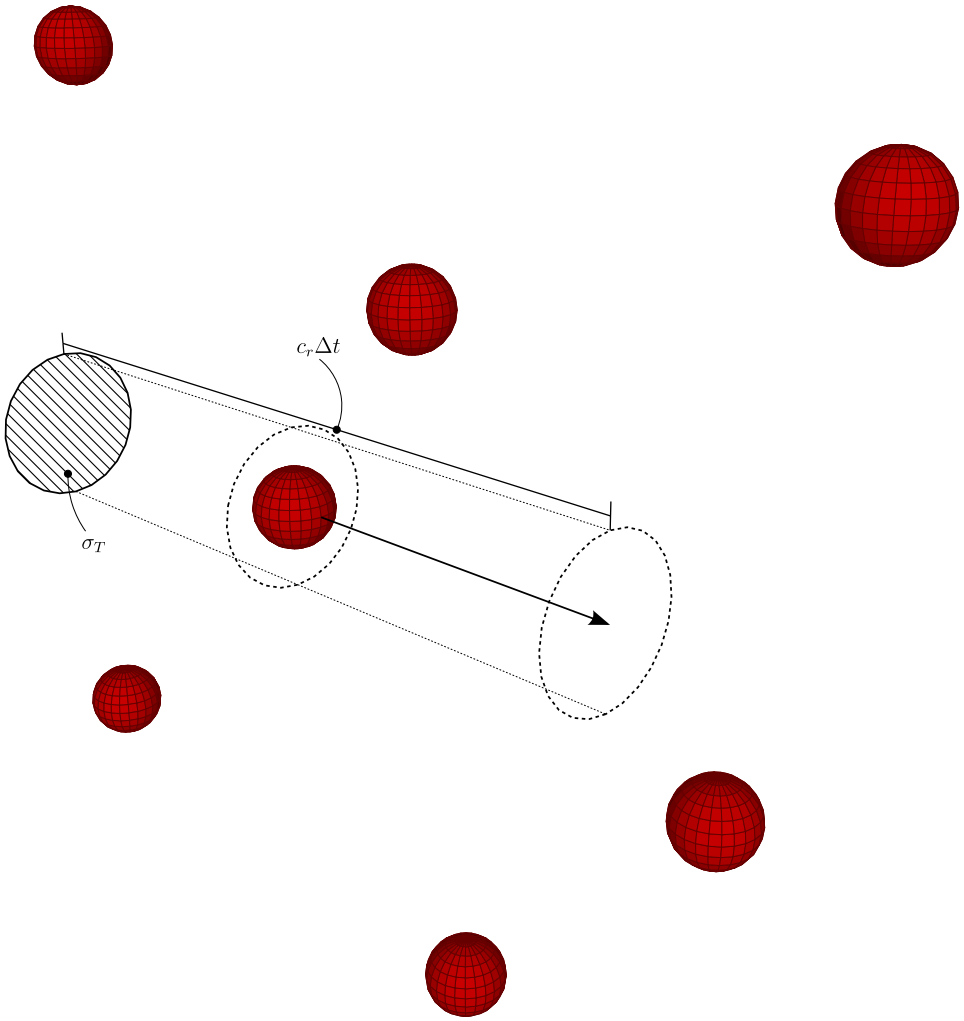

Figure 1.6: Over an interval of time which is much shorter than the mean collision time, assume that the molecule of interest moves through a field of stationary molecules with speed c_r. A collision will occur if the centre of any field molecule exists within the (swept) cylinder of volume $\sigma_T c_r \Delta t$. Adapted from Bird [1994].

Statistical uncertainty

As macroscopic properties are sampled by averaging microscopic properties, the DSMC method is inherently statistical. Hadjiconstantinou et al. [2003] present predictions for the statistical uncertainty due to finite sampling in the presence of thermal fluctuations, and show that relative statistical error can be expressed as

$$\epsilon_w = \frac{\sigma_w}{U} = \frac{1}{\sqrt{N_{\mathtt{sam.}} N_{\mathtt{cell}}}} \frac{1}{\mathrm{Ma}\sqrt{\kappa}}, \tag{1.12}$$

where σ_w is the standard deviation of the streamwise velocity w, U is the characteristic velocity, $N_{\mathtt{sam.}}$ is the number of number of statistically independent samples required to obtain an estimate of w, $N_{\mathtt{cell}}$ is the number of computational particles per cell, and κ is the adiabatic index. Therefore, the computational intensity associated with estimating w with a relative uncertainty ϵ_w using the DSMC method scales as $(\epsilon_w \,\mathrm{Ma})^{-2}$; as $\mathrm{Ma} \to 0$ the DSMC method becomes intractable. This has led researchers to develop computationally efficient (variance-reduced) methods for the simulation of low-speed (or more generally, low-signal) rarefied gas flows.

1.2.3 Low-variance deviational simulation Monte Carlo

Generally, rarefied gas flows at small scales are near thermodynamic equilibrium. Therefore, we would prefer to utilise a method with a computational efficiency that is independent of the relative statistical uncertainty (the ratio of the standard deviation σ to the magnitude of the characteristic signal). The low-variance deviational simulation Monte Carlo (LVDSMC) method introduced by Homolle [2007]; Homolle and Hadjiconstantinou [2007a,b], and more recently developed by Radtke [2011]; Radtke et al. [2011, 2013], is such a method. It provides considerable gains in computational efficiency, and enables the solution of otherwise intractable problems.

Variance reduction

Previously it was shown that, due to the high dimensionality of $f(\boldsymbol{x}, \boldsymbol{c}, t)$, stochastic particle-based methods (such as the DSMC method) for the simulation of the Boltzmann equation may be preferred. The algorithm that dictates the time-accurate advancement of the LVDSMC procedure is similar to that of the DSMC method; both methods provide solutions of the Boltzmann equation by decoupling particle transport and collisions. However, unlike the DSMC method, which utilises N particles to approximate f, the LVDSMC method uses $\mathcal{N}$ deviational particles to simulate (with reduced variance) the deviation from a fixed (global) equilibrium distribution f_0.

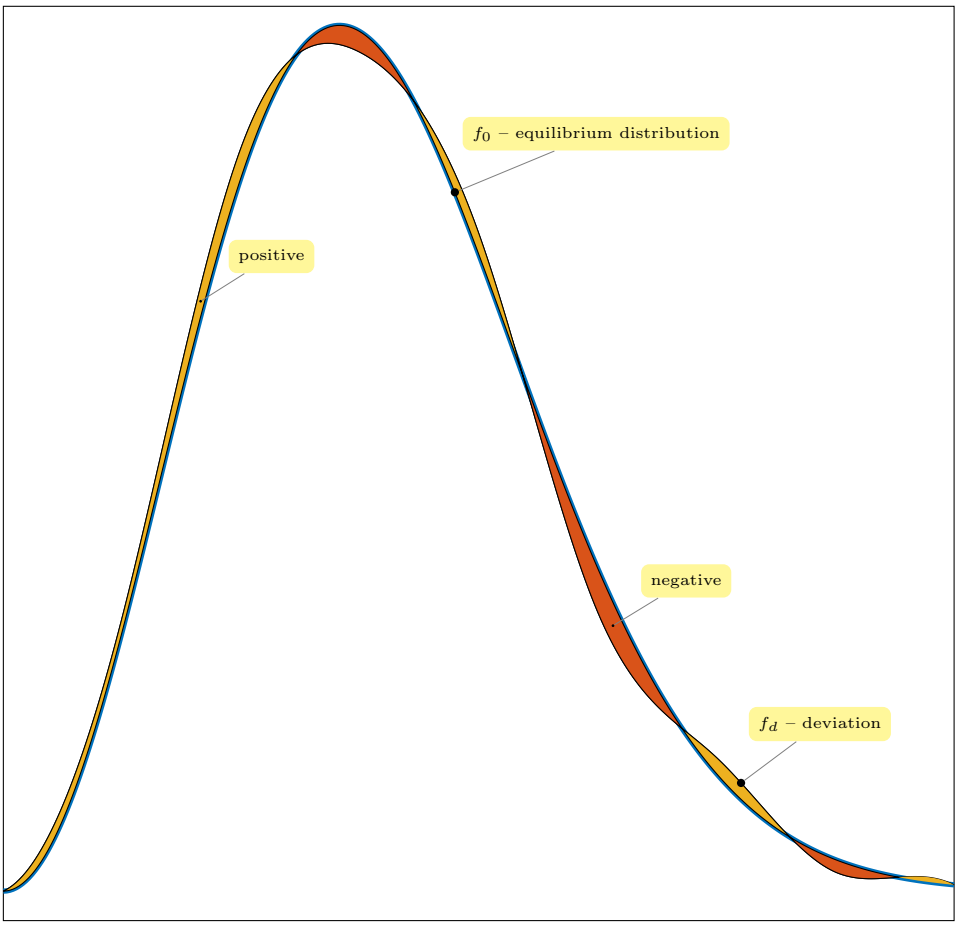

Figure 1.7: Illustration showing deviation from an equilibrium state. The deviation from equilibrium (f_d) must be represented by signed particles.

For near-equilibrium flows this closely approximates the actual distribution function.

$$f_0\left(\boldsymbol{c}\right) = \frac{n_0}{\pi^{3/2} c_0^3} \exp\left(-\frac{\boldsymbol{c}^2}{c_0^2}\right), \tag{1.13}$$

for a fixed (equilibrium value of) temperature T_0 and number density n_0. The most probable thermal speed of the global equilibrium state is $c_0 = \sqrt{2RT_0}$, where R is the specific gas constant. The distribution function is decomposed to form

$$f\left(\boldsymbol{x}, \boldsymbol{c}, t\right) = f_0\left(\boldsymbol{c}\right) + f_d\left(\boldsymbol{x}, \boldsymbol{c}, t\right), \tag{1.14}$$

where f_d is represented by the simulation of deviational particles. The relationship between the particle weight $\mathcal{W}$ (analogous to the number of real molecules rep-

resented by a DSMC particle) and $\mathcal{N}$ is non-linear (unlike the linear relationship between W and N of the DSMC method), and is expressed as

$$\mathcal{W} = \frac{\epsilon\, \rho_0\, V_{\texttt{cell}}}{m\, \Xi}\,, \tag{1.15}$$

where ϵ is a dimensionless parameter than quantifies the departure from equilibrium, ρ_0 is the equilibrium value of mass density ρ, m is the molecular mass [kg], and Ξ is approximately the average number of deviational particles per cell. In addition, because f_d can take either a positive or negative sign (see Fig. 1.7 for an illustration of this concept), the particle sign $s_p \in [-1, 1]$ is introduced.

The implementation of the LVDSMC method used herein, employs Strang's splitting method (see Ohwada [1998]). For a time step Δt, the procedure begins by translating all particles over the interval $1/2\Delta t$. If a body force is applied, it acts following this half advection step, again for the interval $1/2\Delta t$. A full collision step then occurs over the interval Δt. Next, the body force acts again for the interval $1/2\Delta t$. Finally, all particles are again translated over the interval $1/2\Delta t$, before properties are sampled. Clearly, as with the DSMC method, advection and collision steps occur separately. If we considered the Boltzmann equation in terms of the deviational distribution function f_d, we obtain the following [Radtke, 2011]:

$$\left[\frac{\partial f_d}{\partial t} + \boldsymbol{c} \cdot \frac{\partial f_d}{\partial \boldsymbol{x}}\right]_{\texttt{tran.}} = 0\,, \tag{1.16}$$

$$\left[\frac{\partial f_d}{\partial t}\right]_{\texttt{coll.}} = \mathcal{J}\left[f_0 + f_d, f_0 + f_d\right] = \mathcal{L}\left[f_d\right] + \mathcal{J}\left[f_d, f_d\right]\,, \tag{1.17}$$

where equations (1.16) and (1.17) describe the advection and collision of particles, respectively. Like representative particles, deviational particles are translated according to $\boldsymbol{x}\left(t + \Delta t\right) = \boldsymbol{x}\left(t\right) + \boldsymbol{c}\left(t\right) \Delta t_{1/2}$, where $\Delta t_{1/2}$ is the half-time step.

The collision operator (in equation (1.17)), which is here defined by the VHS model, is split to form linear $\left(\mathcal{L}\left[f_d\right]\right)$ and non-linear $\left(\mathcal{J}\left[f_d, f_d\right]\right)$ components. The effect of the latter is negligible when considering near-equilibrium flows, and is disregarded. Therefore, the collision operator is $\mathcal{L}\left[f_d\right]$, which is more dominant.

Effective body force

Using a technique introduced by Cercignani and Daneri [1963], the LVDSMC method is able to represent streamwise gradients as an effective body force. By assuming that the streamwise dependence is carried by the underlying equilibrium state, this feature allows streamwise pressure and temperature gradients to be set independently.

The scaled gradients

$$-\phi_p = \frac{1}{p}\frac{\mathrm{d}p}{\mathrm{d}s} \ , \text{ and } \phi_T = \frac{1}{T}\frac{\mathrm{d}T}{\mathrm{d}s} \ , \tag{1.18}$$

are treated as input parameters, and are used directly to define an additional term in the advection operator (equation (1.16)). All IMM computations presented in this thesis make use of this feature. For further details, see Radtke [2011].

1.3 Thesis outline

In Chapter 2, a steady-state internal-flow multiscale method (IMM) for gas flows (which is referred to herein as the steady-IMM) is developed. This method features a number of extensions that differentiates it from the dense-fluid-flow IMM of Borg et al. [2013a]. These include: incorporation of fluid compressibility; support for streamwise non-isothermality; adaptation to Monte Carlo simulation methods for gases; and implementation of pseudospectral methods for far-improved accuracy.

In Chapter 3, the steady-IMM for gas flows is verified by comparison of its solutions with those obtained by the DSMC method (alternative methods are used when solution of the problem by the DSMC method is computationally intractable). Six test cases are considered to verify the steady-IMM: cases one and two involve the simulation of body-force-driven and pressure-driven flows through a converging-diverging conduit, respectively; case three simulates a shear-driven flow through a micro-gas journal bearing; cases four, five, and six consist of non-isothermal (thermal-transpiration) flows through various geometries.

Chapter 4 outlines the numerical and multiscale methodology that constitutes the unsteady-IMM for gas flows. This method is validated by comparison with the time-dependent thermal-transpiration results of Rojas-Cárdenas et al. [2013] for various streamwise temperature variations and values of Kn.

The influence of various geometric parameters on the performance of thermal-transpiration compressors (and implicitly Knudsen compressors) is investigated in Chapter 5. Both steady and unsteady implementations of the IMM for gas flows (presented in this thesis) are employed to recommended compressor designs which maximise performance. We demonstrate the IMM as an effective tool for the design optimisation of these devices, as opposed to a simulation tool.

The key developments and findings of this work are outlined in Chapter 6, accompanied by a discussion of future work and potential applications of the IMM.

Chapter 2

IMM for steady gas flows: methodology

In this chapter, a method for modelling steady rarefied gas flows in high-aspect-ratio conduits is developed. This method, referred to as the steady-internal-flow multiscale method (steady-IMM), is an extension of the hybrid approach proposed by Borg et al. [2013a] for the simulation of multiscale dense-fluid flows in conduits of high aspect ratio. The need for the steady-IMM is apparent when considering the many important and emerging micro/nano-technologies that involve the large class of low-speed rarefied gas flows the method is designed to treat.

Like the IMM for dense-fluid flows, the steady-IMM (for gas flows) couples particle-based 'micro subdomain' instances and a macro domain, the flow conditions through which are described by continuum theory (the continuum formulation of conservation of mass and momentum). These subdomains represent the local cross-sectional geometry of the macro domain, and are distributed in the streamwise direction with a spacing dictated by the configuration of the problem. Application of the steady-IMM requires that a degree of length-scale separation exists between macroscopic variations in the streamwise (s-)direction and microscopic processes occurring in the transverse (xy-)plane. Rarefied gas flows in high-aspect-ratio conduits (see Fig. 2.1) exhibit such scale-sepeartion. In the following, the major extensions that distinguish the steady-IMM from that of Borg et al. [2013a] are outlined.

In Borg et al. [2013a] it is assumed that the low-speed dense-fluid flow in microdevices is incompressible. However, despite the low Reynolds and Mach numbers (to which we restrict our attention) of such flows, significant compressiblity can occur [Gad-el Hak, 2005], particularly in dilute gases. In Borg et al. [2013a], even though a dense Lennard-Jones fluid was considered, a significant error due to the incompressibility assumption was identified. This observation is due to the significant variations in density that occur as a result of the combination of high viscous losses and the substantial streamwise length of the high-aspect-ratio conduits considered.

Therefore, as will be shown, the steady-IMM incorporates fluid compressibility.

Since micro-solver instances (subdomains) require considerable computational effort, continous variations of functions, such as the streamwise variation of mass density, should be reconstructed from the values of mass flow rate (measured directly from the streamwise-distributed subdomains) using a method that provides excellent accuracy and convergence characteristcs. To this end, we adopt pseudospectral methods, which exhibit so-called 'exponential' convergence: increasing the number of collocation points (i.e. the number of subdomains Π per streamwise length, Π/L_s) decreases the error exponentially, i.e. $\propto \left(L_s/\Pi\right)^{\Pi}$. Finite-difference methods (which offer an alternative approach for the solution of problems by the steady-IMM) do not share this rate of convergence; generally, the accuracy of finite-difference methods is inferior to that of pseudospectral methods.

To treat a gas flow, Monte Carlo methods (e.g. the direct simulation Monte Carlo (DSMC) method or the low-variance deviational simulation Monte Carlo (LVDSMC) method) provide micro resolution (by simulating the flow in micro subdomains). In Chapters 3, 4, and 5, the LVDSMC method is used solely (due to its efficient treatment of low-signal flows). This method simulates streamwise gradients as an effective body force, and negates the need to include computational cells in the streamwise direction. Therefore, in the case of a three-dimensional macro domain, LVDSMC subdomain instances are simply two-dimensional 'slices' in the xy-plane (of the macro domain). For a two-dimensional macro domain, a one-dimensional implementation of the LVDSMC method is used.

Other major extensions allow for non-isothermal conditions (to model thermal transpiration) and the treatment of a broader range of flow problems: periodic, body-force-driven, pressure-driven, thermally-driven, and shear-driven. Support for these is provided by the underlying equations that are presented in what follows.

2.1 Macro model

Consider the continuity equation,

$$\frac{\partial \rho}{\partial t} + \nabla \cdot (\rho \mathbf{U}) = 0\,, \tag{2.1}$$

where ρ is the mass density, $\mathbf{U} = (u, v, w)$ is the convective velocity, and t is time. By the locally-parallel flow assumption ($u = v = 0$), equation (2.1) becomes

$$\frac{\partial \rho}{\partial t} + \frac{\partial}{\partial s} (\rho w) = 0\,. \tag{2.2}$$

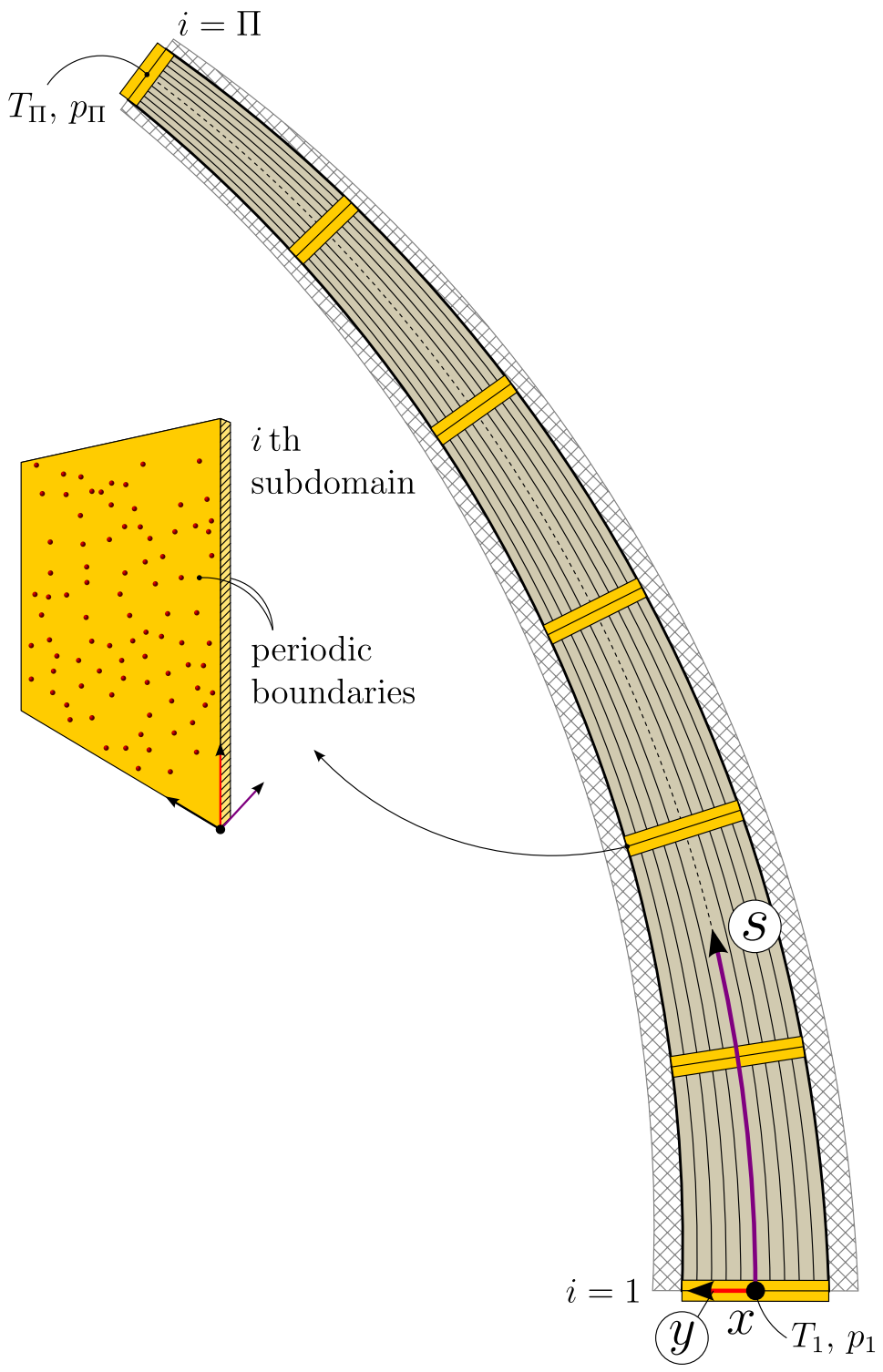

Figure 2.1: A generic internal-flow geometry with the steady-IMM applied.

Integrating equation (2.2) over the cross-sectional area A of the conduit gives

$$\frac{\partial \rho}{\partial t} + \frac{1}{A}\frac{\partial \dot{m}}{\partial s} = 0\,, \tag{2.3}$$

where the mass flow rate is defined as

$$\dot{m} = \int_A \rho w \, \mathrm{d}A\,. \tag{2.4}$$

Combining equation (2.3) with an equation of state $p = f(\rho, T)$, where p is the pressure and T is the temperature, constitutes the macro model. Assuming that macro state variables are known at the boundaries of the flow/conduit, the mass flow rate as a function of s is all that is required to close the macro model; this variation is determined from Π streamwise distributed micro-solver instances (subdomains), which provide solutions of the micro model. We consider the temporal evolution of the mass flow rate in each micro subdomain to be governed by

$$\frac{\partial \dot{m}}{\partial t} = \mathcal{F}\left(\frac{\partial T}{\partial s}\,; \frac{\partial p}{\partial s}\,; \mathcal{X}\right)\,, \tag{2.5}$$

where $\mathcal{F}$ represents the micro model, and the container $\mathcal{X}$ holds information regarding the molecular structure of the gas being modelled.

Many problems involve spatial and temporal scale separation between the micro and macro model. For such cases, the asynchronous time-step coupling approach described in E et al. [2009]; Lockerby et al. [2013] is adopted; the micro and macro model are advanced at different rates with negligible accuracy penalty. For the underlying methodology of the (transient) unsteady-IMM, refer to Chapter 4. For steady-flow problems, the system does not evolve in time. Instead, the time-dependent term in equation (2.3) is omitted, and the steady continuity equation can be discretised at streamwise-distributed collocation points (subdomains):

$$\left.\frac{1}{A_i}\frac{\partial \dot{m}}{\partial s}\right|_i = 0 \qquad \text{for } i = 1, 2, \ldots, \Pi\,. \tag{2.6}$$

The collocation points (nodes on the centreline of the macro domain) are the geometric centres of Π micro subdomains. Pseudospectral methods are employed by the steady-IMM to obtain density and its spatial derivative (at these collocation points) from the mass flow rate in subdomains. Equation (2.6) can be expressed as

$$\langle \dot{m}_i \rangle = \text{const.} = \dot{M} \qquad \text{for } i = 1, 2, \ldots, \Pi\,, \tag{2.7}$$

where $\langle \dot{m}_i \rangle$ is the mass flow rate generated (by a body force) in the i th of Π subdo-

mains. Chevrons denote that the mass flow rate is measured directly from the ith micro subdomain. $\dot{M}$ is the macroscopic mass flow rate through the conduit, which is iteratively refined. Note, for steady-flow problems, a conservative rule-of-thumb is to use $\Pi = \lceil 8/3\, S_L \rceil$ subdomains, where S_L is the length-scale separation number.

2.2 Micro model

The equation for conservation of momentum is

$$\rho \left[\frac{\partial \mathbf{U}}{\partial t} + (\mathbf{U} \cdot \nabla)\, \mathbf{U} \right] = -\nabla p + \nabla \cdot \mathbb{T} + \mathbf{f}\,, \tag{2.8}$$

where $\mathbb{T}$ is the shear stress tensor and $\mathbf{f}$ is a body force per unit volume, which describes the momentum transport of a fluid. By restricting our attention to steady laminar flows (low Reynolds and Mach numbers) in high-aspect-ratio conduits (i.e. locally-parallel flow, $u = v = 0$), equation (2.8) can be linearised:

$$\frac{\partial p}{\partial s} = \nabla p = \nabla \cdot \mathbb{T} + \mathbf{f}\,. \tag{2.9}$$

For individual decoupled subdomains, a different momentum balance is formed

$$0 = \nabla \cdot \mathbb{T} + \mathbf{f}\,. \tag{2.10}$$

Due to the streamwise periodicity of the subdomains, the streamwise pressure gradient occurring in equation (2.10) cannot exist. Equations (2.9) and (2.10) are therefore inconsistent. To facilitate a coupling mechanism between micro and macro models, a streamwise pressure gradient is emulated by the application of a fictitious body force Φ, referred to as a pressure-gradient correction in Borg et al. [2013a].

2.3 Macro-micro coupling

The macro-micro coupling is stated in equation (2.7). The steady-IMM is iterative, predicting values of Φ_i and ρ_i for $i = 1, 2, \ldots, \Pi$ which generate micro mass-flow responses that, on convergence, satisfy equation (2.7). The macroscopic mass flow rate $\dot{M}$ and the (continuous) streamwise variation of mass density constitute the basic outputs of the steady-IMM. Other macroscopic quantities, such as pressure, are related to density by an equation of state. If the conduit is three-dimensional, streamwise velocity profiles $w\,(x, y)$ can be extracted from subdomain instances. For two-dimensional conduits, one-dimensional velocity profiles $w\,(y)$ are obtained.

Consider the i th subdomain. The iterative solution of equation (2.7) requires a prediction of the general response of the micro mass flow rate $\langle \dot{m}_i \rangle$ to changes of Φ_i and ρ_i. It is assumed that the difference between $\langle \dot{m}_i \rangle$ and the mass flow rate due directly to wall motion ($\rho_i Q_i$) is separately proportional to the net momentum flux (introduced by an external acceleration a and the pressure-gradient correction Φ_i) and the streamwise surface temperature gradient. This is stated as

$$\langle \dot{m}_i \rangle = k_i \left(\rho_i a - \Phi_i \right) + \rho_i Q_i + j_i \left. \frac{\mathrm{d}T}{\mathrm{d}s} \right|_i . \tag{2.11}$$

The constant of proportionality k_i is estimated prior to the first iteration. As will be shown, the constant j_i, determining the mass flow rate due to thermal transpiration, does not require estimation. Note, the prediction implied by equation (2.11) only determines the convergence characteristics of the method, and does not affect the accuracy of the final solution (provided one can be found). Equation (2.11) is used to estimate the change in mass flow rate between successive iterations:

$$\dot{m}_i^{\ell+1} - \left\langle \dot{m}_i^{\ell} \right\rangle = k_i \left(\rho_i^{\ell+1} a - \rho_i^{\ell} a - \Phi_i^{\ell+1} + \Phi_i^{\ell} \right) + Q_i \left(\rho_i^{\ell+1} - \rho_i^{\ell} \right) , \tag{2.12}$$

where ℓ is the iteration index. Because it is assumed that the surface temperature gradient, which enables thermal transpiration, is unaffected by ρ and Φ, it has been disregarded in equation (2.12). The simulations of Akhlaghi and Roohi [2014] demonstrate that, for high degrees of rarefaction, this assumption is questionable. However, as already stated, such an inaccuracy only affects the convergence characteristics of the iterative procedure, and not the accuracy of the final solution.

So that successive values of $\langle \dot{m}_i \rangle$ tend to a single macroscopic value:

$$\dot{M} + k_i \left(\Phi_i^{\ell+1} - \rho_i^{\ell+1} a \right) - Q_i \rho_i^{\ell+1} = \left\langle \dot{m}_i^{\ell} \right\rangle + k_i \left(\Phi_i^{\ell} - \rho_i^{\ell} a \right) - Q_i \rho_i^{\ell} , \tag{2.13}$$

where $\dot{M}$ replaces $\dot{m}_i^{\ell+1}$ in equation (2.12). As ρ_i and Φ_i converge ($\rho_i^{l+1} \to \rho_i^{l}$ and $\Phi_i^{l+1} \to \Phi_i^{l}$), equation (2.13) enforces macroscopic mass conservation, $\left\langle \dot{m}_i^{l} \right\rangle \to \dot{M}$.

By an equation of state, Φ includes the contribution of the surface temperature gradient. For ideal gases, the pressure-gradient correction is expressed as,

$$\Phi_i^{\ell+1} = R T_i \left. \frac{\mathrm{d}\rho}{\mathrm{d}s} \right|_i^{\ell+1} + R \left. \frac{\mathrm{d}T}{\mathrm{d}s} \right|_i \rho_i^{\ell+1} , \tag{2.14}$$

where R is the specific gas constant. Monatomic rarefied gases are modelled accurately as ideal gases; a more complex equation of state is not necessary.

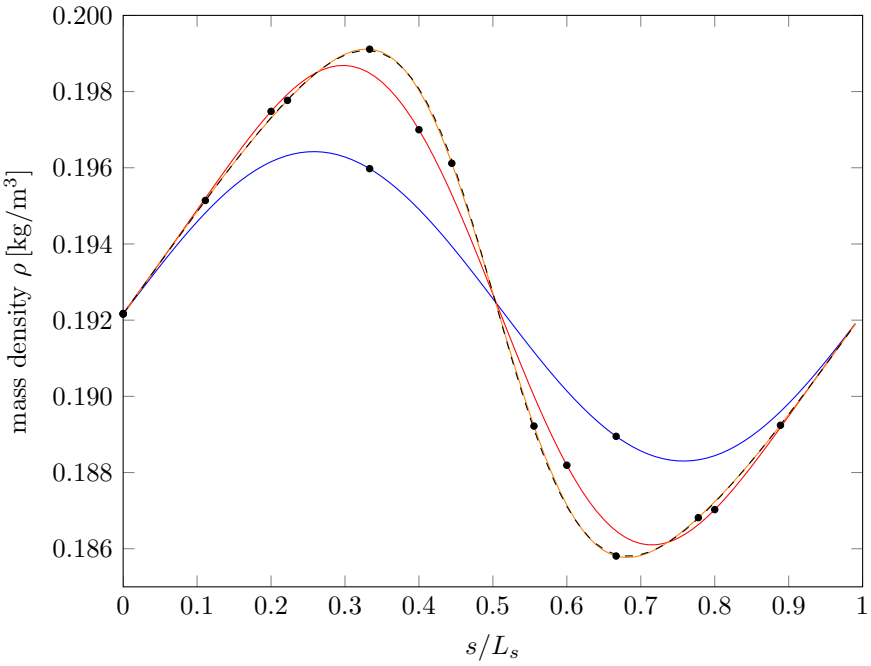

Figure 2.2: Rate of 'exponential' convergence: comparison of the solutions from the steady-IMM, with predictions of $\langle \dot{m}_i \rangle$ for $i = 1, 2, \ldots, \Pi$ provided by a simple slip solver. Trigonometric interpolation is used in $\Pi = 3$ (——), $\Pi = 5$ (——) and $\Pi = 9$ (——) equispaced collocation points. The highly accurate solution is the dashed line.

At each iteration, equations (2.13) and (2.14) are solved simultaneously, producing sequentially improving predictions of $\dot{M}$, ρ_i and Φ_i; the latter two variables are reapplied to update the individual subdomain states. From equation (2.14), the density and its spatial derivative (the temperature and its spatial derivative do not vary between iterations) are required at $i = 1, 2, \ldots, \Pi$ points to obtain values of $\Phi_i^{\ell+1}$. To this end, pseudospectral methods (boasting exceptional accuracy and convergence characteristics) are employed to obtain values of ρ_i and Φ_i at $\ell + 1$.

2.4 Pseudospectral methods

Since accuracy is crucial to the solution of problems by the steady-IMM, pseudospectral methods are used to obtain numerical approximations of $\Phi_i^{\ell+1}$ and $\rho_i^{\ell+1}$ in equation (2.14). For a sufficiently smooth function, the typical convergence rate is 'exponential' (or of 'infinite order'), which is highly desirable (demonstrated in Fig. 2.2). Minimising the number of collocation points (computationally intensive micro-solver instances) required to precisely represent density and its derivative, greatly enhances the computational efficiency of the steady-IMM.

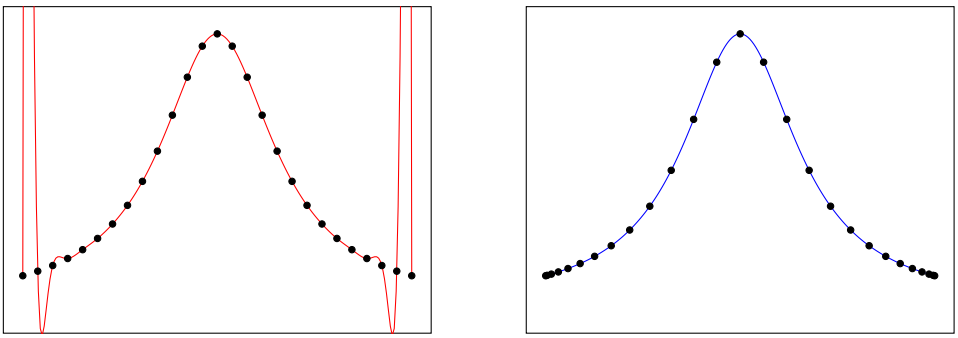

Figure 2.3: Comparison of interpolation of function in equispaced points (——), and Chebyshev points (——). If a smooth function is interpolated by a polynomial in equispaced points, error increases with the degree of the polynomial: Runge's phenomenon. By interpolating in Chebyshev points, error decreases geometrically.

The periodicity of the problem dictates the nature of the pseudospectral method, and implicitly the spacing of the collocation points. Problems with streamwise-periodic boundary conditions can be tackled by trigonometric interpolation in equispaced points. For problems confined to non-periodic (macro) domains, polynomial interpolation in Chebyshev points, defined on the interval $[0, L_s]$ by

$$s_{k+1} = \frac{L_s}{2}\left[1 - \cos\left(\frac{k}{\Pi - 1}\,\pi\right)\right] \qquad \text{for } k = 0, 1, \ldots, \Pi - 1\,, \tag{2.15}$$

is used. Polynomial interpolation in equispaced points will result in undesirable oscillations at the limits of the interval (as shown in Fig. 2.3) [Runge, 1901]: this is known as Runge's phenomenon. However, polynomial interpolation in Chebyshev points (Chebyshev interpolation), which are distributed more densely at the limits of the interval (to compensate for the *one-sided* approximation of $\rho\,(s)$, and implicitly $\Phi\,(s)$, near $s = 0, L_s$ [Boyd, 2001]), minimises this effect and gives *very* uniform accuracy over the entire interval [Boyd, 2001; Shizgal, 2015].

2.4.1 Trigonometric interpolation

For the calculation of a streamwise-periodic flow by the steady-IMM, a Fourier series expansion is used to represent $\rho\,(s)$ in terms of a sum of simple trigonometric functions. The derivative of $\rho\,(s)$ is obtained by the term by term differentiation of the expansion of $\rho\,(s)$. The expansion of the streamwise-periodic function $\rho\,(s)$ is

$$\rho\,(s) = \hat{\rho}_1 + \sum_{j\,=\,1}^{(\Pi-1)/2} \left(\hat{\rho}_{2j}\sin\left(2\pi s\,j/L_s\right) + \hat{\rho}_{2j+1}\cos\left(2\pi s\,j/L_s\right)\right)\,, \tag{2.16}$$

where $\hat{\rho}_{1,2,\ldots,\Pi}$ are the Fourier coefficients (note, Π must be odd). Therefore, $\Phi(s)$ is given by substituting equation (2.16) and its derivative into equation (2.14):

$$\Phi(s) = \frac{2\pi RT}{L_s} \sum_{j=1}^{(\Pi-1)/2} \left(j\hat{\rho}_{2j} \cos\left(2\pi s\, j/L_s\right) - j\hat{\rho}_{2j+1} \sin\left(2\pi s\, j/L_s\right) \right) + R\frac{\mathrm{d}T}{\mathrm{d}s} \left[\hat{\rho}_1 + \sum_{j=1}^{(\Pi-1)/2} \left(\hat{\rho}_{2j} \sin\left(2\pi s\, j/L_s\right) + \hat{\rho}_{2j+1} \cos\left(2\pi s\, j/L_s\right) \right) \right] . \quad (2.17)$$

Equations (2.16) and (2.17) are evaluated at

$$s_i = L_s\,(i-1)\,/\Pi \qquad \text{for } i = 1, 2, \ldots, \Pi\,, \quad (2.18)$$

to give variables in physical space

$$\rho_i^{\ell+1} = \hat{\rho}_1 + \sum_{j=1}^{(\Pi-1)/2} \left(\hat{\rho}_{2j} \sin\left(2\pi s_i\, j/L_s\right) + \hat{\rho}_{2j+1} \cos\left(2\pi s_i\, j/L_s\right) \right) , \quad (2.19)$$

and

$$\Phi_i^{\ell+1} = \frac{2\pi RT_i}{L_s} \sum_{j=1}^{(\Pi-1)/2} \left(j\hat{\rho}_{2j} \cos\left(2\pi s_i\, j/L_s\right) - j\hat{\rho}_{2j+1} \sin\left(2\pi s_i\, j/L_s\right) \right) + R\left.\frac{\mathrm{d}T}{\mathrm{d}s}\right|_i \left[\hat{\rho}_1 + \sum_{j=1}^{(\Pi-1)/2} \left(\hat{\rho}_{2j} \sin\left(2\pi s_i\, j/L_s\right) + \hat{\rho}_{2j+1} \cos\left(2\pi s_i\, j/L_s\right) \right) \right] , \quad (2.20)$$

at the next iteration, $\ell+1$. Iteration indices for the Fourier coefficients are omitted for clarity. Equations (2.19) and (2.20) are substituted into equation (2.13) to obtain

$$\dot{M} + k_i \left\{ \frac{2\pi RT_i}{L_s} \sum_{j=1}^{(\Pi-1)/2} \left(j\hat{\rho}_{2j} \cos\left(2\pi s_i\, j/L_s\right) - j\hat{\rho}_{2j+1} \sin\left(2\pi s_i\, j/L_s\right) \right) + R\left.\frac{\mathrm{d}T}{\mathrm{d}s}\right|_i \left[\hat{\rho}_1 + \sum_{j=1}^{(\Pi-1)/2} \left(\hat{\rho}_{2j} \sin\left(2\pi s_i\, j/L_s\right) + \hat{\rho}_{2j+1} \cos\left(2\pi s_i\, j/L_s\right) \right) \right] \right\} = \left\langle \dot{m}_i^{\ell} \right\rangle + k_i \left(\Phi_i^{\ell} - \rho_i^{\ell} a \right) - Q_i \rho_i^{\ell}\,. \quad (2.21)$$

Equation (2.21) represents Π equations, consisting of $\Pi + 1$ variables ($\hat{\rho}_{1,2,\ldots,\Pi}$ and $\dot{M}$). For a fully determined system, an equation for total mass is introduced (for periodic problems this is known and fixed from the outset):

$$M = \iiint_V \rho \, \mathrm{d}x \, \mathrm{d}y \, \mathrm{d}s \approx \frac{L_s}{\Pi} \sum_{i=1}^{\Pi} A_i \rho_i^{\ell+1}$$
$$\approx \frac{L_s}{\Pi} \sum_{i=1}^{\Pi} A_i \left[\hat{\rho}_1 + \sum_{j=1}^{(\Pi-1)/2} \left(\hat{\rho}_{2j} \sin\left(2\pi s_i \, j/L_s\right) + \hat{\rho}_{2j+1} \cos\left(2\pi s_i \, j/L_s\right) \right) \right] , \tag{2.22}$$

where A_i is the cross-sectional area of the geometry at the ith collocation point. The trapezoidal rule, the rate of convergence of which is excellent for smooth and periodic integrands [Weideman, 2002], is used to form equation (2.22) (the mean of the variables at the collocation points multiplied by L_s).

The system of linear equations (formed by equations (2.21) and (2.22)), can be solved at each iteration using LU decomposition, or similar. Once the Fourier coefficients are known, values of ρ_i and Φ_i (in physical space), at the ith node (subdomain) can be obtained from equations (2.19) and (2.20).

2.4.2 Polynomial (Chebyshev) interpolation

If the macro domain is non-periodic, a Fourier series expansion for the approximation of $\rho(s)$ and $\Phi(s)$ is undesirable (a Fourier series can only faithfully represent periodic functions). To evaluate the density and its derivative in equation (2.14), polynomial interpolation is used. The density variation is represented by

$$\rho(s) = \sum_{j=0}^{\Pi} \hat{\rho}_j s^j \, . \tag{2.23}$$

From equation (2.14), a polynomial description of $\Phi(s)$ is formed

$$\Phi(s) = RT(s) \sum_{j=1}^{\Pi} j \hat{\rho}_j s^{j-1} + R \frac{\mathrm{d}T(s)}{\mathrm{d}s} \sum_{j=0}^{\Pi} \hat{\rho}_j s^j \, . \tag{2.24}$$

To minimise the effect of Runge's phenomenon (and ensure accuracy over the entire interval $[0, L_s]$ as with trigonometric interpolation), equations (2.23) and (2.24) are evaluated at Chebyshev points (hence, more specifically, this is an application of Chebyshev interpolation [Boyd, 2001]) defined on the interval $[0, L_s]$ by

$$s_{k+1} = \frac{L_s}{2} \left[1 - \cos\left(\frac{k}{\Pi - 1} \pi \right) \right] \qquad \text{for } k = 0, 1, \ldots, \Pi - 1 \, , \tag{2.25}$$

to give, for $i = 1, 2, \ldots, \Pi$, variables in physical space

$$\rho_i^{\ell+1} = \sum_{j=0}^{\Pi} \hat{\rho}_j s_i^j \,, \tag{2.26}$$

$$\Phi_i^{\ell+1} = RT_i \sum_{j=1}^{\Pi} j\hat{\rho}_j s_i^{j-1} + R \left.\frac{\mathrm{d}T}{\mathrm{d}s}\right|_i \sum_{j=0}^{\Pi} \hat{\rho}_j s_i^j \,, \tag{2.27}$$

at the next iteration, $\ell + 1$. Iteration indices for the Fourier coefficients are omitted for clarity. Equations (2.26) and (2.27) are substituted into equation (2.13) to obtain

$$\dot{M} + k_i \left(RT_i \sum_{j=1}^{\Pi} j\hat{\rho}_j s_i^{j-1} + R \left.\frac{\mathrm{d}T}{\mathrm{d}s}\right|_i \sum_{j=0}^{\Pi} \hat{\rho}_j s_i^j \right) - \left(\sum_{j=0}^{\Pi} \hat{\rho}_j s_i^j \right) (k_i a + Q_i)$$

$$= \left\langle \dot{m}_i^l \right\rangle + k_i \left(\Phi_i^l - \rho_i^l a \right) - Q_i \rho_i^l \,. \tag{2.28}$$

Equation (2.28) represents Π equations containing $\Pi + 2$ variables. For a fully determined system, the boundary conditions on pressure at the inlet and outlet,

$$p_1 = RT_1 \hat{\rho}_0 \,, \tag{2.29}$$

$$p_\Pi = RT_\Pi \sum_{j=0}^{\Pi} \hat{\rho}_j L_s^j \,, \tag{2.30}$$

must be considered.

The system of linear equations (formed by equations (2.28), (2.29) and (2.30)), can be solved at each iteration using LU decomposition, or similar. Once the coefficients of the polynomial are known, values of ρ_i and Φ_i (in physical space) at the i th node (subdomain) can be obtained from equations (2.26) and (2.27). An alternative method of solution is to introduce a mass flow rate condition in place of Dirichlet boundary conditions on pressure (equations (2.29) or (2.30)). For example,

$$\dot{M} = 0 \,. \tag{2.31}$$

The ability to invert the problem in this manner is discussed in the following chapter.

2.5 Boundary conditions

It has been shown that the macro domain can be constrained (at the inlet/outlet) by streamwise-periodic boundary conditions or boundary conditions on pressure.

In addition to these boundary conditions, which are prescribed at the inlet/outlet, a streamwise temperature gradient or velocity can be imposed on the surfaces of the conduit. By prescribing a streamwise velocity (normal velocity is assumed zero), a shear-driven flow can be modelled. This may be used to model gas lubrication layers, for example. It may also be used to study the thin film of gas that has recently been shown to exist between droplets and solid surfaces [de Ruiter et al., 2015]. The imposition of a streamwise temperature gradient on the surfaces of the conduit is useful in the study of thermal transpiration (and more generally, thermal creep). This capability of the steady-IMM is used extensively throughout this thesis.

2.6 Coupling algorithm

The steady-IMM generates a sequence of improving approximate values of pressure-gradient correction and density at collocation points (subdomain instances). A convergence (stoppage) criterion is used to control the number of iterations. On convergence, the mass flow rates generated in each subdomain are equal, and macroscopic mass is conserved. The steady-IMM follows the procedure outlined below:

Algorithm 1 The steady internal-flow multiscale method

1: **procedure** STEADYIMM ▷ steady-IMM

Require: set Q_i, T_i', a_i ▷ boundary conditions for $i = 1, \ldots, \Pi$
Require: set $T_i, \rho_i^{\ell=0}$ ▷ thermodynamic conditions for $i = 1, \ldots, \Pi$
Require: set $L_{y,i}, a_{\text{int.},i}, s_i$ ▷ other conditions for $i = 1, \ldots, \Pi$
Require: set V, Π ▷ scalar values

2: **for** $i \leftarrow 1, \Pi$ **do** ▷ loop over all (Π) subdomains
3: INITIALISE$(T_i, T_i' = 0, \Phi_i^{\ell=0}, \rho_i^{\ell=0})$ ▷ initialise i th subdomain
4: RUN(i) ▷ command execution of i th subdomain
5: **end for**

6: BLOCK(Π) ▷ wait for time stepping of all subdomains to finish

7: **for** $i \leftarrow 1, \Pi$ **do** ▷ loop over all (Π) subdomains
8: MDOT$(i, \left\langle \dot{m}_i^{\ell=0} \right\rangle)$ ▷ obtain $\left\langle \dot{m}_i^{\ell=0} \right\rangle$ for i th subdomain
9: $k_i \leftarrow \left(\left\langle \dot{m}_i^{\ell=0} \right\rangle - Q_i \rho_i^{\ell=0} \right) / \left(\rho_i^{\ell=0} a_{\text{int.},i} \right)$ ▷ k_i for i th subdomain
10: **end for**
11: $\ell \leftarrow 1$

Prior to initiation of the iteration loop (starting at the while loop in algorithm 2),

a set of Π simulations must be performed in order to generate values of k_i. This is achieved by applying no temperature gradient (even if non-zero) and an arbitrary pressure gradient Φ_i in each subdomain. The mass flow rate measured from each subdomain is then used to obtain values of k_i directly from equation (2.11).

Algorithm 2 Part II: the unsteady internal-flow multiscale method

12: **while** convergence criterion is unsatisfied **do**
13: **for** $i \leftarrow 1, \Pi$ **do** ▷ loop over all (Π) subdomains
14: **if** periodic configuration **then**
▷ linear equations (2.21), (2.22) are used to solve:
15: SOLVEFOURIER$(T_i, T_i', k_i, \Phi_i^{\ell-1}, \rho_i^{\ell-1}, \Phi_i^{\ell}, \rho_i^{\ell})$ ▷ solve for $\Phi_i^{\ell}, \rho_i^{\ell}$
16: **else**
▷ linear equations (2.28), (2.29), (2.30) are used to solve:
17: SOLVE$(T_i, T_i', k_i, \Phi_i^{\ell-1}, \rho_i^{\ell-1}, \Phi_i^{\ell}, \rho_i^{\ell})$ ▷ solve for $\Phi_i^{\ell}, \rho_i^{\ell}$
18: **end if**
19: INITIALISE$(T_i, T_i', \Phi_i^{\ell}, \rho_i^{\ell})$ ▷ initialise i th subdomain at ℓ th iteration
20: RUN(i) ▷ command execution of i th subdomain at ℓ th iteration
21: **end for**

22: BLOCK(Π) ▷ wait for time stepping of all subdomains to finish

23: **for** $i \leftarrow 1, \Pi$ **do** ▷ loop over all (Π) subdomains
24: MDOT$(i, \left\langle \dot{m}_i^{\ell} \right\rangle)$ ▷ obtain $\left\langle \dot{m}_i^{\ell} \right\rangle$ for i th subdomain at ℓ th iteration
25: **end for**

26: $\ell \leftarrow \ell + 1$
27: **end while**
28: **end procedure**

The steady-IMM allows for the use of any suitable micro solver. Pipelines (of Unix-like operating systems) are used to communicate instructions to the micro solver. If, however, the micro solver (process) cannot read commands from standard input (stdin), an alternative means of communication must be developed.

The computational requirements of the steady-IMM are trivial. The highly-efficient Linear Algebra Package (LAPACK) software library is used to perform the matrix inversion for the calculation of $\hat{\rho}_{1,2,\ldots,\Pi}$ and $\dot{M}$ every iteration.

In the next chapter, we apply the steady-IMM to model a number of flow systems. To verify every aspect of the method's implementation, pressure-driven, shear-driven, and thermally-driven flows are all modelled. Due to its exceptionally high computational efficiency in the low-signal limit, the low-variance deviational simulation Monte Carlo method is used exclusively to provide micro resolution.

Chapter 3

IMM for steady gas flows: verification and results

In this chapter, the steady-internal-flow multiscale method (steady-IMM) for gas flows, developed in Chapter 2, is verified. The solutions computed by the steady-IMM are compared to those obtained by conventional particle-based (non-hybrid) simulations; if it is computationally feasible to obtain, the direct simulation Monte Carlo (DSMC) method provides the reference solution (for verification). When simulating low-signal (e.g. low-Mach number) flows, traditional particle-based methods, such as the DSMC method, suffer from overwhelming statistical noise; a large number of independent samples are required. In fact, some problems are too computationally intensive to solve using these standard methods. For this reason, we employ the low-variance deviational simulation Monte Carlo (LVDSMC) method (highly efficient for low-signal flows) as our micro solver, and not the DSMC method.

3.1 Isothermal problems

The following cases verify the steady-IMM for isothermal conditions. For most cases, reference solutions are obtained by the computationally demanding DSMC method. Body-force-driven, pressure-driven, and shear-driven flows are all modelled.

3.1.1 Converging-diverging channel: external acceleration

To begin, the steady-IMM is applied to resolve the three-dimensional body-force-driven flow in a converging-diverging channel (illustrated in Fig. 3.1a). The width and streamwise length of the channel are $L_x = 0.5\,\mu\text{m}$ and $L_s = 24\,\mu\text{m}$, respectively; the height L_y ranges from $0.3\,\mu\text{m}$ to $0.5\,\mu\text{m}$. The minimum value of the scale separation number, as calculated by equation (1.8), is $S_L = 23.5$. The average mass density (a constant value) is $\bar{\rho} = 42.93 \times 10^{-3}\,\text{kg}\,\text{m}^{-3}$. The modelled gas is variable hard sphere (VHS) argon ($\omega = 0.81$), and the temperature is $T = 273\,\text{K}$.

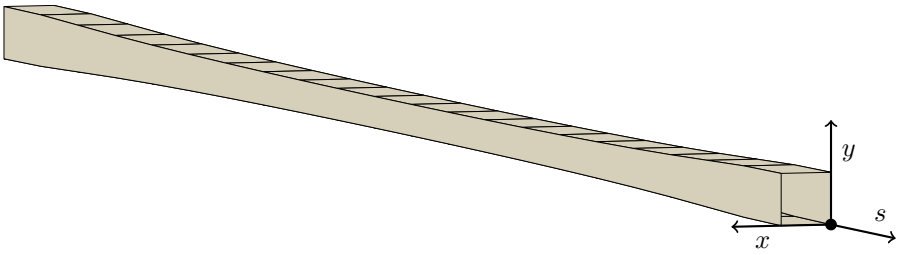

(a) A converging-diverging channel.

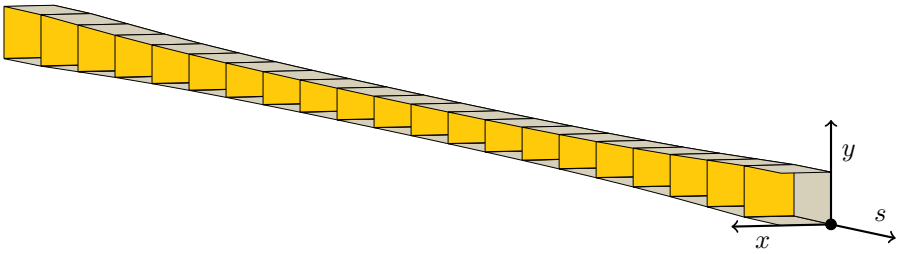

(b) For $\Pi = 21$, a converging-diverging channel: streamwise periodic.

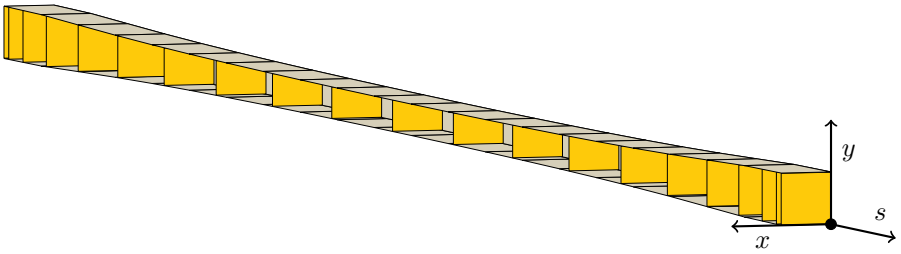

(c) For $\Pi = 21$, a converging-diverging channel: streamwise non-periodic.

Figure 3.1: Subdomain spacing in a converging-diverging channel.

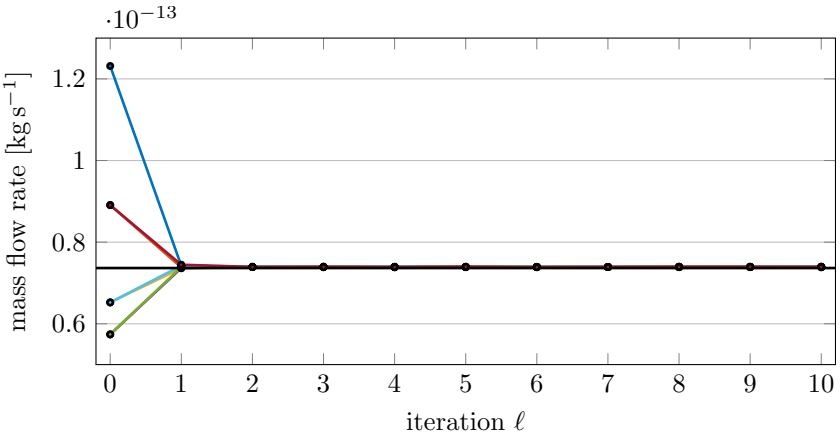

Figure 3.2: **Case 1** – convergence of mass flow rates measured in $\Pi = 7$ subdomains ($\langle \dot{m}_i \rangle$ for $i = 1, 2, \ldots, \Pi$) towards a single value. The steady-state mass flow rate computed by the dsmcFoam solver is shown for comparison (——). Because uncertainty becomes negligibly small for $\ell > 1$, error bars have been omitted.

To assess the accuracy of the steady-IMM, a conventional (non-hybrid) DSMC simulation (using the dsmcFoam solver of Scanlon et al. [2010]) is performed using $N_f \approx 58\,000$ representative particles, chosen such that each cell of the mesh initially contains $\xi = 30$ particles, with each cell having dimensions that are approximately one fifth of the equilibrium mean free path. The time step is a small fraction of the mean collision time. The applied acceleration is $a = 10^{10}\,\mathrm{m\,s^{-2}}$ – a large value that is used to obtain a manageable signal-to-noise ratio, as the simulation of low-signal flows by the DSMC method is prohibitively intensive; a large number of statistically independent samples would be required to accurately estimate flow responses.

The flow is characterised by a maximum Reynolds number $\mathrm{Re} = 11.21 \times 10^{-3}$ (based on local surface separation L_y and centreline velocity), and a maximum Mach number $\mathrm{Ma} = 45.47 \times 10^{-3}$. The Knudsen number (at the centreline) ranges from 4.21 to 6.83. The mass flow rate obtained by the non-hybrid DSMC simulation is $\mathcal{M} = 73.658 \pm 0.012 \times 10^{-15}\,\mathrm{kg\,s^{-1}}$ (one standard-deviation error, throughout).

Since our focus is on low-signal flows, which the DSMC method is not suited to treat, the LVDSMC method is selected as the micro solver. To demonstrate the stability, accuracy, and efficiency of the steady-IMM, the number of subdomains Π (providing flow rate data) is varied ($\Pi = 5$, 7, 9, 11, and 21). As the problem is periodic (in the streamwise direction), subdomains are placed according to equation (2.18). The multiscale configuration for $\Pi = 21$ is illustrated in Fig. 3.1b (considered to provide a highly accurate solution). For $\Pi = 7$ and $\ell = 2$ (iteration index), $\overline{\dot{m}} = 73.920 \pm 0.017 \times 10^{-15}\,\mathrm{kg\,s^{-1}}$, which is within 0.36 % of $\mathcal{M}$ (see Fig. 3.2).

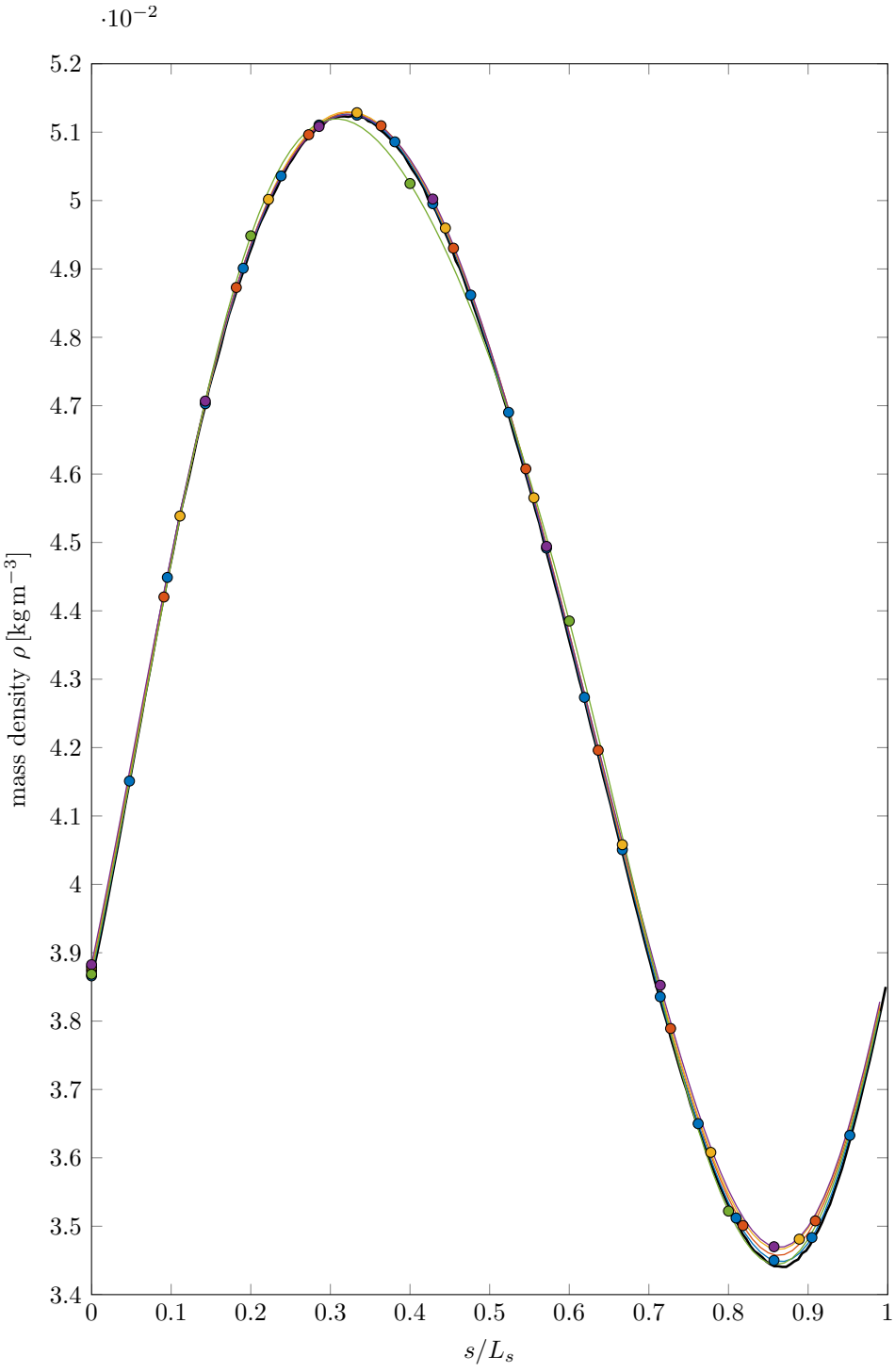

Figure 3.3: **Case 1** – streamwise variation of density computed by the steady-IMM for $\Pi = 5$ (—●—), $\Pi = 7$ (—●—), $\Pi = 9$ (—●—), $\Pi = 11$ (—●—), $\Pi = 21$ (—●—). The variation computed by the dsmcFoam solver is shown for comparison (——).

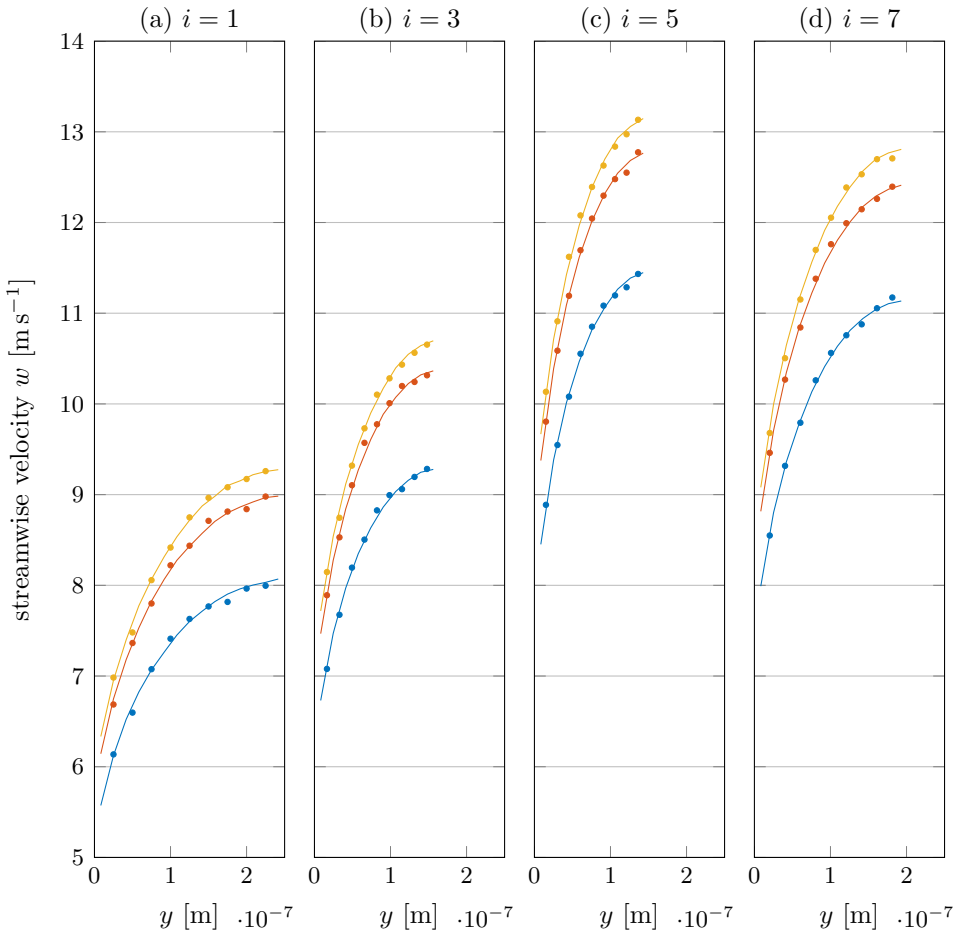

Figure 3.4: **Case 1** – profiles of fluid velocity at various streamwise locations (a)-(d) and at three transverse slices located at, $x = x_1, x_2, x_3$. Data markers represent velocities computed by the dsmcFoam solver, which used the method of bins to sample the data presented. Solid lines represent velocity profiles obtained by the steady-IMM. For $\Pi = 7$ subdomains, $x_1 = 0.0750\,\mu$m (——); $x_2 = 0.158\,\mu$m (——); $x_3 = 0.242\,\mu$m (——); (a) $i = 1$ ($s/L_s = 0$) (for which the two-dimensional velocity profile $w(x, y)$ is shown in Fig. 3.5a); (b) $i = 3$ ($s/L_s = 0.286$); (c) $i = 5$ ($s/L_s = 0.571$); (d) $i = 7$ ($s/L_s = 0.857$). Walls are located at $x = 0$, $0.500\,\mu$m; (a) $y = 0$, $0.500\,\mu$m; (b) $y = 0$, $0.329\,\mu$m; (c) $y = 0$, $0.303\,\mu$m; (d) $y = 0$, $0.403\,\mu$m. Owing to symmetries in the y-direction, only half of the profile is shown. Note, interpolation may be used to recover velocity profiles in the macro domain.

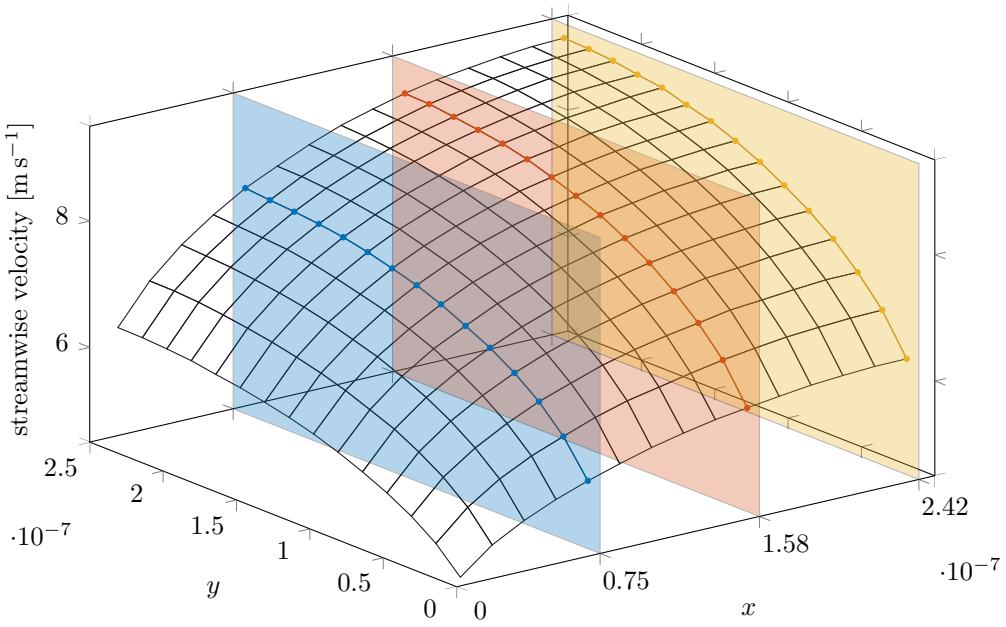

(a) **(Case 1)**: velocity profile $w(x, y)$.

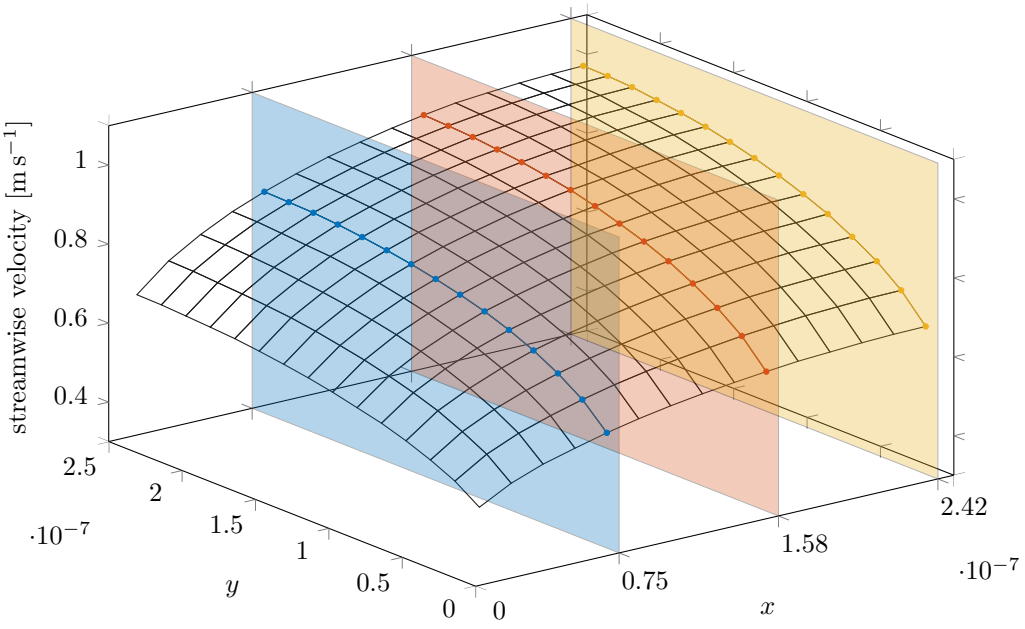

(b) **(Case 2)**: velocity profile $w(x, y)$.

Figure 3.5: Full two-dimensional velocity profiles $w(x, y)$ extracted from the first of (a) $\Pi = 7$ and (b) $\Pi = 11$ subdomains. Walls are located at $x = 0$, 0.5 µm; $y = 0$, 0.5 µm. Owing to symmetries in the xy-plane, only a quarter of the subdomain is simulated. Nodes of the mesh represent the cell centres of the computational mesh.

The results obtained from the steady-IMM and the non-hybrid dsmcFoam simulation are compared in Figs. 3.3 and 3.4. Figure 3.3 shows the streamwise variation of density (at the centreline) through the channel for $\Pi = 5$, 7, 9, 11, 21. For $\Pi = 7$, Fig. 3.4 compares velocity profiles at four different streamwise positions (corresponding to the placement of subdomains $i = 1$, 3, 5, 7). At each streamwise position, velocities are sampled along cell centres (see Fig. 3.5a). Agreement is excellent between the steady-IMM and the non-hybrid dsmcFoam simulation. It is perhaps counter-intuitive to see that the density is not constant despite the low Mach number (the occurrence of this fluid-compressibility effect is discussed in Gad-el Hak [2005]). Furthermore, the position of maximum density does not occur at the throat of the channel $\big(s/L_s = 0.5\big)$, but instead slightly upstream.

It would be preferable, for consistency, to assess the performance of the steady-IMM relative to a three-dimensional (non-hybrid) LVDSMC simulation. However, because a three-dimensional implementation of the LVDSMC methodology does not exist, it is not possible to precisely determine the considerable performance improvement afforded by the steady-IMM, relative to a full molecular treatment of the problem. An approximate, yet consistent, measure can be calculated by comparison of the product (G) of the number of simulated deviational (or representative) particles (dependent on the spatial discretisation and the desired number of particles per cell) and the number of simulated time steps. For the full microscopic problem,

$$G_f = N_f\big(\mathcal{T} + N_{\texttt{sam.}}\big)\,, \tag{3.1}$$

where N_f is the number of particles occupying the full domain, $\mathcal{T}$ is the number of time steps required for the flow to reach steady-state conditions, and $N_{\texttt{sam.}} = N_{\texttt{sam.,LV}}$ is the number of statistically independent samples (not time steps) required by the LVDSMC method to estimate the statistical mean value of the streamwise velocity w with a desired fractional error (the value of $N_{\texttt{sam.}}$ is predicted from the estimates of Hadjiconstantinou et al. [2003]). Note, calculation of the correlation time, beyond which subsequent samples are essentially independent, is unnecessary for the purposes of this comparison. For the multiscale representation of the problem,

$$G_m = \mathcal{N}_m\big(\mathcal{T} + N_{\texttt{sam.}}\big)\big(\ell + 1\big)\,, \tag{3.2}$$

where $\mathcal{N}_m$ is the product of Π and the number of deviational particles in a representative subdomain, and $\ell + 1$ is the number of times that Π micro-solver instances are generated; before iterating (at $\ell \geq 1$), a set of Π micro-solver instances are required (at $\ell = 0$) for the estimation of the constant of proportionality k in equation (2.11). The convergence criterion (effectively dictating ℓ) is given by

$$\left| \frac{\sigma}{\overline{\dot{m}}^{\,\ell=1}_{1,\ldots,\Pi}} \right| < \zeta_{\texttt{tol.}}\,, \tag{3.3}$$

where σ is the standard deviation of $\left\langle \dot{m}^{\ell}_{1,\ldots,\Pi} \right\rangle$, $\overline{\dot{m}}^{\,\ell=1}_{1,\ldots,\Pi}$ is the mean of the mass flow rates measured during the first iteration, and $\zeta_{\texttt{tol.}} = 0.001$ is a predetermined tolerance. The ratio of G_f (equation (3.1)) and G_m (equation (3.2)),

$$C = \frac{G_f}{G_m} = \frac{N_f}{\mathcal{N}_m\,(\ell+1)}\,, \tag{3.4}$$

provides an improvement factor. By setting the same time-step size for both full and multiscale problems, $\left(\mathcal{T} + N_{\texttt{sam.}}\right)$ does not need to feature in equation (3.4). After some simplification, the theoretical performance improvement of the steady-IMM relative to a three-dimensional LVDSMC simulation is given by

$$C = \frac{N_s}{\Pi\,(\ell+1)}\,, \tag{3.5}$$

where N_s is the number of cells in the streamwise direction. This assumes that the number of computational cells in each subdomain is equal to the number in the xy-plane of the non-hybrid simulation. The number of deviational particles per cell Ξ must also be consistent. The performance of the steady-IMM is clearly dependent on its rate of convergence, which is dictated by the proportionality constant k and the convergence characteristics of the pseudospectral methods described in Chapter 2. For Case 1, where $N_s = 121$, $\Pi = 7$, and $\ell + 1 = 3$ (Fig. 3.2 shows convergence at $\ell = 2$), the performance improvement of the steady-IMM, relative to a three-dimensional LVDSMC simulation, is $C = 5.8$: this conservative estimate is very encouraging. With minimal computational cost, three-dimensional low-signal flows can be accurately resolved by the steady-IMM.

We now estimate the performance improvement of the steady-IMM relative to the non-hybrid (three-dimensional) DSMC simulation described previously. In the low-signal limit, the statistical uncertainty in macroscopic properties has been characterised by Hadjiconstantinou et al. [2003]. As presented in Chapter 1, the relative statistical error ϵ_w in cell-based streamwise velocity estimates, obtained by non-deviational methods (such as the DSMC method), is given by

$$\epsilon_w = \frac{\sigma_w}{U} = \frac{1}{\sqrt{N_{\texttt{sam.,DS}}\,N_{\texttt{cell}}}}\,\frac{1}{\mathrm{Ma}\sqrt{\kappa}}\,, \tag{3.6}$$

where σ_w is the standard deviation of the streamwise velocity w, U is the character-

istic velocity, $N_{\texttt{sam.}}$ is the number of statistically independent samples required to estimate w, $N_{\texttt{cell}}$ is the number of computational particles per cell, and κ is the adiabatic index. For the DSMC method, equation (3.6) shows that ϵ_w is proportional to $(N_{\texttt{sam.}} N_{\texttt{cell}})^{-1/2}$ and Ma^{-1}. Thus as $\mathrm{Ma} \to 0$, the statistical error in cell-based measures becomes large. Conversely, for near-equilibrium flows, the LVDSMC method is able to estimate macroscopic properties with small relative statistical error that is independent of the departure from equilibrium [Hadjiconstantinou et al., 2010; Radtke, 2011; Radtke et al., 2013]. Therefore, we neglect the departure from equilibrium in equation (3.6), and estimate the value of $N_{\texttt{sam.,LV}}$ for use in equation (3.2). The improvement factor (for the same relative statistical error) is then

$$C = \frac{G_f}{G_m} = \frac{N_{\texttt{sam.,DS}}}{N_{\texttt{sam.,LV}}} \frac{\xi}{\Xi} \frac{N_s}{\Pi\,(\ell + 1)}\,, \tag{3.7}$$

where Ξ is the number of deviational particles per cell. Again, the time-step size is equal for both full and hybrid cases. For the case being considered, where $\xi = 30$ and $\Xi \approx 10$ (recommended quantity for efficient simulation in multiple spatial dimensions [Radtke, 2011]), the performance improvement of the steady-IMM relative to the non-hybrid DSMC simulation is $C = 450$: an extremely impressive computational speed-up. Since the steady-IMM allows for the representation of the full three-dimensional domain as a small number of micro subdomains, fewer particles (relative to the full microscopic problem) are simulated. It is this feature of the steady-IMM which considerably reduces the computational intensity of the method.

3.1.2 Converging-diverging channel: pressure driven

Case 2 also consists of a converging-diverging channel flow, but, unlike in §3.1.1, the problem is constrained by Dirichlet boundary conditions on pressure. This non-periodic configuration is illustrated in Fig. 3.1c. All physical parameters relating to the geometry, including the minimum value of the scale separation number, are identical to those of the first case. The pressure boundary conditions described in Chapter 2 are used to generate the desired pressure gradient. The inlet pressure is $p_1 = 2.439 \times 10^3\,\mathrm{Pa}$ ($\mathrm{Kn} = 4$), and the outlet pressure is $p_\Pi = 1.220 \times 10^3\,\mathrm{Pa}$ ($\mathrm{Kn} = 8$). The gas is VHS argon and the temperature is $T = 273\,\mathrm{K}$.

To assess the accuracy of the steady-IMM, a non-hybrid DSMC (dsmcFoam) simulation is performed using $N_f \approx 58\,000$ representative particles, chosen such that each cell of the mesh initially contains approximately $\xi = 30$ particles. As in Case 1, the dimensions of each cell are approximately one fifth of the equilibrium mean free path. The time step is selected as a small fraction of the mean collision time.

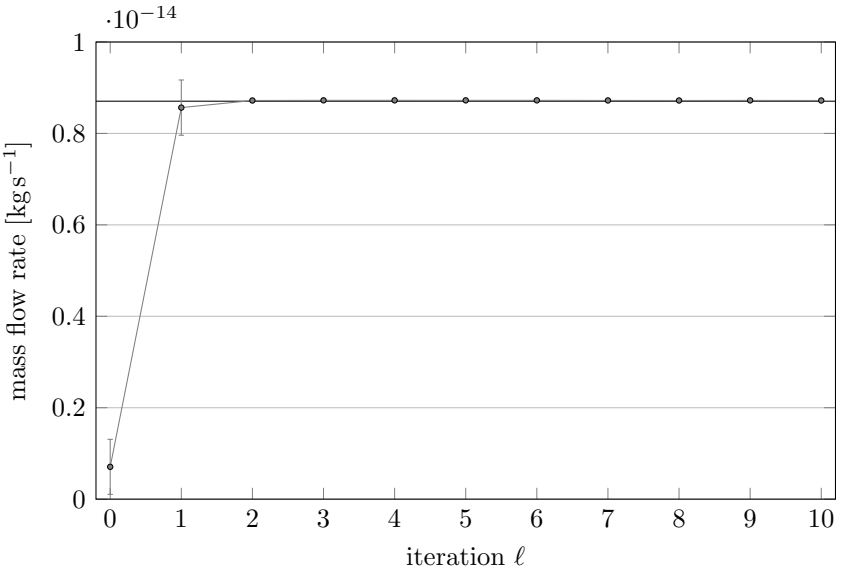

Figure 3.6: **Case 2** – convergence of mass flow rates measured in $\Pi = 11$ subdomains ($\langle \dot{m}_i \rangle$ for $i = 1, 2, \ldots, \Pi$) towards a single value. The steady-state mass flow rate computed by the dsmcFoam solver is shown for comparison (——). For $\ell > 1$, error bars are not visible because uncertainty becomes negligibly small.

The flow is characterised by a maximum Reynolds number $\mathrm{Re} = 1.373 \times 10^{-3}$ (based on local surface separation L_y and centreline velocity), and a maximum Mach number $\mathrm{Ma} = 7.805 \times 10^{-3}$, a much smaller value than that of the previous case. The Knudsen number ranges from 4.00 to 9.85. As a consequence of the reduced Mach number, the DSMC method is not used to capture transverse velocity profiles. To do so, for a reasonable value of ϵ_w, requires a prohibitively large number of samples (according to equation (3.6)). The mass flow rate obtained by the non-hybrid DSMC simulation is $\mathcal{M} = 8.705 \pm 0.008 \times 10^{-15}\,\mathrm{kg\,s^{-1}}$ (see Fig. 3.6).

Again, microscale resolution is provided by the LVDSMC method. Because this is not a periodic problem, subdomains are placed at Chebyshev points on the interval $[0, L_s]$, as defined by equation (2.25). This minimises the effects of Runge's phenomenon (undesirable oscillation at the limits of the interval). For $\Pi = 11$ and $\ell = 2$, the steady-IMM predicts $\overline{\dot{m}} = 8.720 \pm 0.002 \times 10^{-15}\,\mathrm{kg\,s^{-1}}$, which is within 0.18 % of the value obtained by the non-hybrid dsmcFoam simulation.

For $\Pi = 11$, Fig. 3.7 shows velocity profiles at four different streamwise positions (corresponding to the placement of subdomains $i = 1$, 3, 5, 7). At each streamwise position, velocity profiles are extracted along grid lines that extend in the y-direction (see Fig. 3.5b). Figures 3.8 and 3.9 present the streamwise variation (at the centreline) of density and pressure, and the streamwise velocity w, respectively.

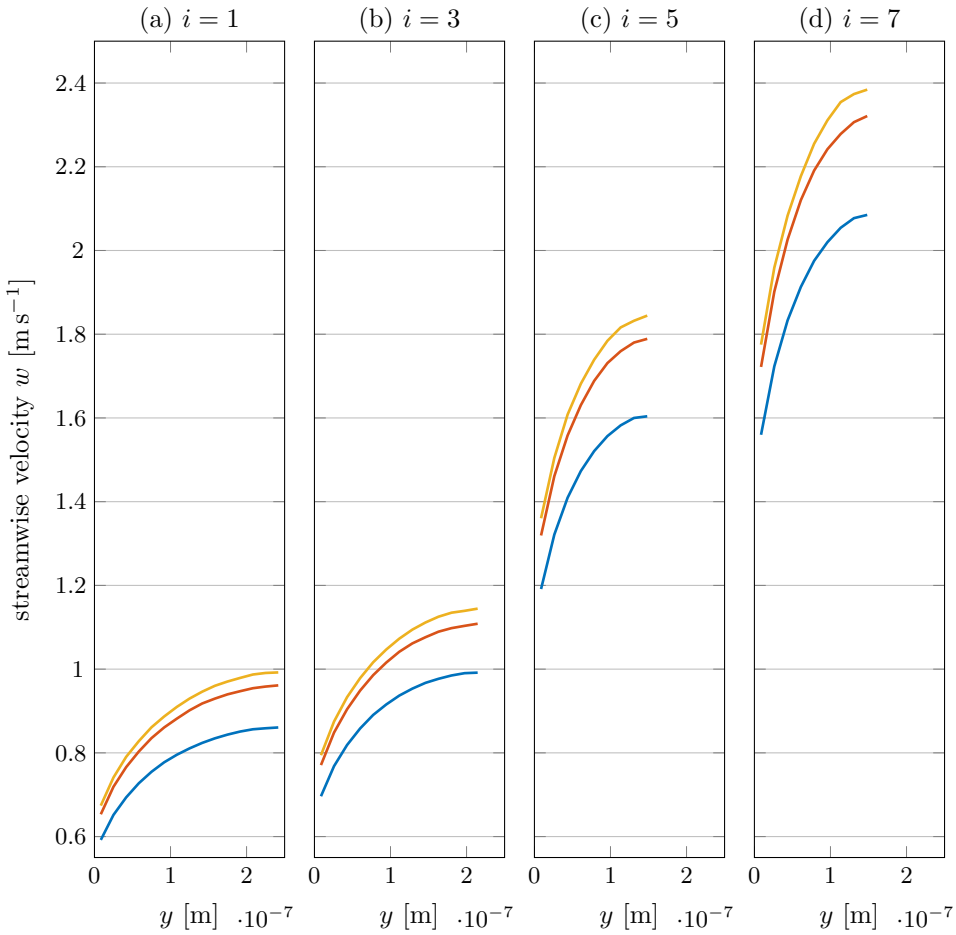

Figure 3.7: **Case 2** – profiles of fluid velocity at various streamwise locations (a)-(d) and at three transverse slices: $x = x_1, x_2, x_3$. All profiles $w(y)$ are obtained by the steady-IMM, where $x_1 = 0.0750\,\mu\text{m}$ (——); $x_2 = 0.158\,\mu\text{m}$ (——); $x_3 = 0.242\,\mu\text{m}$ (——); (a) $i = 1$ ($s/L_s = 0$) (for which the two-dimensional velocity profile $w(x, y)$ is shown in Fig. 3.5b); (b) $i = 3$ ($s/L_s = 0.0955$); (c) $i = 5$ ($s/L_s = 0.345$); (d) $i = 7$ ($s/L_s = 0.655$). Walls are located at $x = 0$, $0.500\,\mu\text{m}$; (a) $y = 0$, $0.500\,\mu\text{m}$; (b) $y = 0$, $0.446\,\mu\text{m}$; (c) $y = 0$, $0.314\,\mu\text{m}$; (d) $y = 0$, $0.314\,\mu\text{m}$. Owing to symmetries in the y-direction, only half of the profile is shown. Without excessive computational effort, profiles from the non-hybrid DSMC simulation cannot be resolved with an acceptable level of statistical confidence, and are therefore not included.

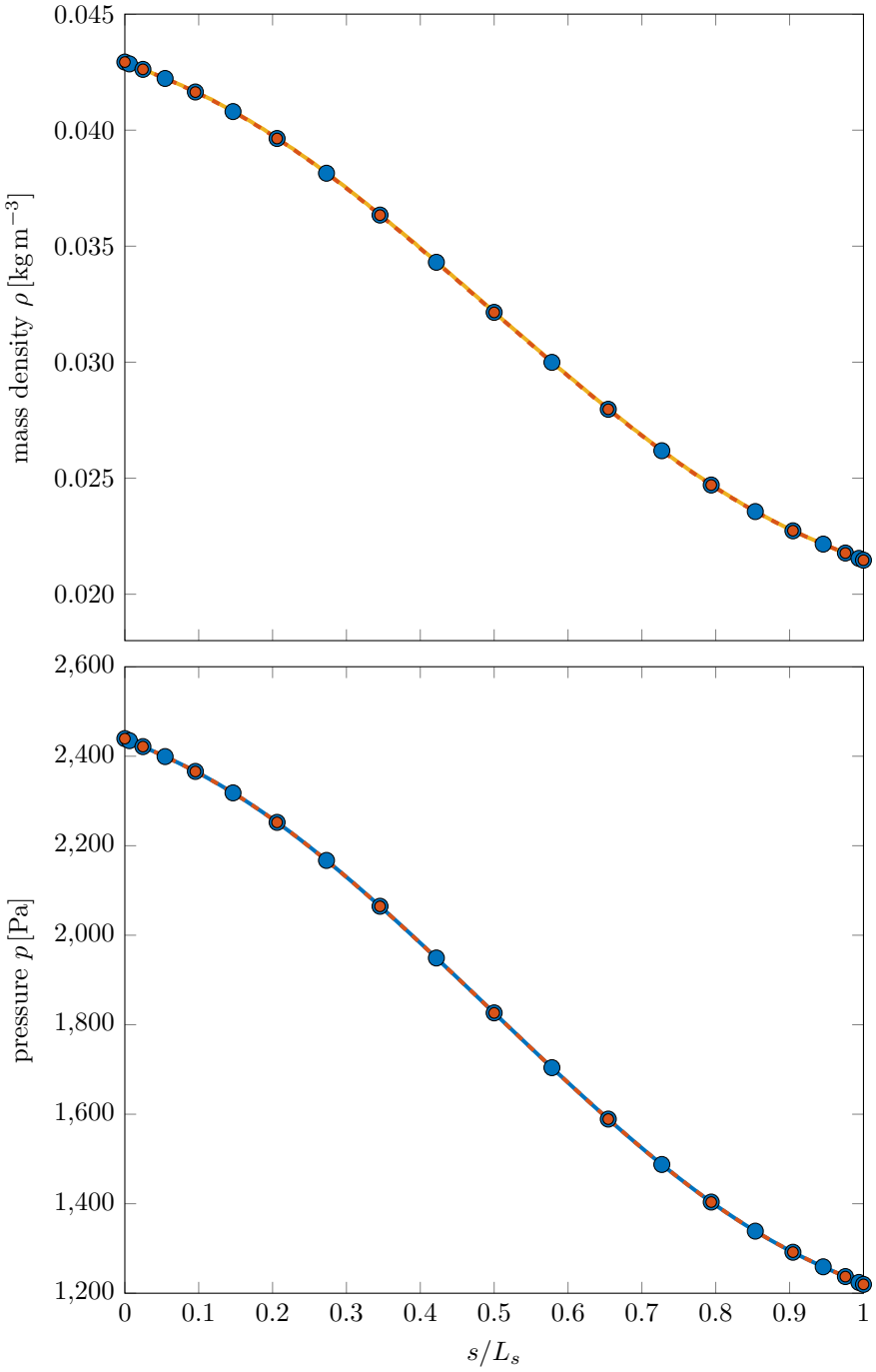

Figure 3.8: **Case 2** – streamwise variation of ρ (top) and p (bottom) computed by the steady-IMM for $\Pi = 11$ (● with dashed line) and $\Pi = 21$ (● with solid line). The continuous variation of ρ computed by the DSMC method (——) is also shown. For clarity, the continuous variation of ρ is only shown for $\Pi = 11$, which is considered to be less accurate. The continuous variation of p is shown for both values of Π.

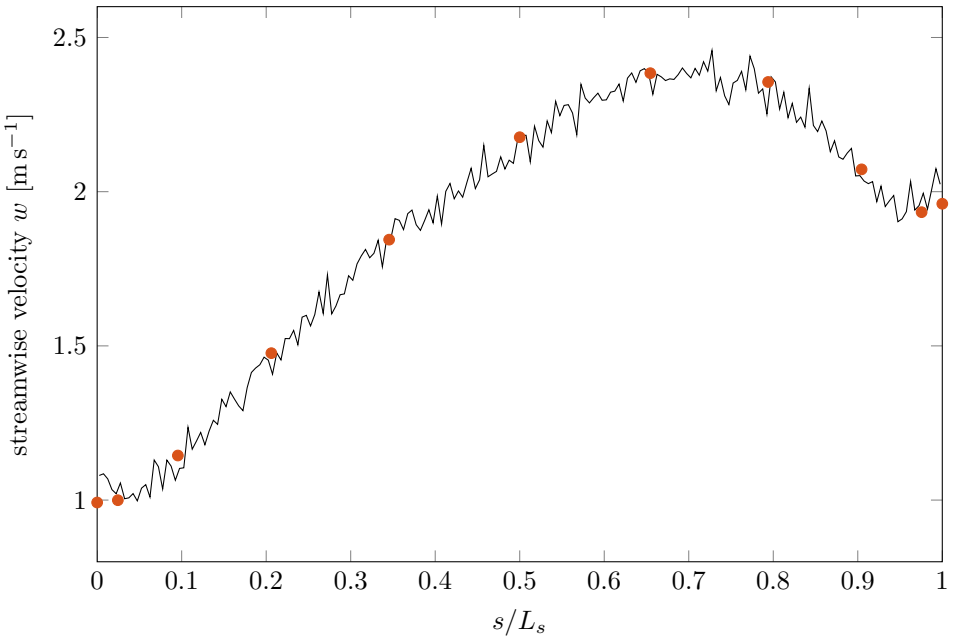

Figure 3.9: **Case 2** – streamwise variation of velocity w at the centreline. Point values of w at the geometric centres of $\Pi = 11$ LVDSMC micro subdomains (●) are compared to the continuous variation of w obtained by the DSMC method (——).

The results show an acceleration and expansion towards $s/L_s = 1$, and an increasing level of slip as the Knudsen number increases with decreasing density. Excellent agreement is observed between the steady-IMM and the non-hybrid DSMC calculation. The improvement factor relative to the non-hybrid DSMC simulation is $C = 290$: an impressive speed-up despite a larger value of Π (relative to Case 1).

3.1.3 Eccentric-cylinder shear-driven flow

As micro-machinery fabrication matures, accurately modelling the lubrication layer in micro-gas journal bearings will become increasingly important. Generally, the thickness (L_y) of such a film is extremely small relative to its dimension in the s-direction (L_s): a length-scale separated problem that can be modelled using the steady-IMM. Furthermore, if the Mach number is low, as is typical in small-scale devices, the temperature variation (due to viscous heating) across the thickness of the lubricant film can be neglected and isothermal conditions are valid.

The final isothermal verification case consists of a two-dimensional shear-driven flow confined between eccentric circular cylinders (shown in Fig. 3.10): a micro-gas journal bearing during operation. Surface motion conditions are specified by the tangential velocities $u_{B,\,0} = -5\,\mathrm{m\,s^{-1}}$ and $u_{B,\,h} = 0\,\mathrm{m\,s^{-1}}$ for the inner and

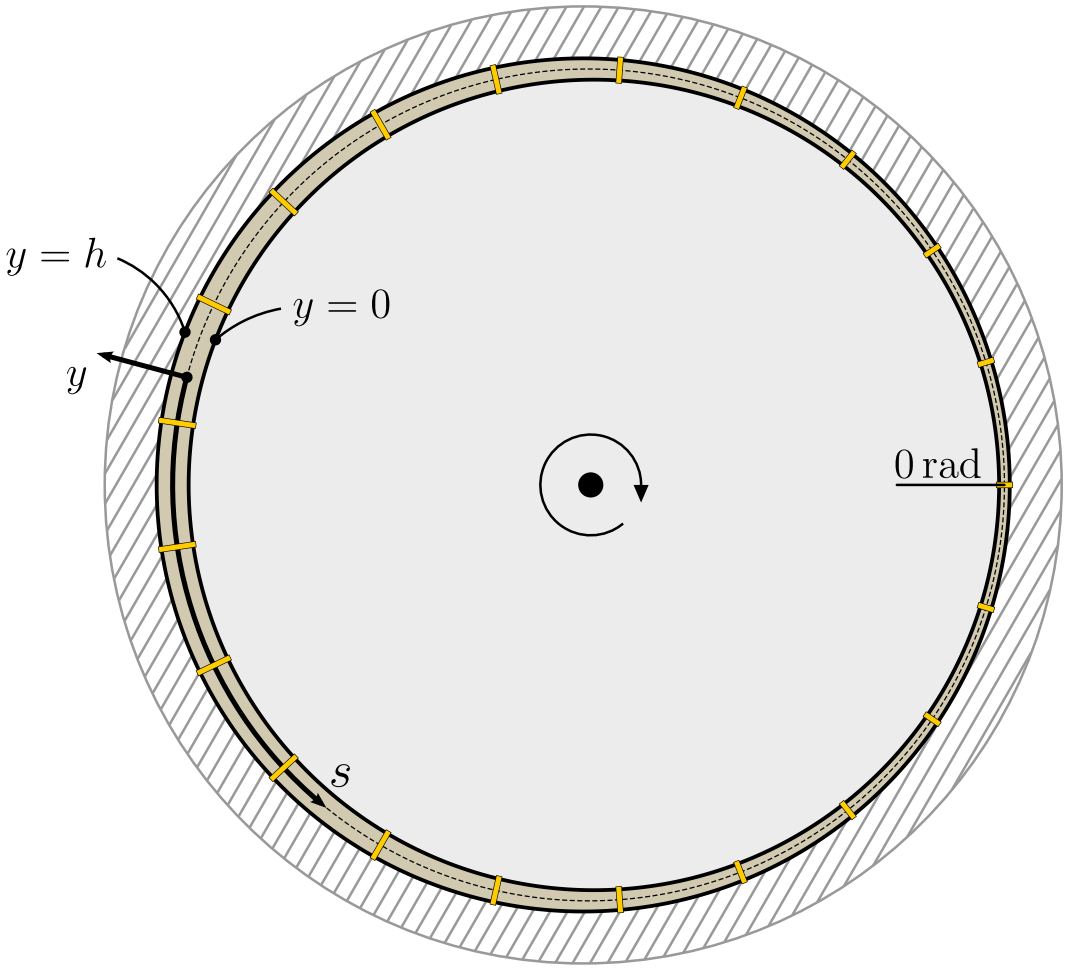

Figure 3.10: **Case 3** – two-dimensional shear-driven flow confined between eccentric circular cylinders. The x-direction is normal to the sy-plane. Subdomains are one-dimensional LVDSMC instances, and as such are displayed as $\Pi = 21$ lines.

outer cylinders, respectively (wall velocities are chosen so that a DSMC simulation is computationally feasible). The inner cylinder and outer cylinder have radii of 100 µm and 101 µm, respectively. The length of the geometry in the x-direction is $L_x = 1.5\,\mu\text{m}$. The inner cylinder rotates about its centre of mass. The maximum and minimum distance between the two cylinders are 1.5 µm and 0.5 µm, respectively. The gas confined between the cylinders is VHS argon, with average density $\bar{\rho} = 28.62 \times 10^{-3}\,\text{kg}\,\text{m}^{-3}$. The temperature of both surfaces is $T = 273\,\text{K}$. For the full molecular treatment by the DSMC method, $\mathcal{T} = 20\,000$, $N_{\texttt{sam.,DS}} \approx 757.5 \times 10^3$, and $N_f \approx 94\,800$. Therefore, $G_f = 72.78 \times 10^9$. The steady-state mass flow rate computed by the DSMC method is $\mathcal{M} = -90.420 \pm 0.329 \times 10^{-15}\,\text{kg}\,\text{m}\,\text{s}^{-1}$.

Solution of the problem by the steady-IMM is achieved by the decomposition of the domain to form $\Pi = 11$, 21 equispaced subdomains. The multiscale configuration for $\Pi = 21$ is illustrated in Fig. 3.10, which is considered to provide the most accurate solution. The circumferential positions s_i are given by equation (2.18) where $L_s = 631.5\,\mu\text{m}$. Based on the convergence criterion given in equation (3.3), the steady-IMM reaches a solution at $\ell = 4$ for $\Pi = 11$; The predicted mass flow rate is $\overline{\dot{m}} = -91.255 \pm 0.072 \times 10^{-15}\,\text{kg}\,\text{m}\,\text{s}^{-1}$. This value is within 0.92 % of the value obtained by the non-hybrid dsmcFoam simulation ($\mathcal{M}$), again demonstrating the accuracy of the steady-IMM. The performance improvement of the multiscale method relative to the non-hybrid (two-dimensional) DSMC simulation, is given by equation (3.7) as $C \approx 1500$. From equation (3.5), the performance improvement of the steady-IMM relative to a non-hybrid LVDSMC simulation is $C \approx 19$

Figure 3.11 shows velocity profiles at a number of circumferential positions, and Fig. 3.12 shows the circumferential variation of density. Close agreement is found between the steady-IMM (for $\Pi = 11$ and 21) and the non-hybrid DSMC simulation. Statistical noise clearly dominates the velocity profiles (Fig. 3.11) computed by the DSMC method, which required heavy use of high performance computing facilities. The steady-IMM produces highly resolved velocity profiles, while requiring minimal computational effort. Only a workstation of modest computational performance is required. Due to the high degree of length-scale separation and weak gradients in the streamwise direction (compared to those in the transverse plane), the development period of the non-hybrid simulation is considerable. Because streamwise gradients in mass flow rate (which promote temporal changes in density) are weak, development of the flow occurs slowly (relative to viscous-driven development in the transverse direction). Not needing to simulate this lengthy development period greatly enhances the performance of the steady-IMM, and results from coupling the micro model to a steady form of the continuity equation.

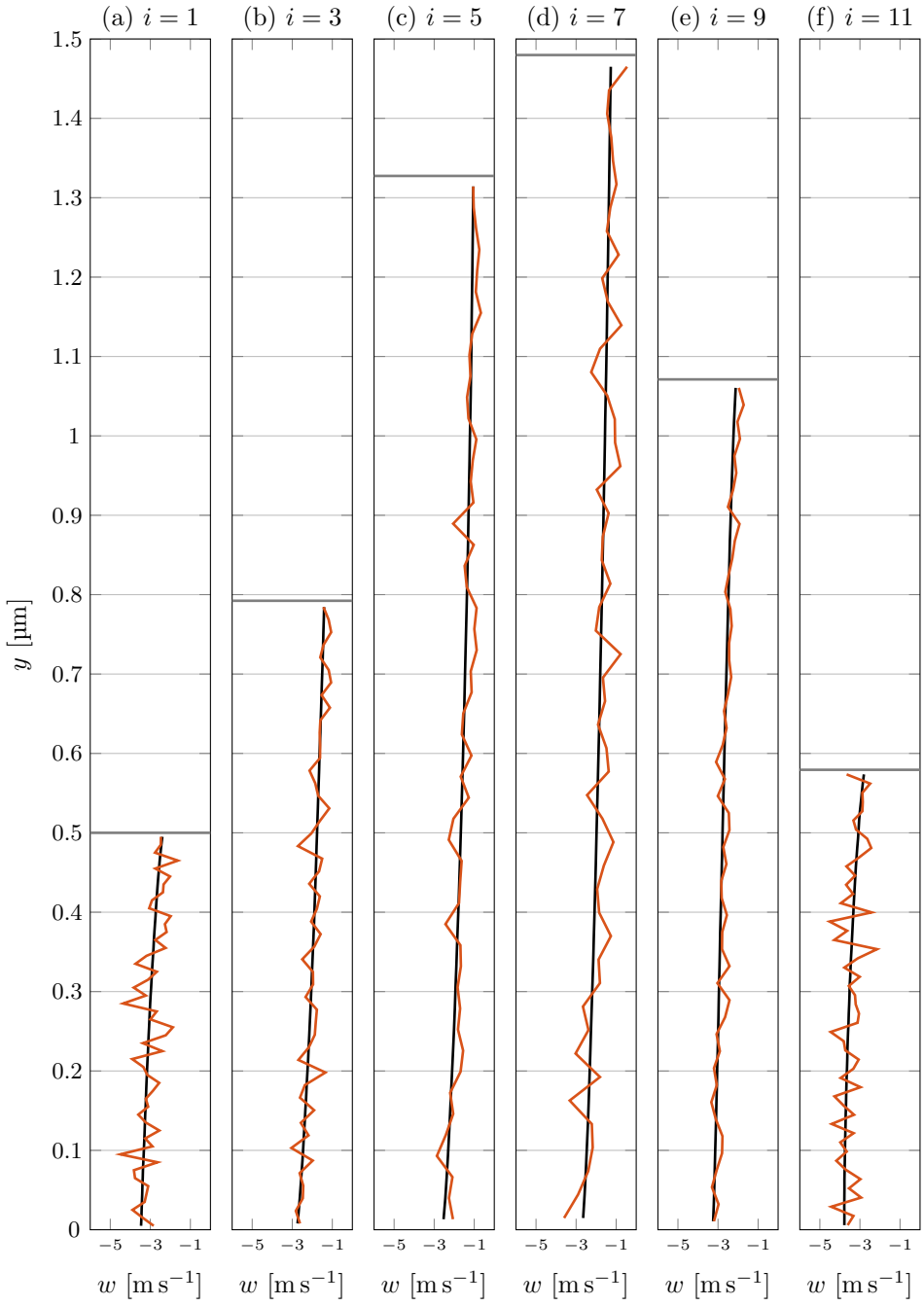

Figure 3.11: **Case 3** – comparison of velocity profiles $w(y)$ from the steady-IMM (——) and the dsmcFoam solver (——) at streamwise locations: (a) $i = 1$ ($s/L_s = 0$); (b) $i = 3$ ($s/L_s = 0.182$); (c) $i = 5$ ($s/L_s = 0.364$); (d) $i = 7$ ($s/L_s = 0.545$); (e) $i = 9$ ($s/L_s = 0.727$); (f) $i = 11$ ($s/L_s = 0.909$). Walls are located at $y = 0$ ($u_{B,0} = -5\,\mathrm{m\,s^{-1}}$) and $y = h$ ($u_{B,h} = 0\,\mathrm{m\,s^{-1}}$) indicated by (——).

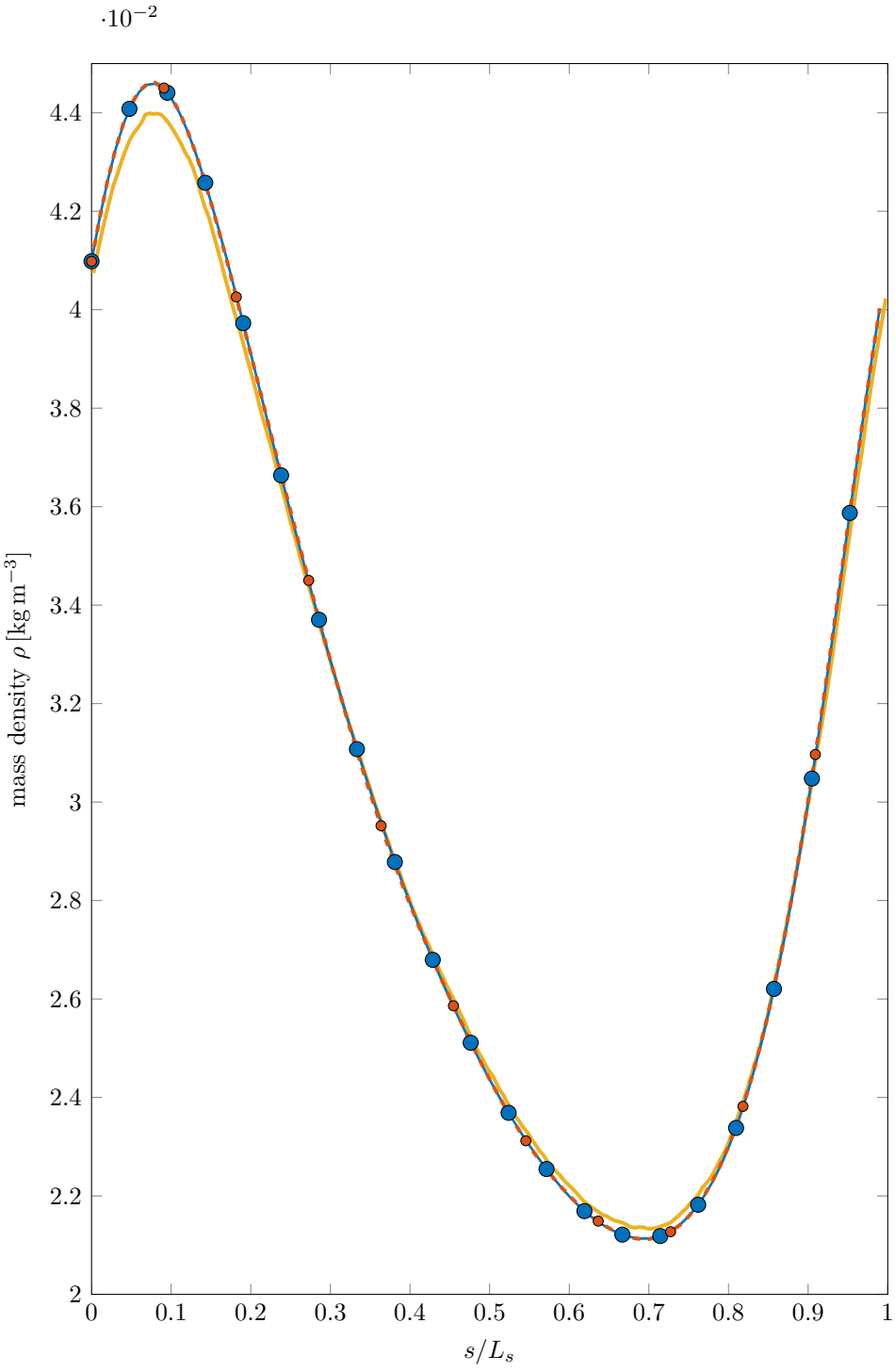

Figure 3.12: **Case 3** – comparison of streamwise variation ($s/L_s = 0$ corresponds to 0 rad on the centreline in Fig. 3.10) of ρ computed by the steady-IMM for $\Pi = 11$ (● with dashed line) and $\Pi = 21$ (● with solid line), and the dsmcFoam solver (——). Note, due to the limited functionality of (current) two-dimensional implementations of the LVDSMC method, a non-hybrid low-variance simulation is not possible.

It has been shown that the steady-IMM is able to accurately simulate shear-driven flows in a micro-gas journal bearing. To further demonstrate the methods potential, the characteristic velocity is reduced. The tangential velocity of the inner cylinder is set to $u_{B,0} = -0.1\,\mathrm{m\,s^{-1}}$, $-0.05\,\mathrm{m\,s^{-1}}$, and $-0.01\,\mathrm{m\,s^{-1}}$. Note, according to equation (3.6), to obtain a low-noise solution for $\mathrm{Ma} = 32.49 \times 10^{-6}$, which is approximately the Mach number when $u_{B,0} = 0.01\,\mathrm{m\,s^{-1}}$, a prohibitively large number of independent samples are needed: 189.4×10^9. With $\Pi = 11$, Fig. 3.13a shows the circumferential variation of density for $u_{B,0} = -0.1\,\mathrm{m\,s^{-1}}$, $-0.05\,\mathrm{m\,s^{-1}}$, and $-0.01\,\mathrm{m\,s^{-1}}$; the outer wall is stationary (i.e. $u_{B,0} = 0\,\mathrm{m\,s^{-1}}$). As an aside, when $\mathrm{Ma} \to 0$ the difference in the behaviour of gas- and liquid-lubricated bearings becomes negligible [Szeri, 1998]; this warrants further investigation. If the performance of gas lubricants is similar to that of liquid lubricants, they may be used interchangeably. Furthermore, due to the many advantages of gas lubricant films (e.g. the absence of cavitation, chemical stability, small thermal gradients and negligible viscous heating, no ecological contamination, etc.), they should be studied to assess how rarefaction and compressibility influences their behaviour.

Figures 3.13b and 3.14 reveal how modifying the Knudsen number can alter the behaviour of the lubrication layer. For a particular circumferential position, all velocity profiles pass through a common point, and the slip at both surfaces increases with Kn. Under certain conditions, the phenomenon of velocity inversion [Einzel et al., 1990], where the tangential velocity increases with distance from the rotating inner cylinder to the stationary outer cylinder, will be observed. The steady-IMM allows for the efficient study of this non-intuitive behaviour.

With support for symmetry boundary conditions, the steady-IMM can be used to study the gas layer (of μ thickness) that forms between an impacting droplet and a surface [Kolinski et al., 2012, 2014; de Ruiter et al., 2015]. Understanding drop impact behaviour is critical to a variety of processes, such as anti-icing, spray coating, and inkjet printing. The gas film (with an exceptionally high aspect ratio), remains intact if the impact speed is less than $0.5\,\mathrm{m\,s^{-1}}$ [de Ruiter et al., 2015]. The impact speed is comparable to that at which the droplet spreads on the film.

3.2 Non-isothermal problems

In this section, thermally-driven flow cases are modelled using the steady-IMM, with a focus on thermal-transpiration flows. The following cases are designed to verify that the steady-state pressure difference (and streamwise pressure variation) induced by the rarefied gas effect known as thermal-transpiration, are captured correctly.

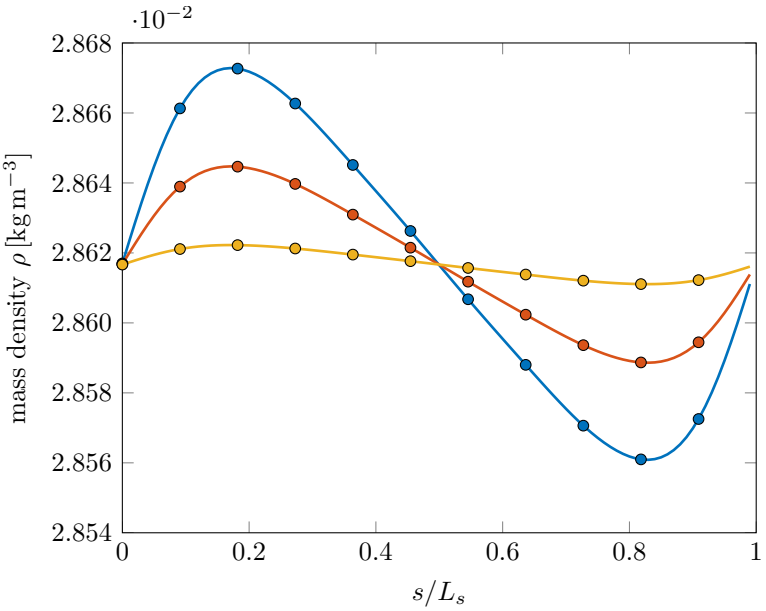

(a) Streamwise variation of mass density for three values of inner wall velocity (outer wall is stationary): $u_{B,0} = -0.1\,\mathrm{m\,s^{-1}}$ (—●—), $-0.05\,\mathrm{m\,s^{-1}}$ (—●—), $-0.01\,\mathrm{m\,s^{-1}}$ (—●—).

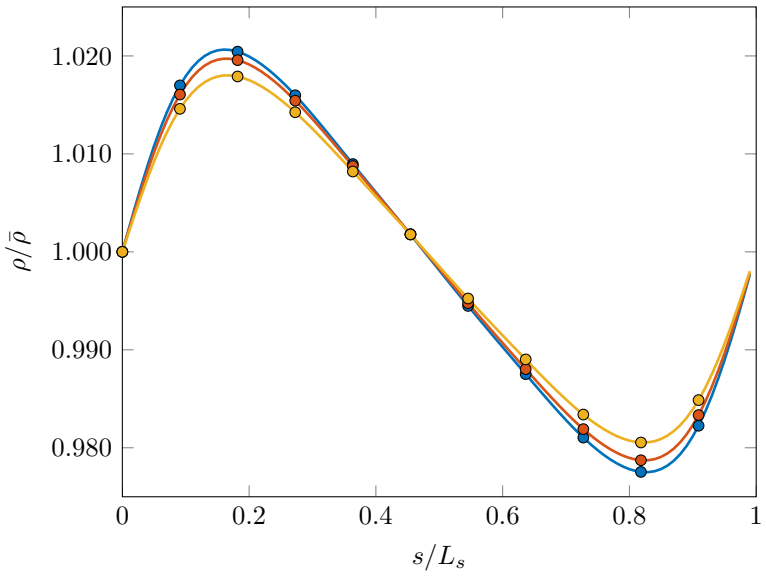

(b) Streamwise variation of mass density (normalised with respect to the average value $\bar{\rho}$) for three values of Knudsen number: Kn = 2 (—●—), Kn = 4 (—●—), Kn = 8 (—●—).

Figure 3.13: Streamwise variation ($s/L_s = 0$ corresponds to 0 rad on the centreline in Fig. 3.10) of mass density computed by the steady-IMM for $\Pi = 11$.

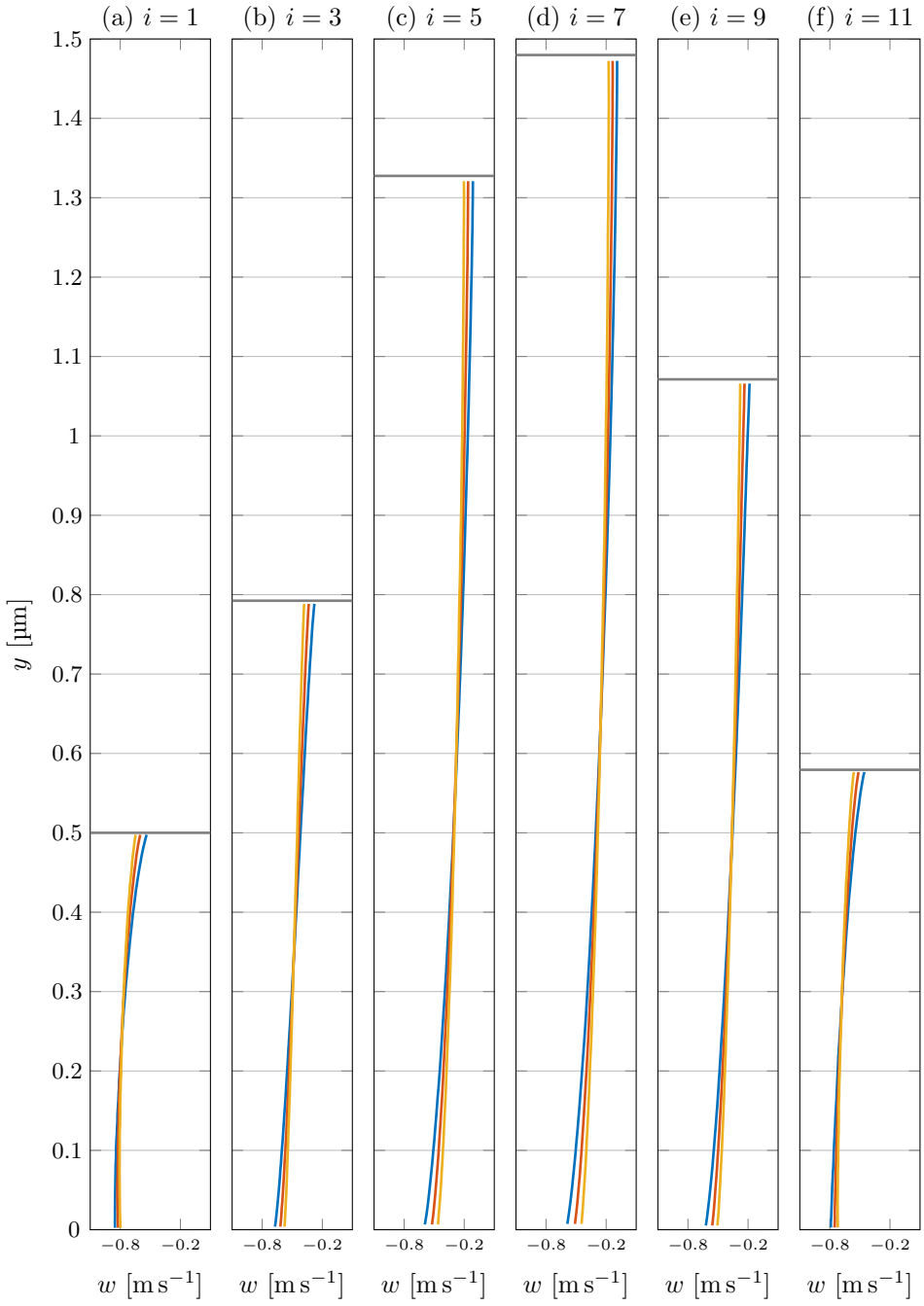

Figure 3.14: Comparison of velocity profiles $w(y)$ from the steady-IMM for ($u_{B,0} = -1\,\mathrm{m\,s^{-1}}$ and $u_{B,h} = 0\,\mathrm{m\,s^{-1}}$) Kn = 2 (——), Kn = 4 (——), and Kn = 8 (——) at streamwise locations: (a) $i = 1$ ($s/L_s = 0$); (b) $i = 3$ ($s/L_s = 0.182$); (c) $i = 5$ ($s/L_s = 0.364$); (d) $i = 7$ ($s/L_s = 0.545$); (e) $i = 9$ ($s/L_s = 0.727$); (f) $i = 11$ ($s/L_s = 0.909$). Walls are located at $y = 0$ and $y = h$ indicated by (——).

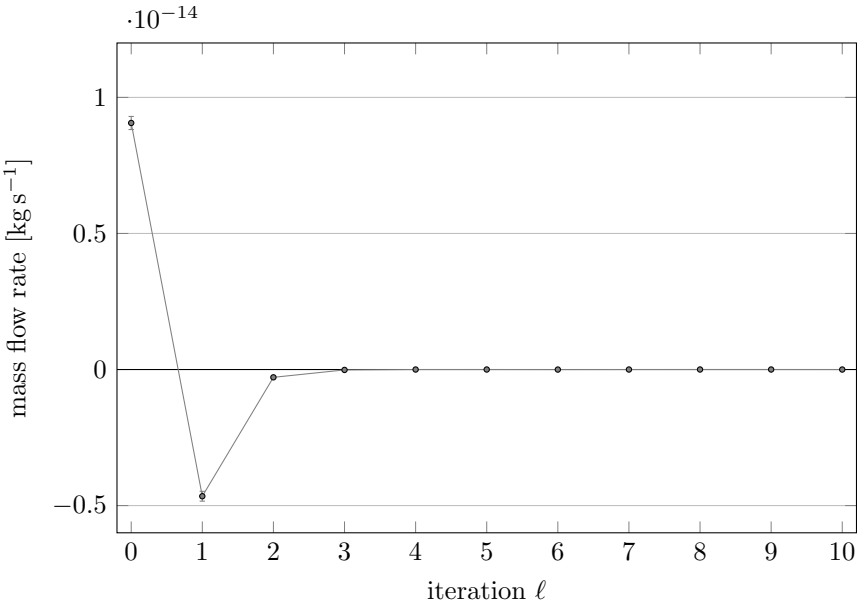

Figure 3.15: **Case 4** – convergence for $\Pi = 7$ to zero net mass flow rate. For $\ell > 1$, error bars are not visible because uncertainty becomes negligibly small.

The complexity of the problems is restricted to allow for the comparison of the solution obtained by the steady-IMM with that calculated by the method of Sharipov [1999]. This approximate method relies on the application of pre-calculated flow coefficients Q_p (reduced mass flow rate due to pressure gradient) and Q_T (reduced mass flow rate due to thermal-transpiration), which are only applicable for a limited parameter set. These flow coefficients are functions of the rarefaction parameter δ.

3.2.1 Linear temperature gradient

The non-isothermal case considered here consists of a thermal-transpiration flow driven by a linear streamwise surface temperature gradient. The length of the geometry is $L_s = 24\,\mu\text{m}$, with a square cross section of height $L_y = 0.5\,\mu\text{m}$. The streamwise temperature distribution [K] is given by $T(s) = \alpha s + 273$, where $\alpha = 4.2 \times 10^6$. The pressure at $p_1 = 2.439 \times 10^3\,\text{Pa}$ (Kn = 4). Subdomains ($\Pi = 9$, 21) are placed at Chebyshev points on the interval $[0, L_s]$, as defined by equation (2.25). For $\Pi = 21$ and $\ell = 3$, $\overline{\dot{m}} = -14.690 \pm 0.901 \times 10^{-18}\,\text{kg s}^{-1}$ (see Fig. 3.15).

Verification cannot be achieved by comparison with a non-hybrid (three-dimensional) DSMC simulation. The pressure boundary conditions of the dsmcFoam solver are unable to reliably calculate pressure in the presence of a low-signal thermal-transpiration flow dominated by thermal fluctuations. To reliably calculate the tangential and normal velocities at pressure boundary faces, the corresponding

cell-centred values of the boundary cell must be clear of overwhelming statistical error. With a satisfactory signal-to-noise ratio, the steady-state pressure difference producing zero net mass flow rate can be found by trial and error using the dsmcFoam solver – an incredibly arduous process. As discussed in §2.5, the steady-IMM has the advantage of allowing $\dot{M} = 0$ to be set in place of a boundary condition on pressure. Since the focus of attention is low-signal flows, the DSMC method is not used. For verification, the streamwise variation of pressure obtained by the steady-IMM is compared to that calculated by the model of Sharipov [1999]:

$$\frac{\mathrm{d}p}{\mathrm{d}s} = \frac{Q_T(\delta)}{Q_p(\delta)} \frac{p(s)}{T(s)} \frac{\mathrm{d}T}{\mathrm{d}s} , \tag{3.8}$$

where δ is the rarefaction parameter (inverse of the Knudsen number), and values for the coefficients Q_p and Q_T are obtained from the Shakhov model (or S-model) equation [Shakhov, 1968]. Equation (3.8) is solved using a Runge-Kutta method, with Q_p and Q_T found by interpolation on values published by Sharipov [1999].

The steady-state pressure difference (that satisfies $\dot{M} = 0$) computed by the steady-IMM is used to gauge thermal-transpiration compressor (and implicitly Knudsen compressor) performance. Figure 3.16 shows the streamwise variation of density and pressure (at the centreline) computed by the steady-IMM and the method of Sharipov. For the linear temperature gradient applied, both methods indicate that an approximately linear pressure variation is generated. The streamwise variation of pressure calculated by equation (3.8) deviates slightly from that obtained by the steady-IMM, possibly due to the approximation inherent in the S-model equation. Figure 3.17 shows the velocity profiles obtained by the steady-IMM at different streamwise locations. The inverted flow profile, resulting from the opposing effects of the pressure and temperature gradients, is observed. These results provide confidence that the steady-IMM can be applied to investigate more general thermal-transpiration flows, as is done in Chapter 5.

The same case is modified so that the surface temperature gradient is artificially large. The temperature difference is increased from $\Delta T = 100\,\mathrm{K}$ to $600\,\mathrm{K}$. The streamwise temperature distribution [K] is given by $T(s) = \alpha s + 273$, where $\alpha = 25 \times 10^6$. The pressure $p_1 = 2.439 \times 10^3\,\mathrm{Pa}$ is unchanged. Again, the streamwise variation of pressure (at the centreline) obtained by the steady-IMM is compared to that calculated by equation (3.8). It is clear from Fig. 3.18 that an approximately linear pressure variation is generated. As expected, the steady-state pressure difference is enhanced by this increased temperature difference. This reflects the effect of the varying Knudsen number on the thermal-transpiration flow.

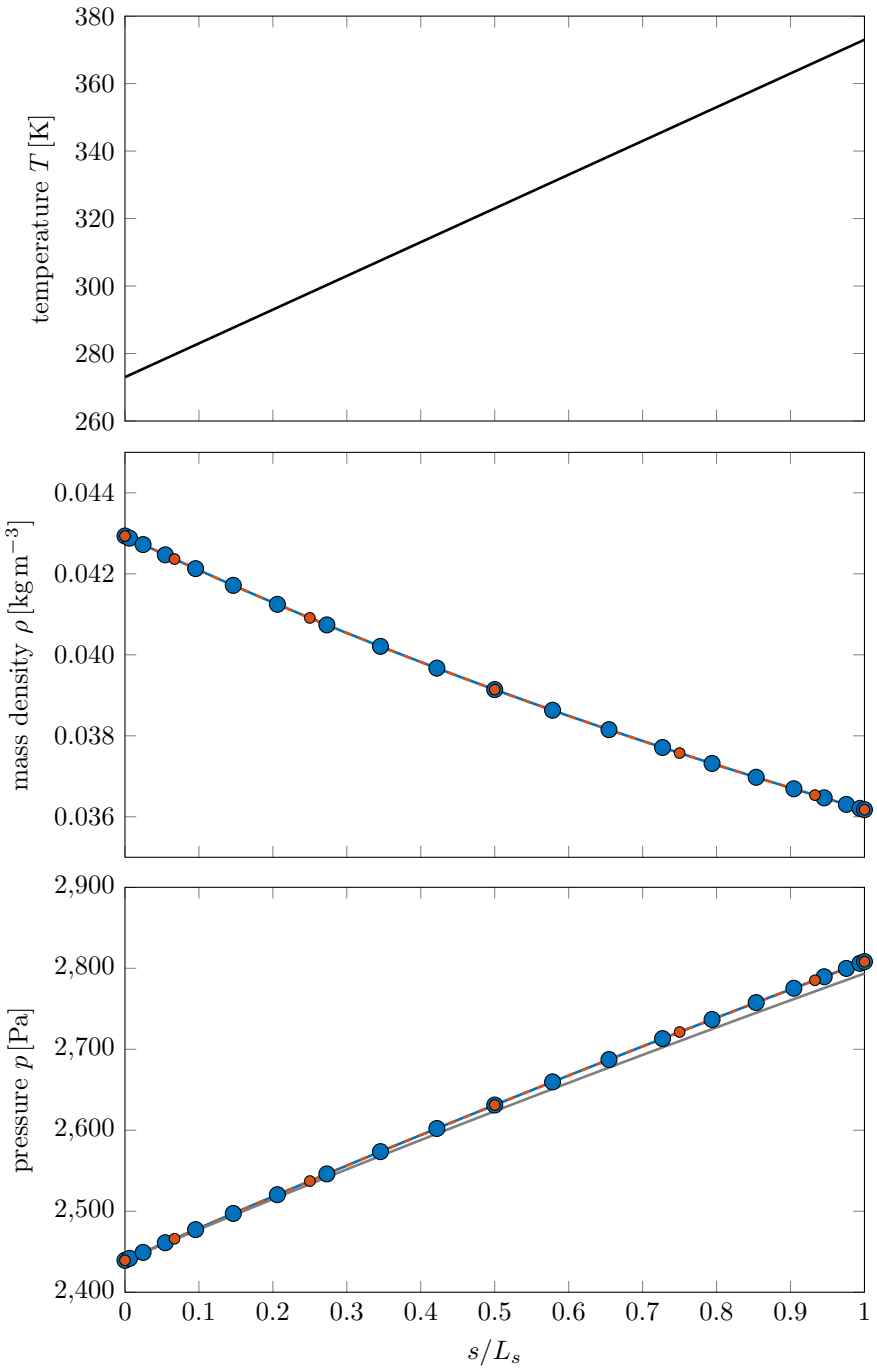

Figure 3.16: **Case 4** – streamwise variation of T (top), ρ (middle) and p (bottom) computed by the steady-IMM for $\Pi = 7$ (● with a dashed line) and $\Pi = 21$ (● with a solid line) in a simple channel with square cross section. The temperature variation is an input and is shown only for reference. The pressure variation computed by the method outlined in [Sharipov, 1999] (——) (equation (3.8)) is shown for comparison.

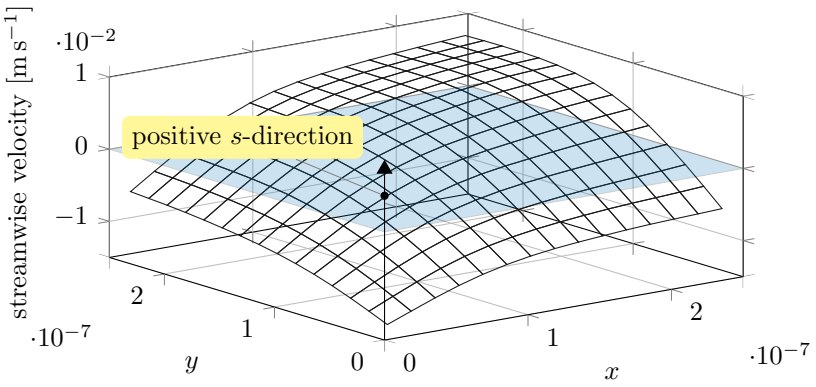

(a) $i = 1$

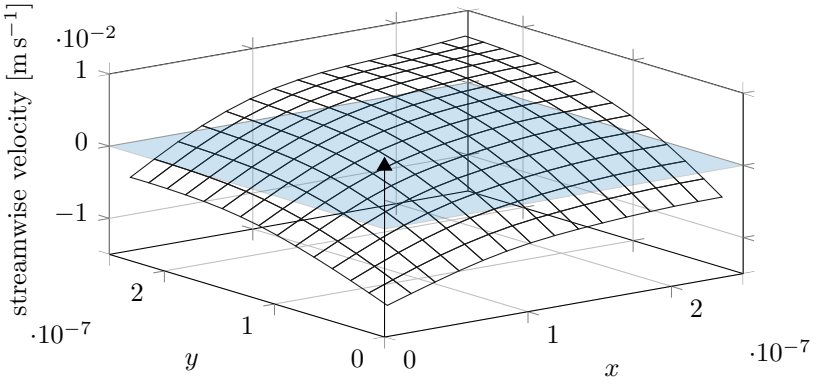

(b) $i = 4$

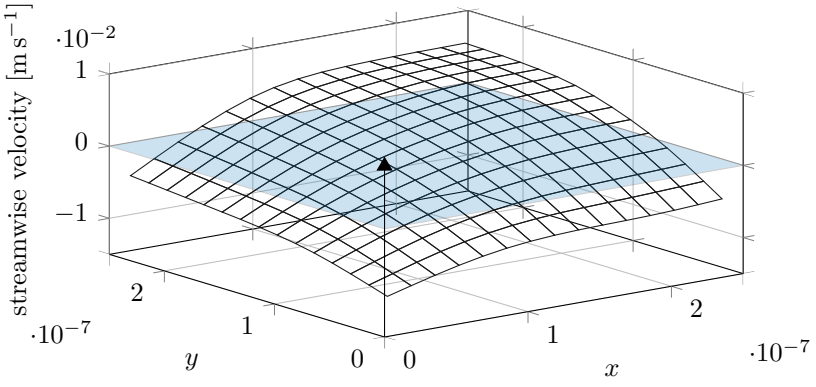

(c) $i = 7$

Figure 3.17: **Case 4** – two-dimensional velocity profiles in the transverse plane at streamwise locations: (a) $i = 1$ ($s/L_s = 0$); (b) $i = 4$ ($s/L_s = 0.5$); (c) $i = 7$ ($s/L_s = 1$). Walls are located at $x = 0, 0.5\,\mu\text{m}$; $y = 0, 0.5\,\mu\text{m}$. Owing to symmetries in the x- and y-directions, only a quarter of the subdomain is simulated.

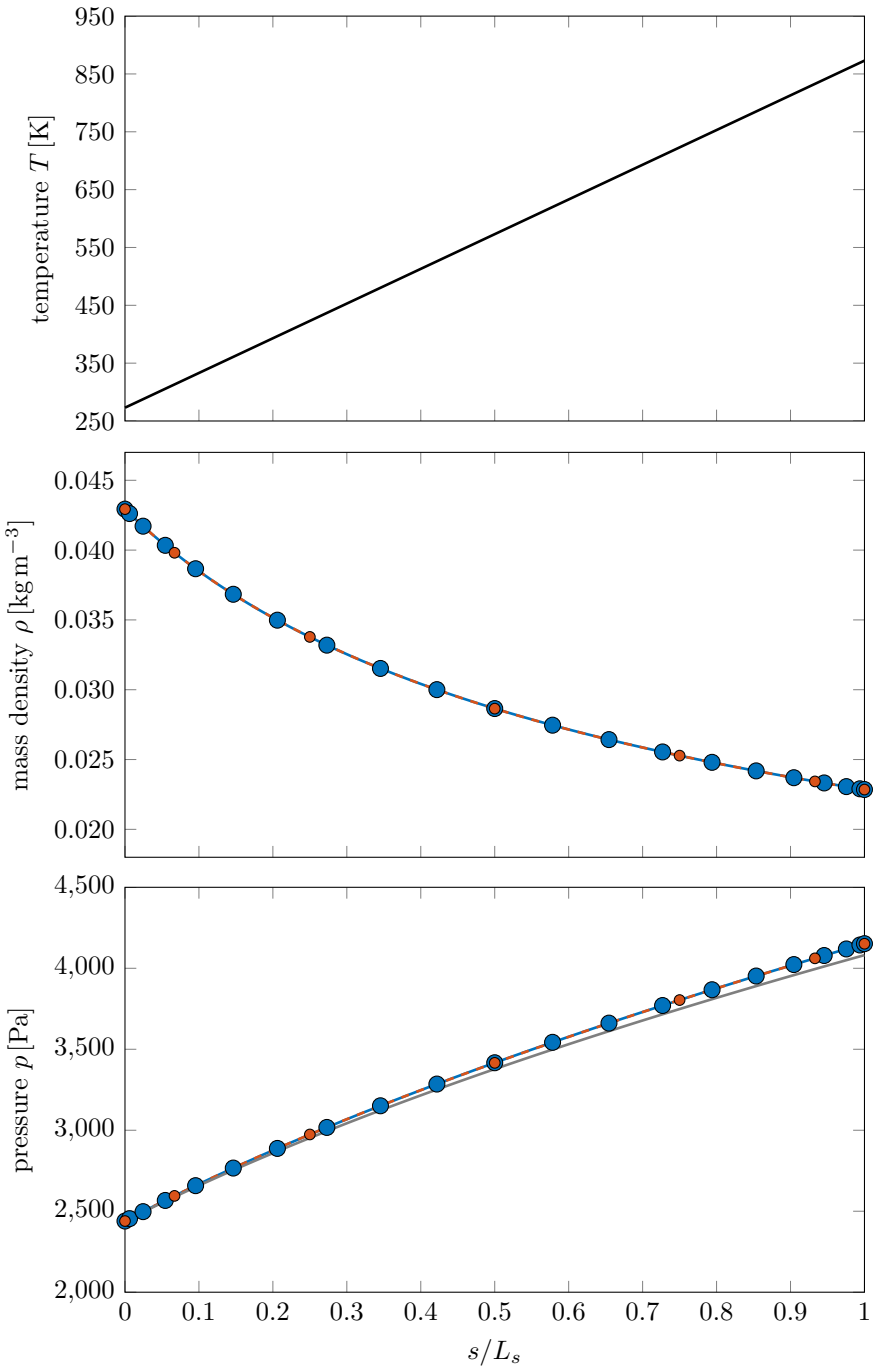

Figure 3.18: **Case 5** – streamwise variation of T (top), ρ (middle) and p (bottom) computed by the steady-IMM for $\Pi = 7$ (● with dashed line) and $\Pi = 21$ (● with solid line) in a simple channel with square cross section. The temperature variation is an input, and is set to be artificially large. The pressure variation computed by the method outlined in [Sharipov, 1999] (——) (equation (3.8)) is shown for comparison.

3.2.2 Non-linear temperature variation

In this section, the steady-IMM is applied to determine whether the steady-state pressure difference is enhanced by altering the temperature variation, whilst maintaining the same total temperature difference. All simulation conditions are identical to those of the case of the previous section, except that a non-linear temperature distribution [K], given by $T(s) = \alpha s^2 + \beta s + 273$ (where $\alpha = 160 \times 10^9$, $\beta = 330 \times 10^3$), is prescribed. Again, the steady-IMM is applied to calculate the pressure variation that satisfies $\dot{M} = 0$; Fig. 3.19 shows the computed pressure variation. The Knudsen number (at the centreline) ranges from 4 to 4.75. Clearly, the pressure difference is relatively unaffected by the temperature variation. This result demonstrates the robustness (an insensitivity under the conditions considered) of thermal-transpiration compressors: it is not necessary to precisely apply a surface temperature gradient to achieve a desired steady-state (maximal) pressure difference.

3.3 Summary

The accuracy, stability, and performance of the steady-internal-flow multiscale method (steady-IMM) have been demonstrated. It has been shown that, for both isothermal and non-isothermal conditions, the method can be used to efficiently and accurately model periodic body-force-driven flows, pressure-driven flows, shear-driven flows, and thermally-driven flows. The mass flow rate predicted by the steady-IMM is consistently within $< 1\%$ of the value computed by simulating the full microscopic problem. Furthermore, velocity measurements and the streamwise variations of density and pressure obtained by the steady-IMM are also in excellent agreement with those of conventional non-hybrid simulations. The performance improvement afforded by the method, relative to multi-dimensional non-hybrid simulations (by DSMC and LVDSMC), is considerable, with speed-ups of up to three orders of magnitude (~ 1500). The lack of a three-dimensional implementation of the LVDSMC method is inconsequential; generally, the steady-IMM (with an acceptable rate of convergence) will outperform a full molecular (non-hybrid) treatment by the micro solver (the total number of simulated particles considered during the execution of the steady-IMM is less than that required to fill the entire macro domain).

Realistic steady-state thermal-transpiration flows, which are not reliably simulated by the DSMC method, have been resolved using the steady-IMM. The steady-state pressure difference is efficiently computed by inverting the flow problem and calculating the downstream pressure with the macroscopic mass flow rate set to zero, i.e. $\dot{M} = 0$. This strategy is utilised extensively in Chapter 5.

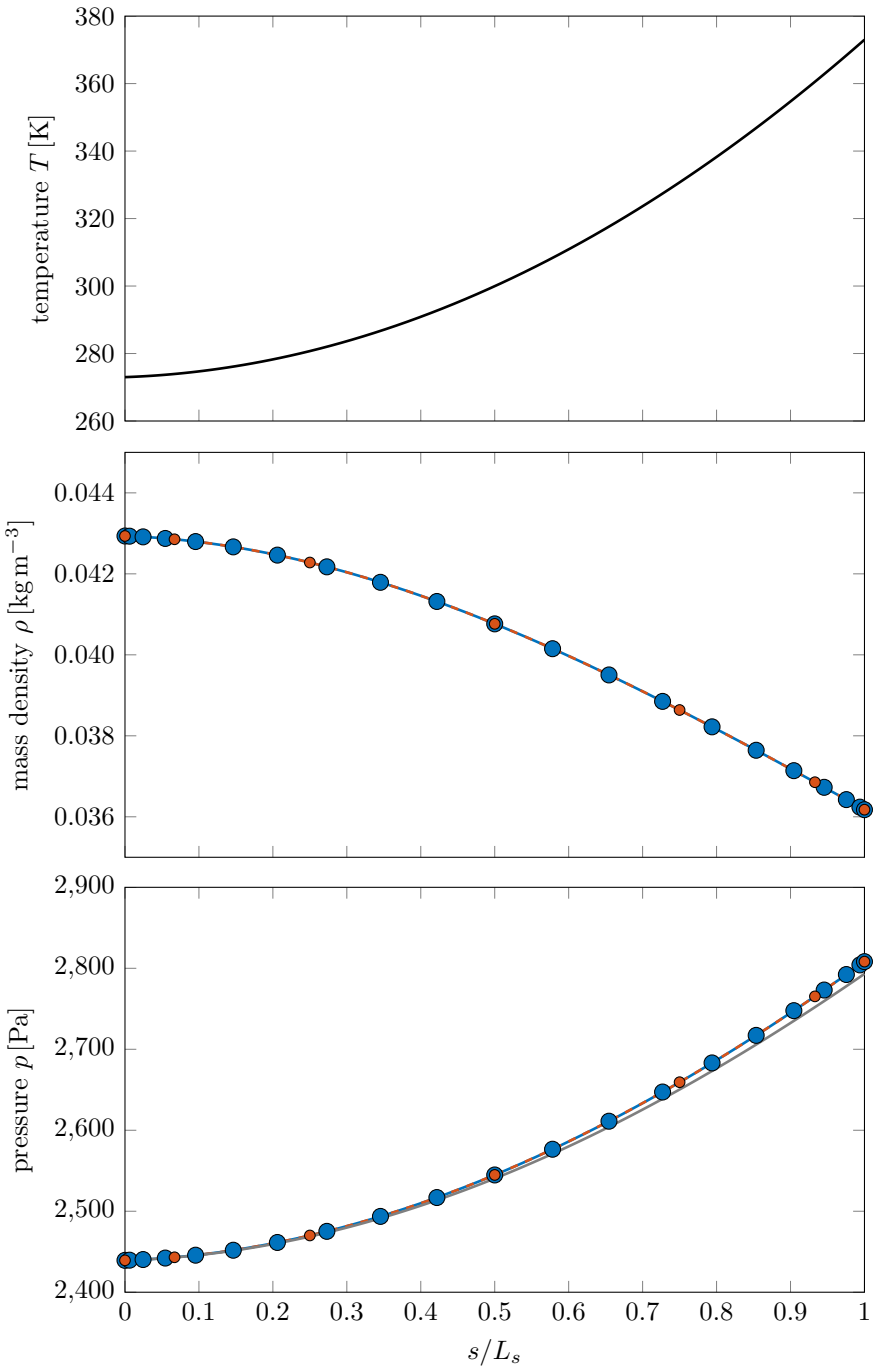

Figure 3.19: **Case 6** – streamwise variation of T (top), ρ (middle) and p (bottom) computed by the steady-IMM for $\Pi = 7$ (● with dashed line) and $\Pi = 21$ (● with solid line). The temperature variation is an input, and is non-linear (with $T_1 = 273$ and $T_\Pi = 373$, as defined in Case 4). The pressure variation computed by the method outlined in [Sharipov, 1999] (——) (equation (3.8)) is shown for comparison.

Chapter 4

IMM for unsteady gas flows

To design many of the future technologies that exploit small-scale flows, it must be possible to model processes at disparate spatial and temporal scales simultaneously: a formidable multiscale problem, which is sometimes possible to treat by exploiting scale separation. Although in princple it is possible to employ a suitable molecular (or kinetic) fluid model to solve the entire flow field, this approach is impractable when studying realistic engineering problems. Non-trivial unsteady (transient) cases are likely to require the use of molecular simulation methods (e.g. direct simulation Monte Carlo (DSMC) method), the results of which are inherently statistical. As an ensemble of realisations are required to account for the statistical uncertainty in estimates of macroscopic properties, the computational effort required is considerable, and in some cases prohibitive. The unsteady-internal-flow multiscale method (unsteady-IMM), developed in this chapter, can be used to efficiently solve such problems, provided a degree of spatio-temporal-scale seperation exists. Typically, the disparity of time scales is far greater than that of length scales; therefore, the performance improvement of the unsteady-IMM (presented here) is expected to be considerably greater than that of the steady-IMM presented in Chapter 2.

In this chapter, the multiscale methodology and validation of the newly-proposed unsteady-IMM is presented, with a focus on time-dependent thermal transpiration. Validation is accomplished by comparison of the (numerical) results with those obtained using the experiment configuration of Rojas-Cárdenas et al. [2013].

4.1 Time-scale separation

Various time-step coupling schemes for hybrid methods exist. The reader is referred to Lockerby et al. [2013] for an in-depth review of these schemes. The time-accurate computations presented in this chapter are performed using the continuous asynchronous (CA) scheme, although other schemes can be used.

Consider a time-scale separated system consisting of M models, where the k th model has a characteristic time scale τ_k, and indexing is ordered such that

$$\tau_k \leq \tau_{k+1} \qquad \text{for } k = 1, 2, \ldots, M-1\,. \tag{4.1}$$

The micro and macro models are represented by $k = 1$ and $k = M$, respectively; models $k = 2$ to $k = M - 1$ are meso models. The degree of time-scale separation $S_{t,k}$ (independent of length-scale separation) between model k and $k + 1$ is

$$S_{t,k} = \frac{\tau_{k+1}}{\tau_k} \geq S_{\texttt{tol.}}\,, \tag{4.2}$$

where the tolerance $S_{\texttt{tol.}}$ dictates the degree of scale separation between the models of the system. For example, $S_{\texttt{tol.}} = \mathcal{O}(10)$. If this condition is not met, the two models are treated as one and coupling is performed conventionally. Because only time-scale separation is discussed in this chapter, S_t is written without its subscript.

In general, the temporal evolution of each model occurs on a separate time scale. The time variable of the k th model is t_k, and each model is represented by

$$\frac{\mathrm{d}X_k}{\mathrm{d}t_k} = F_k\left(X\left(t_k\right)\right)\,, \tag{4.3}$$

where X_k are the set of variables of the k th model, and F_k is some function of the complete system's variables, $X = \{X_1, X_2, \ldots, X_M\}$. It is important to distinguish between the characteristic time scale of the k th model in isolation (τ_k) and the time scale of its variables within the coupled system, as they are potentially different.

To solve this set of models, the independent time variables must be related to each other. The models are conventionally coupled if all time variables are equal (i.e. $t = t_{1,\ldots,M}$). However, models can be advanced at different rates with

$$t_1 = {}^{t_2}\!/_{g_2} = \cdots = {}^{t_M}\!/_{g_M}\,, \tag{4.4}$$

where g_k is the rate that the k th model advances relative to the micro model. This approximation provides a means to exchange fine time scale resolution for long time-scale predictions. The extent to which this assumption is valid depends on the magnitude of S_k. For coupled models that are highly scale separated ($S_k > S_{\texttt{tol.}}$), the smaller-scale model will remain quasi-equilibrated to the dynamics of the larger-scale model: the system will essentially behave as if the models are conventionally coupled. Thus, the aim is to represent the scale-separated system ($> S_{\texttt{tol.}}$) with one that is less, but still considerably, scale separated ($= S_{\texttt{tol.}}$). Acceptable values of g_k are determined in this way; the procedure and constraints are outlined below.

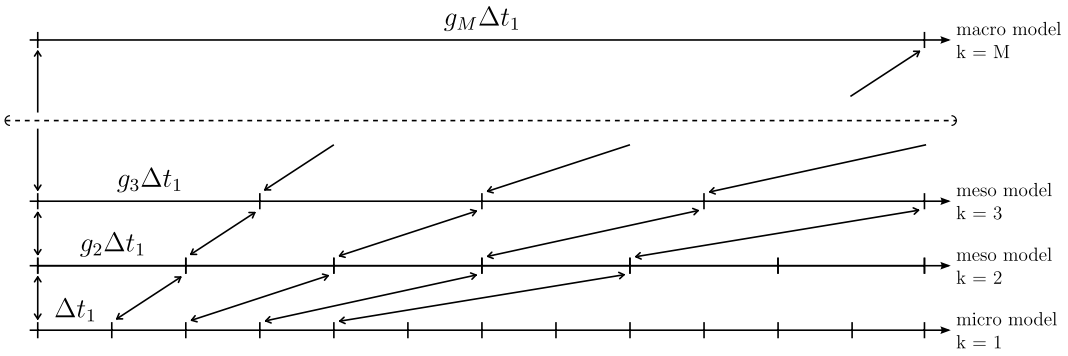

Figure 4.1: The continuous asynchronous (CA) coupling scheme extended to multi-model multiscale systems. Recreated from Lockerby et al. [2015].

A detailed analysis of the error associated with this physical approximation (for a two-model system) are given in [E et al., 2009; Lockerby et al., 2013].

The time step of the k th model is

$$\Delta t_k = g_k \Delta t_1 \,, \tag{4.5}$$

where Δt_1 is the time step used to evolve the micro model (which is defined here as a small fraction of the mean collision time). This forms the basis of the **c**ontinuous micro solution – **a**synchronous (CA) time-step coupling scheme, the numerical implementation of which is illustrated in Fig. 4.1. Note, this is just one of several schemes that may be used for the coupled time advancement of the unsteady-IMM. Micro time-stepping is performed continuously while exploiting time-scale separation by advancing each model at a different rate (according to equation (4.5)). As information is exchanged between the models at every time step, they are asynchronously coupled. It is worth noting that if exchange instances are intermittent, i.e. information is not exchanged at every time step, the **c**ontinuous micro solution – **a**synchronous **i**ntermittent (CAI) time-step coupling scheme is used. This scheme provides additional control by allowing a number of micro-solver time steps to be performed before the exchange of coupling variables (its use is not necessary here).

The aim of the asynchronous coupling scheme (used in this thesis) is to maximise the period over which macro variations are predicted. This is accomplished by maximising the time step in each model subject to the following constraints:

1. The physical approximation of equation (4.4) represents a highly scale-separated system by one that is less so (i.e. has a scale separation of $S_{\mathtt{tol.}}$). This places an upper limit on the enlargement of a time step relative to another:

$$\Delta t_k \leq \frac{S_{k-1}}{S_{\texttt{tol.}}} \Delta t_{k-1} \,. \tag{4.6}$$

2. Numerical accuracy is satisfactory and stability is ensured for each model:

$$\Delta t_k \leq \Delta t_{k,\,\texttt{max}} \,, \tag{4.7}$$

where $t_{k,\texttt{max}}$ is the maximum permissible time step for the k th model, and is predicted as a small fraction of the characteristic time scale τ_k.

Based on these constraints, the time step of each model can be set recursively:

$$\Delta t_k = \min \left\{ \Delta t_{k,\texttt{max}}; \frac{S_{k-1}}{S_{\texttt{tol.}}} \Delta t_{k-1} \right\} \qquad \text{for } k = 2, 3, \ldots, M \,, \tag{4.8}$$

where Δt_1 is set such that the micro model is accurate. Equation (4.8) is used to determine the time step sizes that (temporally) advance the models that describe the system. The cases that are presented illustrate the effectiveness and challenges of employing the physical approximation implied by equation (4.4).

4.2 Time-dependent thermal transpiration

The time-stepping scheme defined in the preceding section is applied to facilitate the coupled time advancement of the unsteady-IMM, which in turn is used to model the transient (macro) pressure response induced by thermal transpiration. Thermal transpiration, which is the rarefied gas phenomenon exploited by the thermal-transpiration compressors, is discussed in Chapter 1, and so is not discussed in detail here. The experimental data of Rojas-Cárdenas et al. [2013] is used to validate the unsteady-IMM; to begin, the experimental configuration is described. The multiscale representation (by the unsteady-IMM) is then detailed and validated.

The experiment configuration of Rojas-Cárdenas et al. [2013] consisted of a borosilicate (glass) channel of circular cross section with radius $r = 242.5 \pm 3.0\,\mu\text{m}$ connecting two reservoirs of volume $V_c = 19.81 \pm 0.54\,\text{cm}^3$ and $V_h = 14.85 \pm 0.40\,\text{cm}^3$. The length of the channel in the streamwise (s-)direction was $L_s = 52.7 \pm 0.1\,\text{mm}$. One of the reservoirs was heated to generate a temperature distribution through the channel (defined by an exponential function). The other reservoir was held at ambient temperature. Note, the subscripts c and h denote that the variable is associated with the unheated and heated reservoirs, respectively. The pressure of the gas in the reservoirs (p_c and p_h) was measured using capacitance diaphragm pressure gauges.

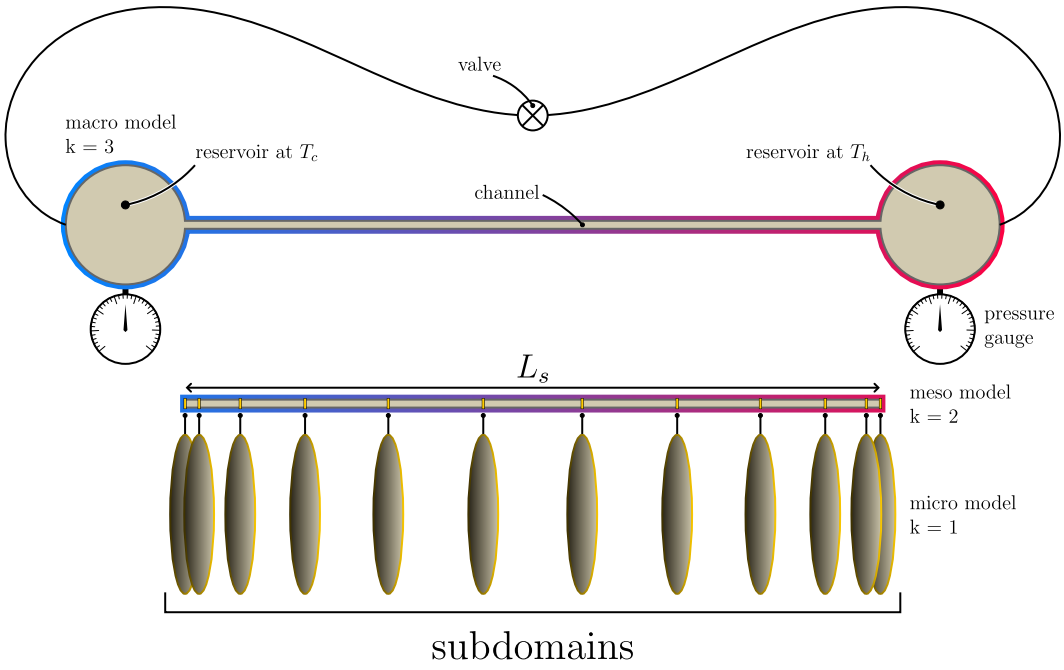

Figure 4.2: A multiscale representation of the experimental configuration of Rojas-Cárdenas et al. [2013], used to study time-dependent thermal transpiration. The pressure gauges indicate where experimental values of pressure are measured. Only the effects of (instantaneously) opening/closing the valve are modelled. These components are not included in the numerical representation of the system.

This system was used to study thermal transpiration as a time-dependent phenomenon; from an initial stationary state where only a thermal-transpiration flow was allowed to develop ($p_c \approx p_h \approx$ const.), to a final stationary state where the net mass flow rate in the channel was zero. This final state was reached by allowing p_c and p_h to evolve, resulting in the generation of a pressure-driven flow which opposed the thermally-driven flow. Argon gas is simulated in all cases.

The unsteady-IMM is used to replicate the experimental configuration and procedure described. The need for the unsteady-IMM arises for the same reasons as previously discussed: we are treating a non-equilibrial flow (thermal transpiration is a non-equilibrium phenomenon [Reese et al., 2003]), and a full molecular or gas-kinetic treatment is computationally intractable.

4.2.1 Macro model

The multiscale representation of the system is comprised of three coupled models, applying the appropriate modelling assumptions to each: the reservoir model (macro, $k = 3$); the channel model (meso, $k = 2$); and the gas-kinetic model (micro,

$k = 1$); see Fig. 4.2. The macro model defining the temporal evolution of p_c and p_h is obtained from mass conservation and by assuming an ideal gas:

$$\begin{aligned} \frac{\mathrm{d}p_c}{\mathrm{d}t_3} &= -\frac{RT_c}{V_c}\dot{m}_{s=0}\,, \\ \frac{\mathrm{d}p_h}{\mathrm{d}t_3} &= -\frac{T_h}{T_c}\frac{V_c}{V_h}\frac{\mathrm{d}p_c}{\mathrm{d}t_3}\,. \end{aligned} \tag{4.9}$$

Although it can easily be accounted for, it is assumed that there is no considerable change in the mass of gas within the channel.

4.2.2 Meso model

The meso model is derived from the continuity equation (2.2) integrated over the cross-sectional area A of the channel. This relates the mass flow rate and pressure:

$$\frac{\partial p}{\partial t_2} + \frac{RT}{A}\frac{\partial \dot{m}}{\partial s} = 0\,. \tag{4.10}$$

The meso model is coupled to the macro model by the boundary conditions: $p = p_c$, $\dot{m} = \dot{m}_{(s=0)}$ at $s = 0$; and $p = p_h$ at $s = L_s$, where $L_s = 52.7 \pm 0.1\,\mathrm{mm}$. The temperature variation is prescribed by [Rojas-Cárdenas et al., 2013]

$$T\left(sL_s^{-1}\right) = \theta_a\left[\exp\left(\theta_b sL_s^{-1}\right) - 1\right] + T_c\,, \tag{4.11}$$

where the constants $\theta_a = 0.655$, $\theta_b = 4.40$, $T_c = 300.0\,\mathrm{K}$ (for cases where $\Delta T = 53.5\,\mathrm{K}$) and $\theta_a = 0.822$, $\theta_b = 4.47$, $T_c = 301.0\,\mathrm{K}$ (for cases where $\Delta T = 71.0\,\mathrm{K}$).

4.2.3 Micro model

By relating mass flow rate to pressure and temperature:

$$\frac{\partial \dot{m}}{\partial t} = \mathcal{F}\left(\frac{\partial T}{\partial s}\,;\frac{\partial p}{\partial s}\,;\mathcal{X}\right)\,, \tag{4.12}$$

the micro model $\mathcal{F}$ provides a means to close the entire system. The container $\mathcal{X}$ holds information regarding the molecular structure of the gas. The micro model is a streamwise-distributed array of low-variance deviational simulation Monte Carlo (LVDSMC) subdomain instances (see Fig. 4.2). The flow in each (streamwise periodic) subdomain is driven by an effective body force, which represents the streamwise pressure and temperature gradients occurring at the streamwise position s_i in the meso domain (changes in density at s_i are also calculated, as with the steady-IMM).

The micro model is thus coupled to the meso model by the streamwise pressure gradient, pressure, and mass flow rate at Chebyshev points on the interval $[0, L_s]$, as defined by equation (2.25). For the simulations presented here, $\Pi = 8$ subdomains are used. For accuracy, the spatial derivatives in equations (4.10) and (4.12) are obtained using a discrete cosine transform (DCT). The type-II DCT (`FFTW_REDFT00`), and its inverse (`FFTW_REDFT01`), from the Fastest Fourier Transform in the West (FFTW) software library are used, as they are highly optimised for arbitrary length data, i.e. any Π. Note, there are no constraints on the real input data. Equation (4.10) then provides ρ_i^n in each subdomain at the proceeding time step n, via an Euler approximation. The pressure gradient in each subdomain at the proceeding time step is simply the spatial derivative of pressure, found by a DCT.

As the cross section of the channel (meso domain) connecting the reservoirs is not rectangular, the original implementation of the LVDSMC method, which only supports simulation on two-dimensional structured grids, was modified to allow for the simulation on two-dimensional unstructured grids. This allows us to consider arbitrarily complex (two-dimensional) geometries. In Chapter 5, this extended implementation of the LVDSMC method (the ULVDSMC method is discussed in Appendix A) is used to study the influence of the cross-sectional shape on thermal-transpiration compressor (and implicitly Knudsen compressor) performance.

4.2.4 Characteristic time scales

Viscous development within the cross section of the channel defines the characteristic time scale of the micro model (see Appendix B for derivation):

$$\tau_1 = \frac{\bar{\rho} r^2}{\bar{\mu}}\,, \tag{4.13}$$

where $\bar{\rho}$ and $\bar{\mu}$ are the average initial density and viscosity of the gas. By assuming a quasi-steady velocity profile (which is only valid for $t \gg \tau_1$), the characteristic time scales of the meso and macro models can be estimated from equations (4.10) and (4.9), respectively (again, see Appendix B for derivation):

$$\tau_2 = \frac{\bar{\mu} L_s^2}{\bar{p} r^2}\,, \tag{4.14}$$

and,

$$\tau_3 = \frac{\bar{\mu} L_s V}{\bar{p} r^4}\,, \tag{4.15}$$

where $\bar{p}$ is the average initial pressure, and $V = V_c + V_h$. These variables are used to calculate the degree of scale separation between the models of the system.

By forcing the temporal derivative of pressure in equation (4.10) to be zero, the initial stationary state of the experimental procedure is simulated by the unsteady-IMM. To ensure that the thermal-transpiration flow is fully developed, the duration of the initial stationary state is set to be much greater than τ_2. The initial pressure in a reservoir is calculated as the average of the experimentally measured transient pressure variation (in that reservoir) obtained during the initial stationary state. As stated in §4.1, time step sizes are set by equation (4.8). The time step of the micro solver is $\Delta t_1 = \Delta x/\sqrt{2RT}$, where Δx is the minimum cell size.

4.2.5 Coupling algorithm

Pseudocode for the implementation of the unsteady-IMM (which utilises the Open Message Passing Interface library to simultaneously run Π micro-solver instances) applied to study time-dependent thermal transpiration is presented below:

Algorithm 3 Part I: the unsteady internal-flow multiscale method

```
1: procedure UNSTEADYIMM                          ▷ unsteady-IMM
2:     MPI_INIT                                   ▷ initialise MPI
3:     MPI_COMM_SIZE(Π)                           ▷ get the number of processes, Π
4:     MPI_COMM_RANK(i)                           ▷ get the process identifier, i

Require: set thermodynamic and flow conditions from file
Require: set the time-step sizes
```

The unsteady-IMM is implemented as a single program, multiple data (SPMD) application: a Π-process parallel application, running Π copies of the executable. Each process, which operates on different data, simulates a single subdomain. Before time stepping is initiated, the time-step sizes of the $M = 3$ models are determined by equation (4.8). Following the initialisation of thermodynamic conditions, the pressure gradient p_s[1] is calculated by a DCT. The program then proceeds with:

Algorithm 4 Part II: the unsteady internal-flow multiscale method

```
5:     for step ← 1, N_t do        ▷ N_t is the total number of simulated time steps
6:         t_3 ← stepΔt_3                                  ▷ macro time scale
7:         t_2 ← stepΔt_2                                  ▷ meso time scale
8:         t_1 ← stepΔt_1                                  ▷ micro time scale

9:         TIMESTEP(p_s,T_s,ϵ,Kn)   ▷ perform micro time step using current values
10:        PROPERTIES               ▷ update hydrodynamic properties, including ṁ_i

11:        MPI_GATHER(ṁ, ρ)                                ▷ gather values from processes
```

[1]Subscripts s and t denote first derivatives with respect to s and t, respectively.

A single micro time step (according to the CA time-stepping scheme) has been performed, and (by calling the `properties` subroutine) each process (with a different value of p_s) has calculated a single value of $\dot{m}$. `MPI_Gather` instructs each process to send the contents of its send buffer, which contains the local scalar variables $\dot{m}$ and ρ, to the root process, $i = 1$. Note, this collective communication operation is blocking, meaning that all processes are synchronised at the call to `MPI_Gather`. The root process performs operations on the collected data to compute updated values of temporally evolving variables that inform the micro model. The following procedures are those which primarily differentiate this implementation of the unsteady-IMM as an approach to study time-dependent thermal transpiration:

Algorithm 5 Part III: the unsteady internal-flow multiscale method

if $i == 1$ **then** ▷ 'root' process to update flow conditions
  $\dot{m}_{s,i=1,\ldots,\Pi} \leftarrow$ DCTDIFF$(\dot{m}_{i=1,\ldots,\Pi})$ ▷ $\dot{m}_s$ is a vector of length Π

▷ **MACRO MODEL**
  if step $< N_{t_{\text{int.}}}$ **then** ▷ during initial stationary state
    $\rho_{t,i=1} \leftarrow 0$ ▷ do not allow $\rho_{i=1}$ to evolve
    $\rho_{t,i=\Pi} \leftarrow 0$ ▷ do not allow $\rho_{i=\Pi}$ to evolve
  else ▷ thermal-transpiration flow is fully developed
    $\rho_{t,i=1} \leftarrow \dot{m}_{i=1,\ldots,\Pi}/V_c$ ▷ allow $\rho_{i=1}$ to evolve
    $\rho_{t,i=\Pi} \leftarrow \dot{m}_{i=1,\ldots,\Pi}/V_h$ ▷ allow $\rho_{i=\Pi}$ to evolve
  end if
  $\rho_{i=1} \leftarrow \rho_{i=1} + \rho_{t,i=1}\Delta t_3$ ▷ update $\rho_{i=1}$ using Euler method
  $\rho_{i=\Pi} \leftarrow \rho_{i=\Pi} + \rho_{t,i=\Pi}\Delta t_3$ ▷ update $\rho_{i=\Pi}$ using Euler method

▷ **MESO MODEL**
▷ update ρ according to equation (4.10): array operation for $i = 2, \ldots, \Pi - 1$
  $\rho_{i=2,\ldots,\Pi-1} \leftarrow \rho_{i=2,\ldots,\Pi-1} + \left(\dot{m}_{s,i=2,\ldots,\Pi-1}/A_{i=2,\ldots,\Pi-1}\right)\Delta t_2$

  $p_{i=1,\ldots,\Pi} \leftarrow \rho_{i=1,\ldots,\Pi} R T_{i=1,\ldots,\Pi}$ ▷ ideal gas law
  ▷ spatial derivative of updated p
  $p_{s,i=1,\ldots,\Pi} \leftarrow$ DCTDIFF$(p_{i=1,\ldots,\Pi})$ ▷ p_s is a vector of length Π
  WRITE ▷ write variables to temporary array/file
end if
MPI_Scatter(p_s, ρ) ▷ scatter updated values to processes
UPDATE ▷ update subdomain conditions
end for
MPI_Finalize ▷ termination of MPI execution environment
end procedure

The unsteady-IMM has been implemented in Fortran 95 (with, for efficiency, the ULVDSMC micro solver embedded within the same program). The resulting program has been used to produce the results presented in the following section.

case	figure	ΔT [K]	p_{h_i} [Pa]	p_{c_i} [Pa]	$S_{\texttt{tol.}}$	$\Delta t_3/\Delta t_1$
1	4.3a	53.5	161.88	161.99	20	25.22×10^3
2	4.3b	71.0	52.46	52.44	10	976.2×10^3
3	4.3c	71.0	108.06	107.91	20	57.77×10^3
4	4.3d	71.0	237.74	237.75	20	11.92×10^3

Table 4.1: Thermodynamic conditions and the parameter values relating to the control and degree of time-scale separation for each validation case.

4.2.6 Discussion of results

For four separate cases, Fig. 4.3 shows the transient response of the pressure in each reservoir after the system is instantaneously closed; there is good agreement between the experimental measurements and the multiscale solution. The asymmetry of the responses around the initial pressure is caused by the different reservoir volumes ($V_c > V_h$). The thermodynamic conditions, $S_{\texttt{tol.}}$, and the degree of scale separation between the micro and macro models are presented in Table 4.1.

All multiscale solutions were computed within less than three hours using $\Pi = 8$ independent central processing units (cores). The frequent communication between these cores is facilitated by the Open Message Passing Interface (MPI) library. If the time steps are set to be equal (i.e. a conventional synchronous coupling), the execution time (utilising the same hardware) of case two is $\Delta t_3/\Delta t_1 = 976{,}000\times$ greater: a computational saving that allows for the solution of an otherwise computationally intractable problem. In fact, if the saving due to spatial multiscaling is also considered, the saving over conventional modelling is far greater than this.

Figure 4.5 demonstrates the impact of decreasing the value of Π; the accuracy of the solution is unacceptable if $\Pi < 6$. Figure 4.2 illustrates the coupling of the $M = 3$ models, and shows that the subdomains at the limits of the interval $[0, L_s]$ are used to compute the temporal evolution of pressure in the reservoirs. All other subdomains are used to inform and evolve the meso model. For small values of Π, the number of collocation points is insufficient to accurately recover the continuous spatial derivative of mass flow rate (equation (4.10)). Therefore, the temporal derivative of mass density (or pressure) is also inaccurate.

Figure 4.4 shows the impact of increasing $S_{\texttt{tol.}}$; a similar result is obtained in all cases, but with lower noise at higher $S_{\texttt{tol.}}$. This highlights an important general limitation of multiscaling with stochastic models (e.g. DSMC) or inherently noisy methods (e.g. MD): fewer time steps result in less sampling, and thus more noise. The trade-off in continuum-particle multiscaling is summarised as

$$\text{fine-scale accuracy} \longleftrightarrow \text{noise \& large-scale prediction.} \tag{4.16}$$

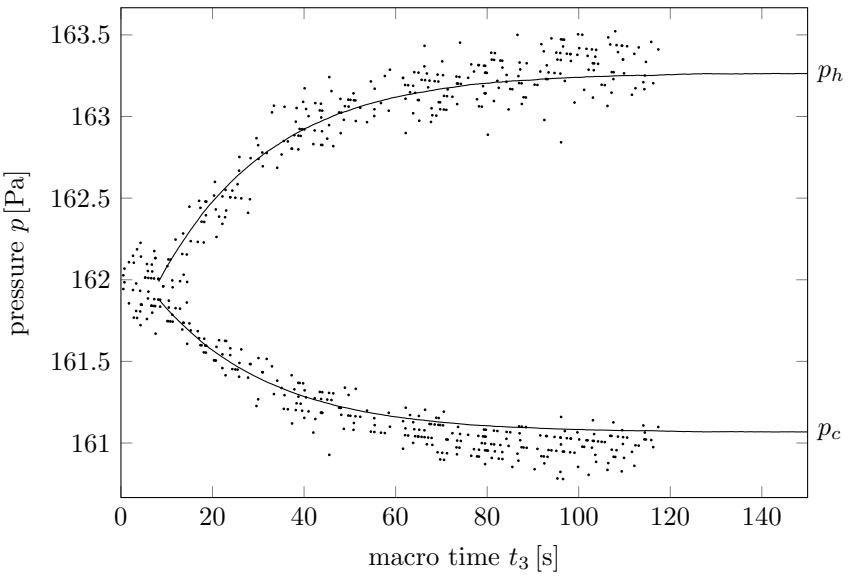

(a) Comparison of experimental data and multiscale solution for time-dependent thermal transpiration with $\Delta T = 53.5\,\mathrm{K}$ and initial pressures $p_{h_i} = 161.99\,\mathrm{Pa}$, $p_{c_i} = 161.88\,\mathrm{Pa}$.

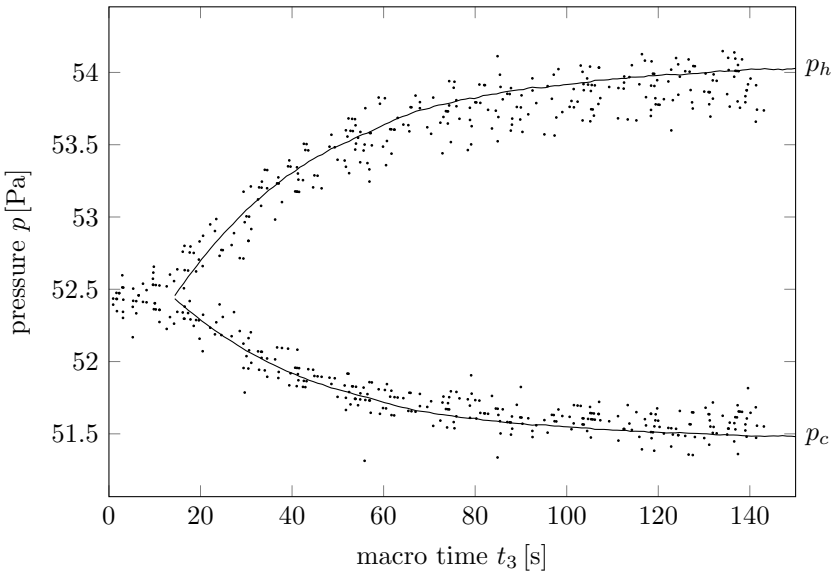

(b) Comparison of experimental data and multiscale solution for time-dependent thermal transpiration with $\Delta T = 71.0\,\mathrm{K}$ and initial pressures $p_{h_i} = 52.46\,\mathrm{Pa}$, $p_{c_i} = 52.44\,\mathrm{Pa}$.

Figure 4.3: Plots of reservoir pressure variation. Experimental data (·) of Rojas-Cárdenas et al. [2013] and the solution from the multiscale simulation (——).

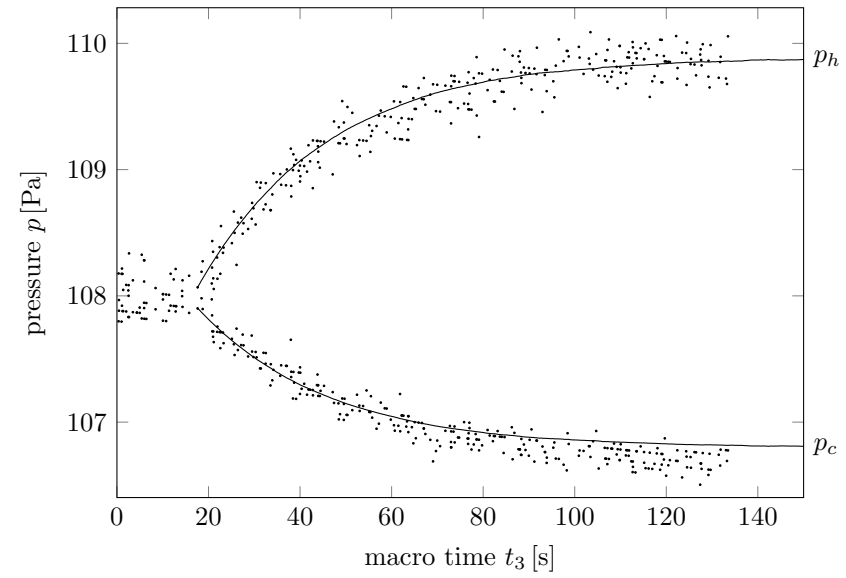

(c) Comparison of experimental data and multiscale solution for time-dependent thermal transpiration with $\Delta T = 71.0\,\mathrm{K}$ and initial pressures $p_{h_i} = 108.06\,\mathrm{Pa}$, $p_{c_i} = 107.91\,\mathrm{Pa}$.

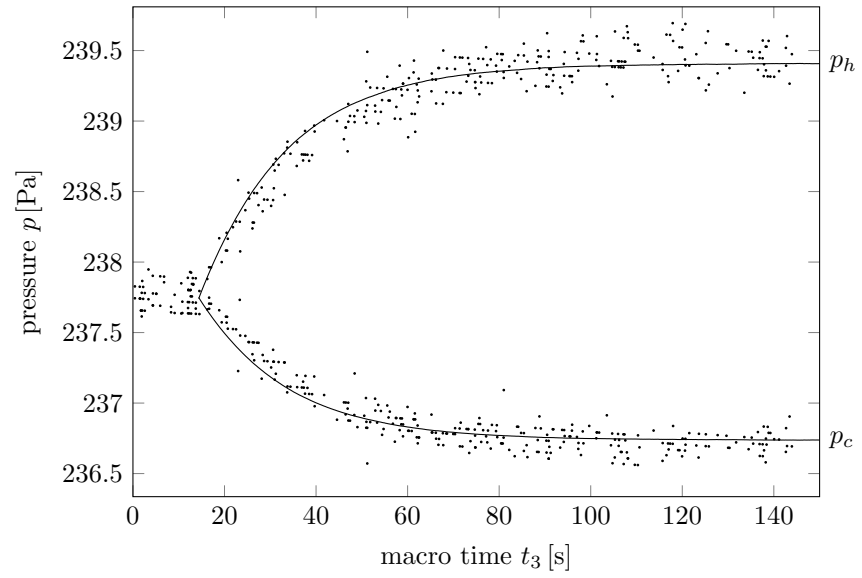

(d) Comparison of experimental data and multiscale solution for time-dependent thermal transpiration with $\Delta T = 71.0\,\mathrm{K}$ and initial pressures $p_{h_i} = 237.74\,\mathrm{Pa}$, $p_{c_i} = 237.75\,\mathrm{Pa}$.

Figure 4.3: Plots of reservoir pressure variation. Experimental data (·) of Rojas-Cárdenas et al. [2013] and the solution from the multiscale simulation (——).

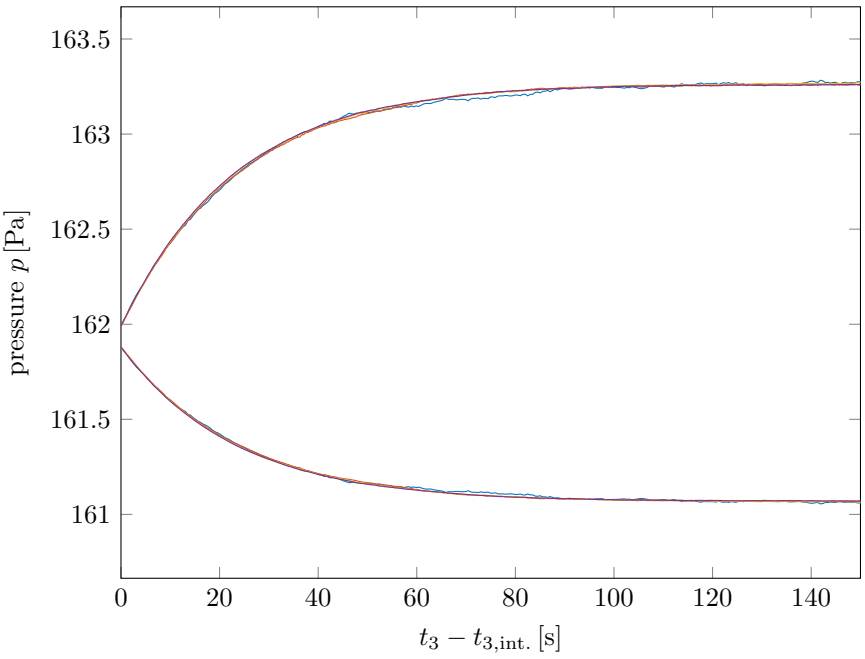

Figure 4.4: For Case 1: variation of reservoir pressure with time for variable $S_{\texttt{tol.}}$: $S_{\texttt{tol.}} = 10$ (——), $S_{\texttt{tol.}} = 20$ (——), $S_{\texttt{tol.}} = 30$ (——), and $S_{\texttt{tol.}} = 40$ (——).

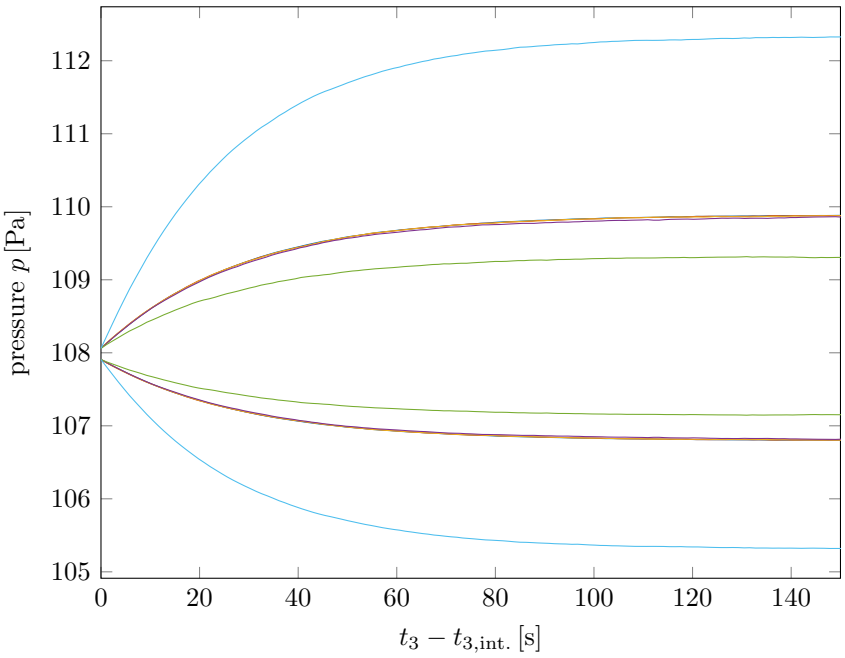

Figure 4.5: For Case 3: variation of reservoir pressure with time for variable Π: $\Pi = 12$ (——), $\Pi = 8$ (——), $\Pi = 6$ (——), $\Pi = 4$ (——), and $\Pi = 3$ (——).

Chapter 5

Knudsen compressor design

The numerical methods outlined in Chapters 2 and 4 are applied to the design optimisation of thermal-transpiration compressors [Knudsen, 1909b, 1910], solid-state devices that can facilitate the compression or pumping of a gas in microsystems. The numerous aspects of their design reinforce the need for computationally efficient modelling techniques by which design optimisation can be performed. Before we proceed, thermal-transpiration (and Knudsen) compressors are introduced.

5.1 Thermal-transpiration compressors

The ability to generate a vacuum by means of thermal-transpiration (a rarefied gas phenomenon by which gas transport occurs in the direction of relatively low to high temperature; see Chapter 1 for more details) allows us to overcome the many challenges and limitations associated with the miniaturisation of conventional vacuum pumps, the reliability of which suffers due to the relative increase of frictional forces over inertial forces at the microscale [McNamara and Gianchandani, 2005]. A micromachined pump that exploits thermal-transpiration has a variety of applications, from micro-gas chromatography [Liu et al., 2011] to the actuation of gases for microplasma manufacturing [Wilson and Gianchandani, 2001].

Thermal-transpiration compressors consist of two reservoirs connected by a 'capillary' with height L of the order of the mean free path λ. The temperature of the gas in each reservoir is different; assume that one reservoir is heated to a temperature T_h and the other is held at ambient temperature T_c (as in the experimental configuration of Rojas-Cárdenas et al. [2013], described in Chapter 4). A streamwise temperature gradient then exists along the surfaces of the capillary. By thermal transpiration, a flow will occur in the direction from T_c to T_h. If the system is closed, the pressure in the heated reservoir will increase as the pressure in the other reservoir decreases: a pressure gradient is generated due to thermal transpira-

tion. At the final stationary state where the pressure-driven and thermally-driven mass flow rates balance, zero net mass flow rate is achieved, i.e. $\dot{M} = 0$. As will be shown in this chapter, multiple capillaries can be used to increase the rate at which the pressure difference is maximised (we denote the maximum pressure difference at the final stationary state as $\Delta\tilde{p}$: this is a gauge of performance).

The thermal-transpiration compressor (described above) is the basis for a staged device: the Knudsen compressor (see Muntz et al. [2002]; Young et al. [2005] for a brief overview of the origins of Knudsen compressors), which provides greater compression. Each stage consists of a capillary section and connecting section. The temperature increases in the capillary section (consisting of multiple capillaries), causing a pressure increase by thermal transpiration. All capillaries end at a connector section, where the pressure is approximately constant and the temperature returns to that at the start of the stage (T_c). For Knudsen compressors to be efficient, it is important that the energy use (for heating) per unit mass of process gas upflow is minimised. The problem of optimisation is investigated in this chapter.

In the following section, the steady-internal-flow multiscale method (steady-IMM), which is presented in Chapter 2, is used to study the influence of a streamwise variation in cross-sectional geometry on $\Delta\tilde{p}$. Following this, an extended implementation of the low-variance deviational simulation Monte Carlo (LVDSMC) method (that allows for the simulation of arbitrary two-dimensional geometries on unstructured meshes; see Appendix A for details) is used to inform the design of the capillaries of thermal-transpiration compressors. The trade-off between two performance indicators is studied by varying the cross-sectional geometry, and packing density of a bundle of capillaries. Only simple cross-sectional shapes are considered, as these are more easily manufactured by microfabrication techniques. Performance indicators are: (a) the maximum pressure difference $\Delta\tilde{p}$; and (b) the time required to obtain $\Delta\tilde{p}$, referred to as the development time. The findings are verified by applying the unsteady-internal-flow multiscale method (unsteady-IMM), presented in Chapter 4, to compute the temporal evolution of pressure in the reservoirs.

5.2 Varying cross section

Consider a single channel in isolation, with conditions set such that the maximum pressure difference $\Delta\tilde{p}$ is generated. The question of how the cross section of the channel affects this pressure difference is posed. In this section, the development time is disregarded as a performance indicator, and the steady-IMM is used. Three cases are presented, each consisting of a converging-diverging channel.

The streamwise length L_s of the channel is varied, altering the streamwise slope of its walls. The width $L_x = 0.5\,\mu\text{m}$ is constant for all cases. The height L_y ranges from $0.3\,\mu\text{m}$ to $0.5\,\mu\text{m}$ at the throat and inlet/outlet of the channel, respectively.

5.2.1 Linear temperature variation

A linear streamwise temperature distribution [K] is prescribed: $T(s) = \alpha s + 273$, where $\alpha = 4.2 \times 10^6$. Figure 5.1 shows the streamwise pressure variation at the centreline of a converging-diverging channel, which is solved for by setting $\dot{M} = 0$ (discussed in Chapters 2 and 3), with $L_s = 24\,\mu\text{m}$. With the variation in the channel height L_y disregarded, the computation is repeated to obtain the pressure variation in a (simple) channel with square cross section $\left(L_x = L_y = 0.5\,\mu\text{m}\right)$. With all other parameters unchanged, a negligible difference in the pressure variation is observed. The percentage difference between the pressure at $s/L_s = 1$ in the converging-diverging and simple channels is $\ll 0.01\,\%$. For the sake of accuracy, the computations presented in this section are all performed with $\Pi \geq 21$.

Figure 5.2 shows the streamwise pressure variation at the centreline of two other converging-diverging channels, the streamwise lengths of which are $L_s = 48\,\mu\text{m}$ and $96\,\mu\text{m}$. For comparison, two simple channels with square cross section $\left(L_x = L_y = 0.5\,\mu\text{m}\right)$ are also modelled. All other parameters are unchanged; the streamwise pressure variation at the centreline of these channels is also shown in Fig. 5.2. Again, the pressure variation appears to be relatively unaffected by the very significant modification to the geometry. For $L_s = 48\,\mu\text{m}$, the percentage difference between the pressure at $s/L_s = 1$ in the converging-diverging and simple channels is $0.30\,\%$. For $L_s = 96\,\mu\text{m}$, this percentage difference is $0.52\,\%$. This case is repeated for $\Pi = 31$ with no significant change in the solution (see Fig. 5.2). Therefore, it is reasonable to assume that any discrepancy between the pressure at $s/L_s = 1$ in the converging-diverging and simple channels is physical.

These results suggest that thermal-transpiration compressor design is fairly insensitive to streamwise variations in cross-sectional geometry. A potential reason for the lack of any change in the streamwise pressure variation (despite the significant loss of internal surface area) may be due to the increased Knudsen number in the vicinity of the constriction. As fewer molecules are present to obstruct the free flight of other molecules, which carry the properties acquired at their origin, this favours thermal transpiration. Further work should involve a thorough investigation to verify this observation. As a preliminary check, however, the geometry shown in Fig. 5.3a (which, although similar to the converging-diverging channel shown in Fig. 3.1a, only converges to the constriction) with $L_s = 24\,\mu\text{m}$ and $\Pi = 21$,

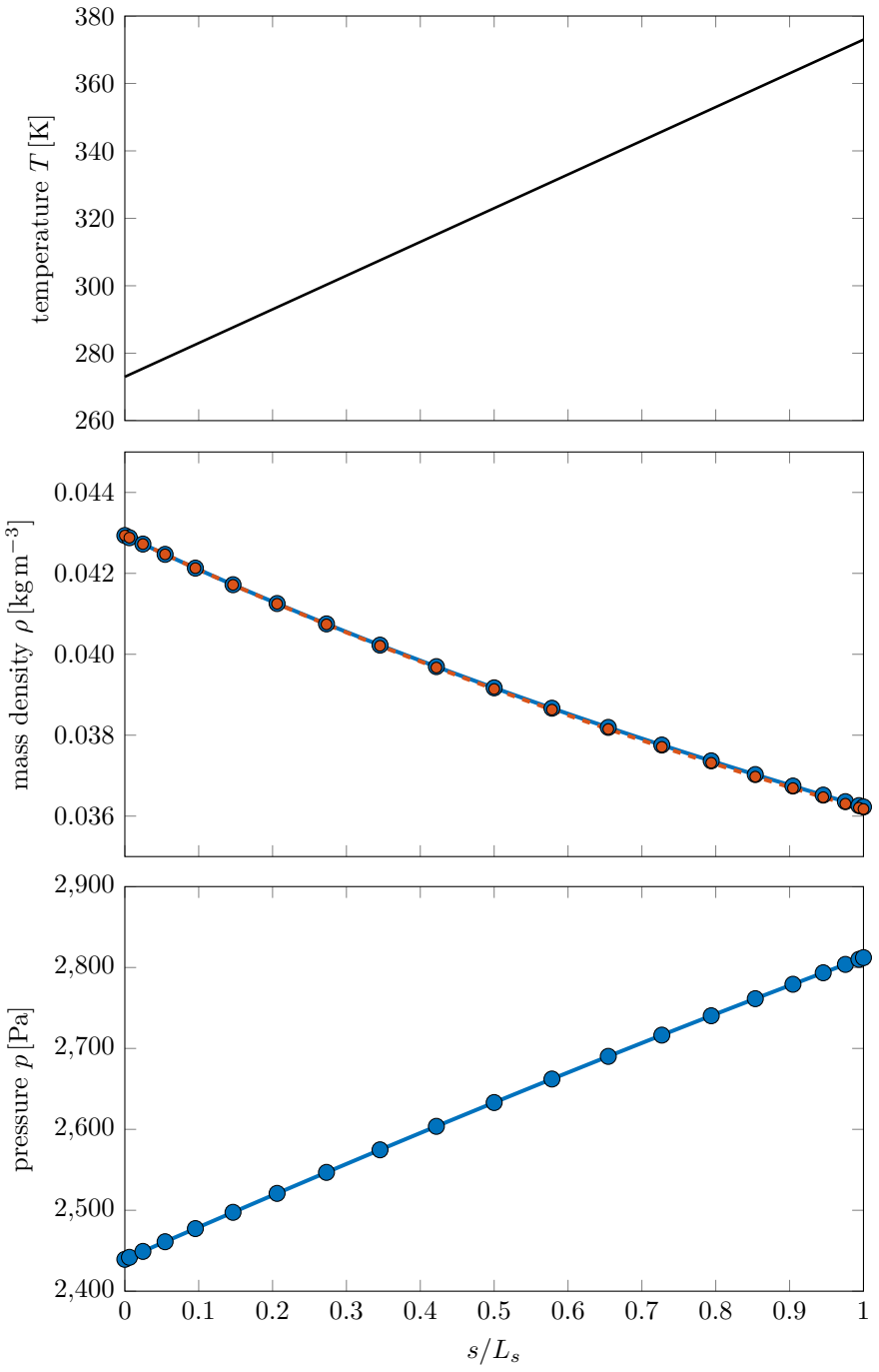

Figure 5.1: Streamwise variation of T (top), ρ (middle) and p (bottom) computed by the steady-IMM for $\Pi = 21$ at the centreline of a converging-diverging channel (● with solid line). The case is repeated for a simple channel (with square cross section $L_x = L_y = 0.5\,\mu\text{m}$). The density variation at the centreline of this simple channel (● with dashed line) is also shown: a small difference is observed. The temperature variation is an input and is shown for reference; a linear variation is prescribed.

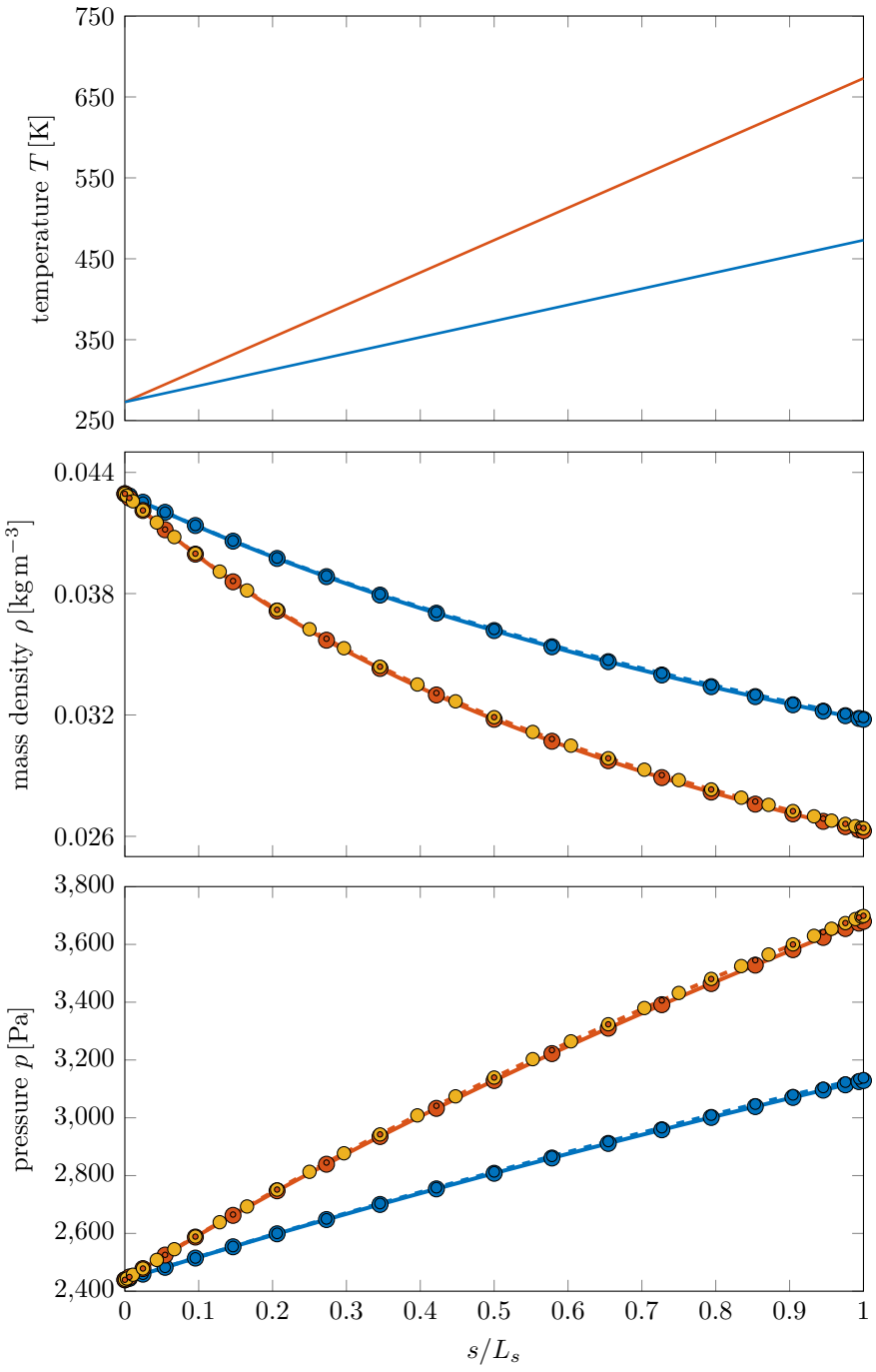

Figure 5.2: Streamwise variation of T (top), ρ (middle) and p (bottom) computed by the steady-IMM for $\Pi = 21$. Two cases where $L_s = 48\,\mu\text{m}$: simple channel (● with solid line), and converging-diverging channel (● with dashed line). Two cases where $L_s = 96\,\mu\text{m}$: simple channel (● with solid line), and converging-diverging channel (● with dashed line). The case where $L_s = 96\,\mu\text{m}$ for a converging-diverging channel is repeated for $\Pi = 31$ (●); the variations of ρ and p are unchanged.

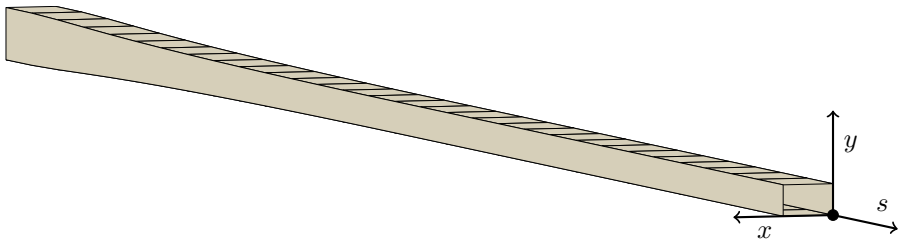

(a) A converging channel.

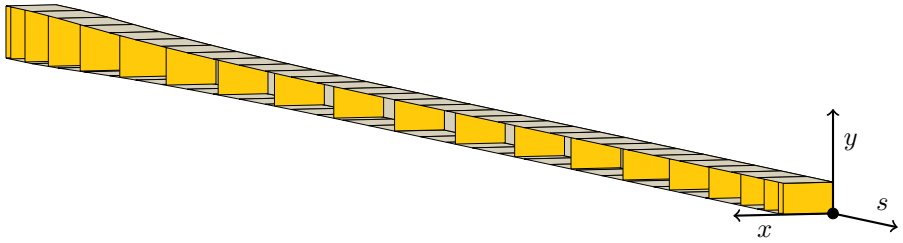

(b) For $\Pi = 21$, a converging channel: streamwise non-periodic.

Figure 5.3: Subdomain spacing in a converging channel.

is also considered. If our assumption is correct, simply modifying the cross-sectional area at the outlet of the channel should not influence the maximum pressure difference $\Delta\tilde{p}$. Figure 5.4 confirms this; no appreciable difference is observed for a simple channel, a converging-diverging channel (Fig. 3.1a), and a converging channel (Fig. 5.3a) (where $L_s = 24\,\mu\text{m}$ for all). In addition, the fundamental equation $\tilde{p}_h/\tilde{p}_c = \sqrt{T_h/T_c}$ [Reynolds, 1879] (which is only accurate in the limit of free-molecular flow), suggests that no difference should be observed as $\text{Kn} \to \infty$.

5.2.2 Non-linear temperature variation

The temperature distribution [K] is modified: $T(s) = \alpha s^2 + \beta s + 273$, where $\alpha = 160 \times 10^9$ and $\beta = 330 \times 10^3$. Figure 5.5 shows the streamwise pressure variation at the centreline of a converging-diverging channel with $L_s = 24\,\mu\text{m}$. The simulation is repeated to obtain the pressure variation in a (simple) channel with square cross section. With all other parameters unchanged, a negligible difference in the pressure variation is observed. At $s/L_s = 1$ the difference is $\ll 0.01\,\%$.

The result further indicates a robustness of thermal-transpiration compressors performance: it is not necessary to precisely apply a streamwise temperature variation to achieve a desired $\Delta\tilde{p}$. To understand why, assume that $\dot{M} = 0$ (at the final stationary state with zero net mass flow rate). By conservation of mass:

$$0 = \dot{M} = -a\,\frac{\mathrm{d}p}{\mathrm{d}s} + b\,\frac{\mathrm{d}T}{\mathrm{d}s}\ . \tag{5.1}$$

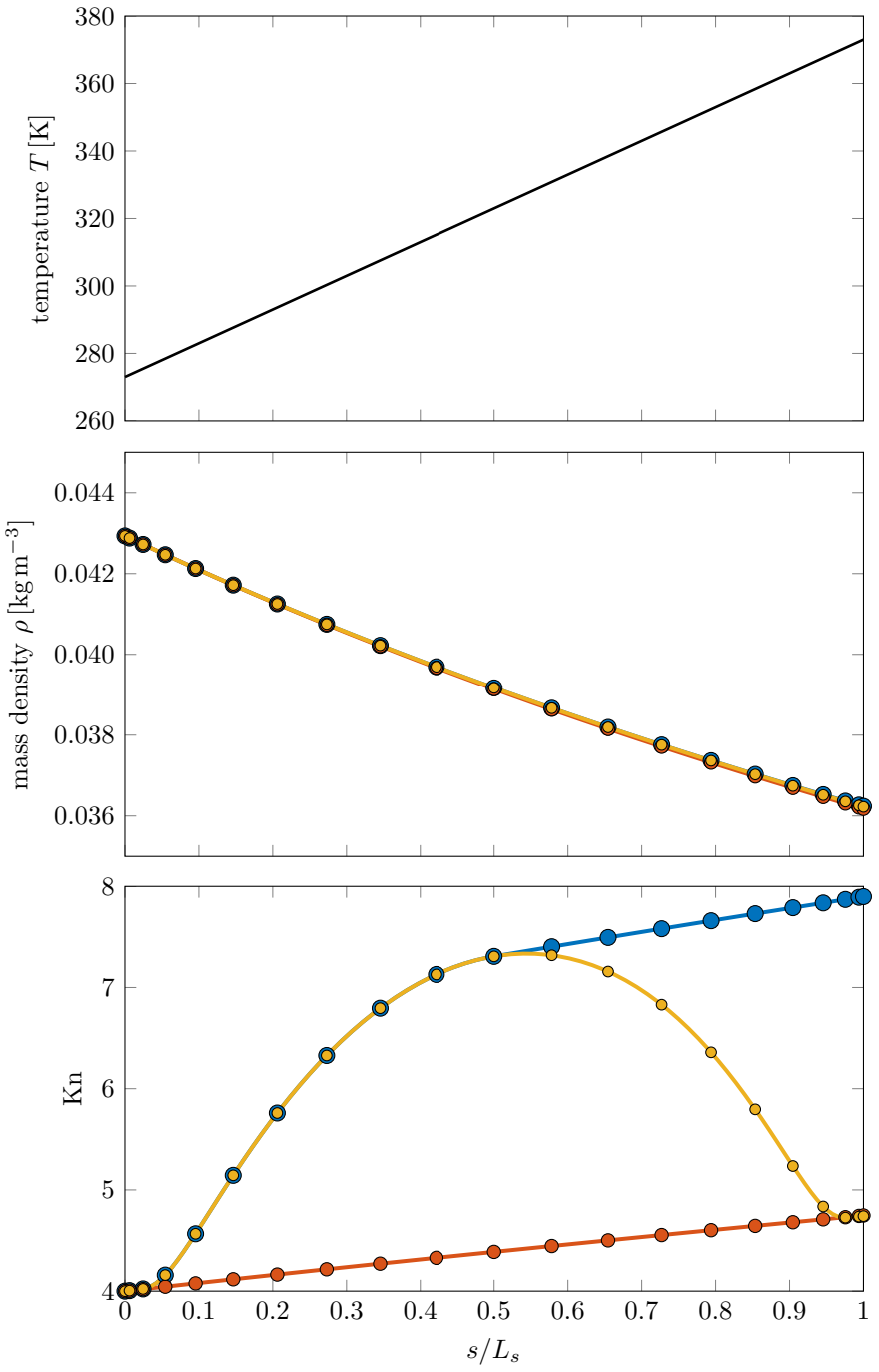

Figure 5.4: Streamwise variation of T (top), ρ (middle) and Knudsen number (Kn) (bottom) computed by the steady-IMM for $\Pi = 21$. Three different geometries (with $L_s = 24\,\mu\text{m}$) are considered: a simple channel with square cross section (● with solid line), a converging-diverging channel (● with solid line) (Fig. 3.1a), and a converging channel (● with solid line) (Fig. 5.3a). The temperature variation is an input; the linear variation shown is prescribed in all cases.

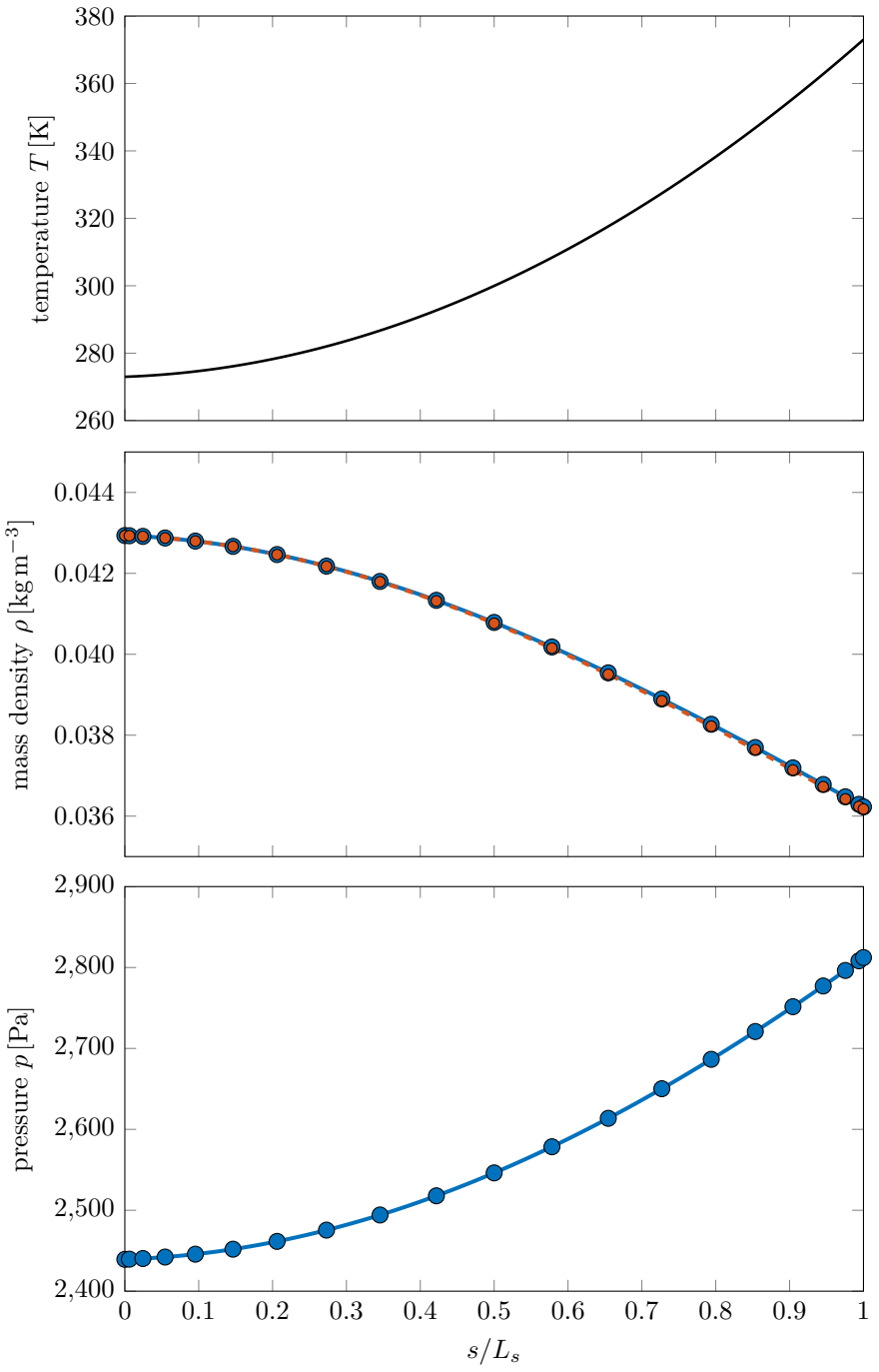

Figure 5.5: Streamwise variation of T (top), ρ (middle) and p (bottom) computed by the steady-IMM for $\Pi = 21$ at the centreline of a converging-diverging channel (● with solid line). The case is repeated for a simple channel (with square cross section $L_x = L_y = 0.5\,\mu\text{m}$). The density variation at the centreline of this simple channel (● with dashed line) is also shown: a small difference is observed. The temperature variation is an input and is shown for reference; a non-linear variation is prescribed.

The local pressure and temperature gradients are then:

$$\frac{\mathrm{d}p}{\mathrm{d}s} = \frac{b}{a}\frac{\mathrm{d}T}{\mathrm{d}s}\ , \tag{5.2}$$

where a and b are non-zero constants. If $k = b/a$ is assumed to have a weak (or no) streamwise dependence, it is possible to integrate this equation to give

$$\Delta\tilde{p} \approx k\Delta T\,, \tag{5.3}$$

where $\Delta\tilde{p}$ is dependent on ΔT, and not the temperature variation. Thus, for a fixed ΔT and $\Delta\tilde{p}$, but a variable temperature distribution, k (which groups macroscopic quantities) must remain constant irrespective of $T(s)$. If k is assumed to represent the average values of viscosity, p, and Kn (as in the analytical slip model of Karniadakis et al. [2005]), then $\Delta\tilde{p}$ should remain approximately constant.

5.3 Optimal cross-sectional geometry

We now consider how the cross-sectional geometry of the capillaries (assumed to be identical) influences performance. The packing of multiple capillaries (as in Knudsen compressors) is also studied. The unsteady-IMM is used to verify the findings.

5.3.1 Theory and implementation

LVDSMC simulations on two-dimensional unstructured grids are performed. Five different cross-sectional geometries are considered: circular, hexagonal, rectangular (2:1), square, and triangular. Attention is restricted to those cross-sectional shapes that are relatively simple to fabricate using conventional micromachining techniques.

The mass flow rate generated by a streamwise pressure gradient and temperature gradient are obtained separately for the cross-sectional geometries listed, as a function of the Kn range of 0.08 to 100. Variable hard sphere air is modelled.

Reduced pressure-driven and thermally-driven mass flow rates are

$$Q_p = \dot{m}_p\left[\Gamma\frac{1}{p}\frac{\mathrm{d}p}{\mathrm{d}s}\right]^{-1}\ ,\ \text{and}\ Q_T = \dot{m}_T\left[\Gamma\frac{1}{T}\frac{\mathrm{d}T}{\mathrm{d}s}\right]^{-1}\ , \tag{5.4}$$

respectively, where $\dot{m}_p$ is the pressure-driven mass flow rate, $\dot{m}_T$ is the thermally-driven mass flow rate, and $\Gamma = A\lambda\rho\sqrt{2RT}$. The ratio of these two variables $\widetilde{Q} = Q_T/Q_p$ is a reflection of the maximum pressure difference ($\Delta\tilde{p}$) attainable, for a given temperature difference. The use of multiple (parallel) capillaries is expected to increase the rate at which Δp is maximised (achieved at the final stationary state

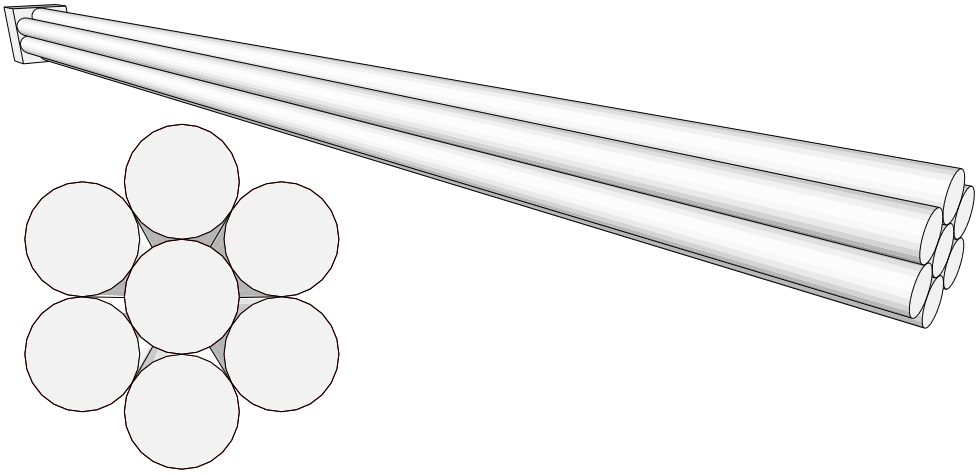

Figure 5.6: Schematic showing a bundle of capillaries with circular cross section in a hexagonal packing arrangement. The cross section of the same array is also shown.

where $\dot{M} = 0$). As will be shown, this rate can be characterised by $\eta\, Q_p$, where η is the packing density of the capillaries. This may be expressed as

$$\eta = \frac{\text{internal cross-sectional area}}{\text{tessellated area}} = \frac{A}{a'}\,. \tag{5.5}$$

Figure 5.6 illustrates the hexagonal packing of seven identical circular capillaries.

Calculation of η is demonstrated for hexagonal and circular cross-sectional geometries (see Fig. 5.7). The area of a regular hexagon is simply

$$A = \frac{3\sqrt{3}}{2}\left(\frac{L}{2}\right)^2\,. \tag{5.6}$$

With reference to Fig. 5.7, the tessellated area of a hexagon is

$$a' = \frac{3\sqrt{3}}{2}d^2\,. \tag{5.7}$$

The inradius r and side length d are

$$r = \frac{\sqrt{3}}{2}\frac{L}{2}\,, \text{ and} \tag{5.8}$$

$$d = \frac{2}{\sqrt{3}}\left(r + \frac{\gamma}{2}\right) = \frac{L}{2} + \frac{\gamma}{\sqrt{3}}\,, \tag{5.9}$$

where γ is the distance between the inner walls of adjacent capillaries (see Fig. 5.7). When the cross section is circular, γ is defined differently, as circles do not tessellate.

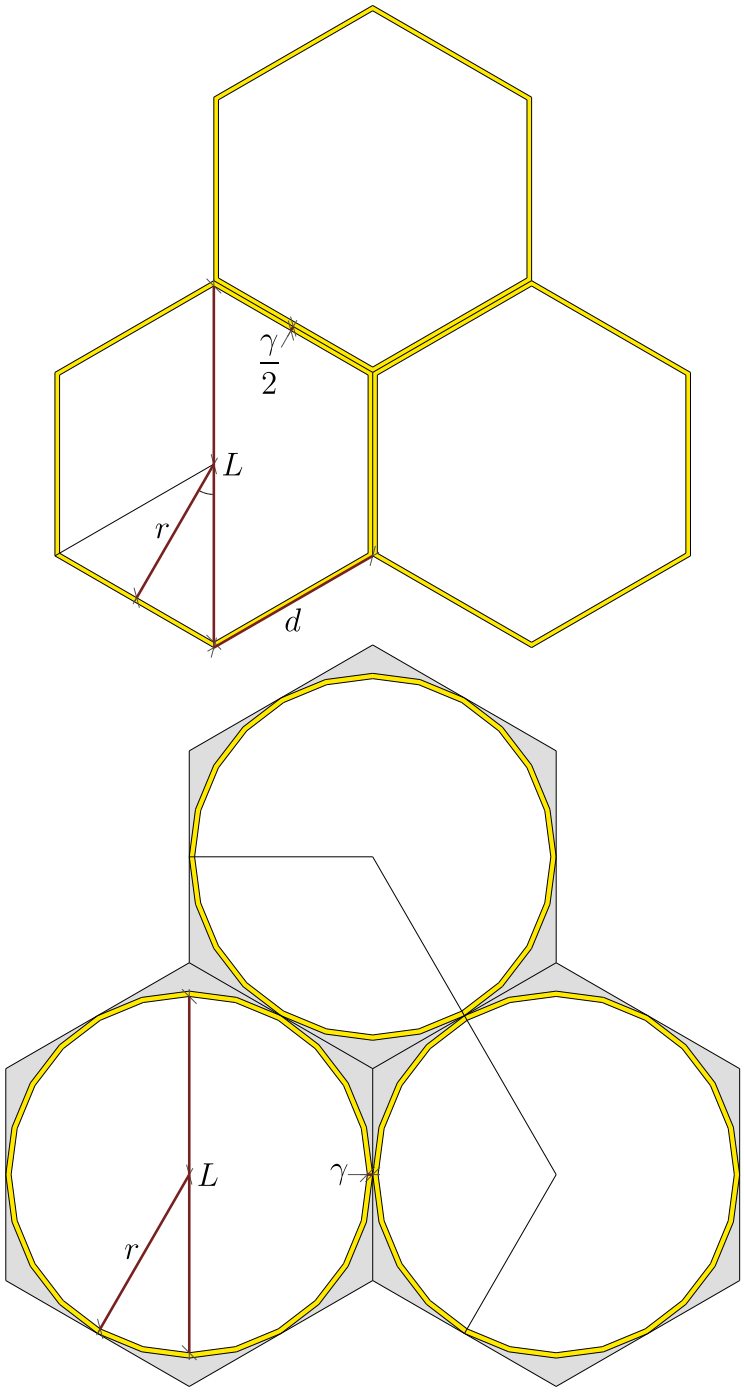

Figure 5.7: Cross section of hexagonal (top) and circular (bottom) capillaries, illustrating packing when $\gamma \neq 0$. Circles are in a hexagonal packing arrangement. The highlighted regions represent the walls (with wall thickness γ) between capillaries.

From this, η is

$$\eta = \frac{A}{a'} = \frac{L^2}{4\left(\frac{L}{2} + \frac{\gamma}{\sqrt{3}}\right)^2} = \frac{1}{\left(1 + \frac{2}{\sqrt{3}}\frac{\mathrm{Kn}}{\upsilon}\right)^2}, \tag{5.10}$$

where the Knudsen number based on wall thickness (γ) is $\upsilon = \lambda/\gamma$, or $\mathrm{Kn}/\upsilon = \gamma/L$. In the case of circular cross-sectional geometries, identical circles are arranged in the densest packing configuration possible. The tessellated area is found by

$$a' = \frac{\sqrt{3}}{2}(L + 2\gamma)^2 = 2\sqrt{3}\left(\frac{L}{2} + \gamma\right)^2. \tag{5.11}$$

From this, η is

$$\eta = \frac{A}{a'} = \frac{\pi L^2}{8\sqrt{3}\left(\frac{L}{2} + \gamma\right)^2} = \frac{\pi}{2\sqrt{3}\left(1 + 2\frac{\mathrm{Kn}}{\upsilon}\right)^2}. \tag{5.12}$$

The maximum value of η, which is recovered when $\upsilon = \infty$, is relatively low at $\Pi/(2\sqrt{3}) \approx 0.9069$. Therefore, a bundle of capillaries with circular cross section do not pack efficiently, resulting in a sub-optimal configuration.

For the other cross-sectional shapes considered, the derivation of η can be found in Appendix C. The packing density of rectangular cross sections is

$$\eta = \frac{1}{1 + 2\left(\frac{\mathrm{Kn}}{\upsilon}\right)^2 + 3\frac{\mathrm{Kn}}{\upsilon}}. \tag{5.13}$$

The packing density of square cross sections is

$$\eta = \frac{1}{\left(1 + \frac{\mathrm{Kn}}{\upsilon}\right)^2}. \tag{5.14}$$

The packing density of triangular cross sections is

$$\eta = \frac{1}{\left(1 + \frac{\mathrm{Kn}}{2\upsilon} + \frac{\mathrm{Kn}}{\sqrt{3}\upsilon}\right)^2}. \tag{5.15}$$

The value of Kn is determined by spline interpolation on $\widetilde{Q} = f(\mathrm{Kn})$. The results in the following section are obtained for the query points $\widetilde{Q} = 0.15$, 0.25, and 0.35. The characteristic length L is then obtained for an average pressure $\bar{p}$.

The area A is calculated based on L, and the number of capillaries is

$$N_{\texttt{cha.}} = \frac{A'\eta}{A}\,, \tag{5.16}$$

where A' is the total cross-sectional area that a bundle of capillaries can occupy.

The total pressure-driven mass flow rate $\dot{M}_p$ and thermally-driven mass flow rate $\dot{M}_T$ of an ideal gas (through $N_{\texttt{cha.}}$ capillaries) are related by mass conservation:

$$\frac{V_c}{RT}\frac{\mathrm{d}p_c}{\mathrm{d}t_3} = \dot{M}_p - \dot{M}_T = -\frac{V_h}{RT}\frac{\mathrm{d}p_h}{\mathrm{d}t_3}\ . \tag{5.17}$$

The above can be expressed separately as

$$\frac{\mathrm{d}p_c}{\mathrm{d}t_3} = \frac{RT}{V_c}\left(\dot{m}_p - \dot{m}_T\right) N_{\texttt{cha.}}\,, \tag{5.18}$$

$$-\frac{\mathrm{d}p_h}{\mathrm{d}t_3} = \frac{RT}{V_h}\left(\dot{m}_p - \dot{m}_T\right) N_{\texttt{cha.}}\,. \tag{5.19}$$

If $\Delta p = p_h - p_c$, then

$$\frac{\mathrm{d}\left(\Delta p\right)}{\mathrm{d}t_3} = -RT\left(\frac{1}{V_c} + \frac{1}{V_h}\right)\left(\dot{m}_p - \dot{m}_T\right) N_{\texttt{cha.}}\,, \tag{5.20}$$

which, by equation (5.4), can be expressed as

$$\frac{\mathrm{d}\left(\Delta p\right)}{\mathrm{d}t_3} = -RT\left(\frac{1}{V_c} + \frac{1}{V_h}\right)\left(-\dot{m}_T + \Gamma Q_p \frac{1}{\bar{p}}\frac{\Delta p}{L_s}\right) N_{\texttt{cha.}}\,, \tag{5.21}$$

where $\bar{p}$ is the average pressure. Assuming the form

$$\Delta p\left(t_3\right) = -\Delta\tilde{p}\left[\exp\left(-\frac{t_3}{\widetilde{\tau}}\right) - 1\right]\,, \tag{5.22}$$

where $\Delta\tilde{p}$ is the stationary pressure difference, the characteristic time (constant) is

$$\frac{1}{\widetilde{\tau}} \propto A N_{\texttt{cha.}} Q_p\,, \tag{5.23}$$

found by expressing $\dot{m}_T$ (in equation (5.21)) in terms of $\Delta\tilde{p}$ when $\dot{m}_T = \dot{m}_p$ (when $\mathrm{d}(\Delta p)/\,\mathrm{d}t_3 = 0$). Equations (5.21) and (5.22) are equated to give equation (5.23), which is sufficient as the relative performance of each cross-sectional shape is of interest. Furthermore, because A' is fixed, and according to (5.16), the above is

$$\frac{1}{\widetilde{\tau}} \propto \eta\, Q_p\,. \tag{5.24}$$

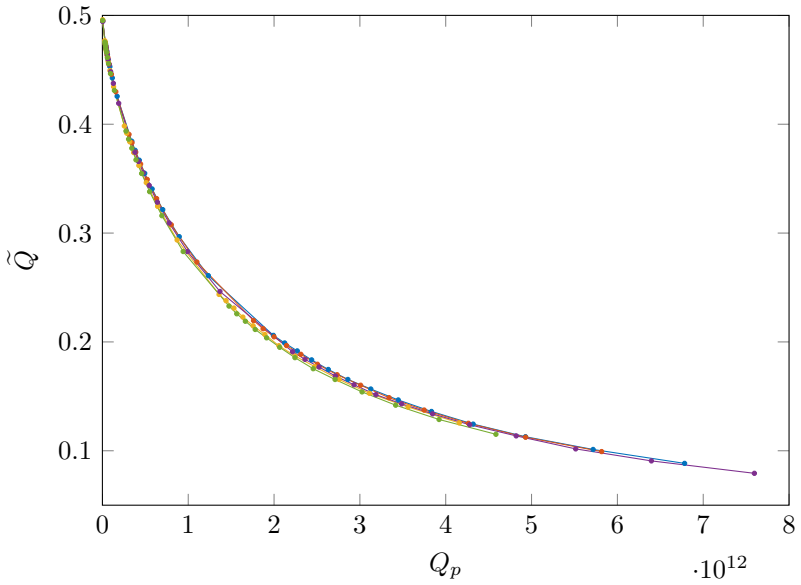

Figure 5.8: The ratio of the reduced mass flow rates $\widetilde{Q} = Q_T/Q_p$ against Q_p for various cross-sectional shapes: circular (—•—); hexagonal (—•—); rectangular (—•—); square (—•—); triangular(—•—). The characteristic length is $L = 1\,\mu\text{m}$ for all cases.

It is possible to find $\widetilde{\tau}$ by fitting the model equation (5.22) to unsteady-IMM results. In the following section, this is done to verify a steady-state analysis demonstrating the influence of the cross-sectional shape (of capillaries) on performance.

5.3.2 Results

The reader is reminded that the maximum pressure difference $\Delta\tilde{p}$ per unit temperature gradient (a measure of steady-state performance) increases with $\widetilde{Q}$ (see Fig. 5.8). Maximising Q_p will reduce the time required to achieve the final stationary state. The best performance is provided by those cross-sectional shapes that maximise both $\widetilde{Q}$ and $\eta\, Q_p$, which, as shown in the preceding section, is inversely proportional to the characteristic time $\widetilde{\tau}$. The characteristic length $L = 1\,\mu\text{m}$ is set for all cases, which implies that the area A of the simulated geometries is variable. Figures 5.9a and 5.9b show $\widetilde{Q} = Q_T/Q_p$ against $\eta\, Q_p$ for the ideal case $\upsilon = \infty$, and for the realistic case $\upsilon = 0.5$, respectively. By comparing Figs. 5.8 and 5.9a, it is clear that (for $\upsilon = \infty$) $\eta \neq 1$ for circular cross sections; all other cross-sectional geometries tessellate (and thus $\eta = 1$). Because the perimeter-area ratio is different for each cross-sectional shape, the curves in Fig. 5.8 do not overlap. If the influence of the packing density is realised (Figs. 5.9a and 5.9b), a bundle of capillaries with circular cross section provides relatively poor performance (despite the low perimeter-area ratio of circles being favourable).

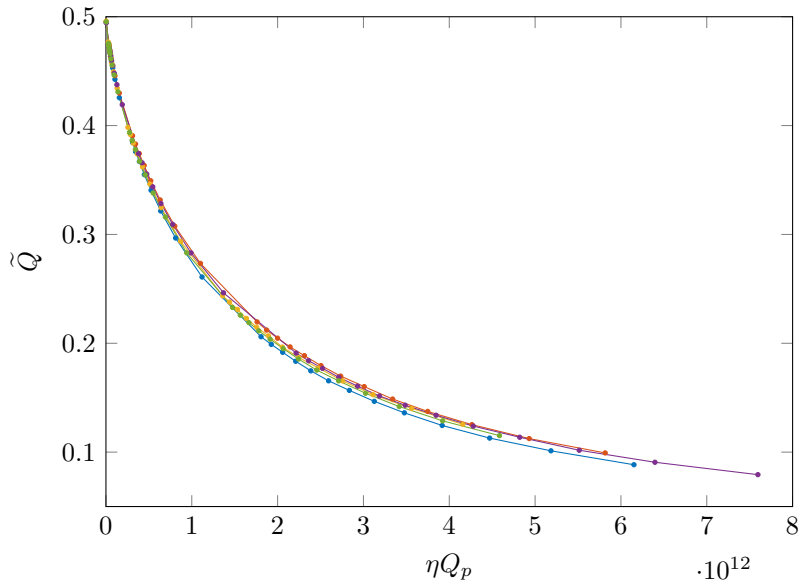

(a) $\upsilon = \infty$

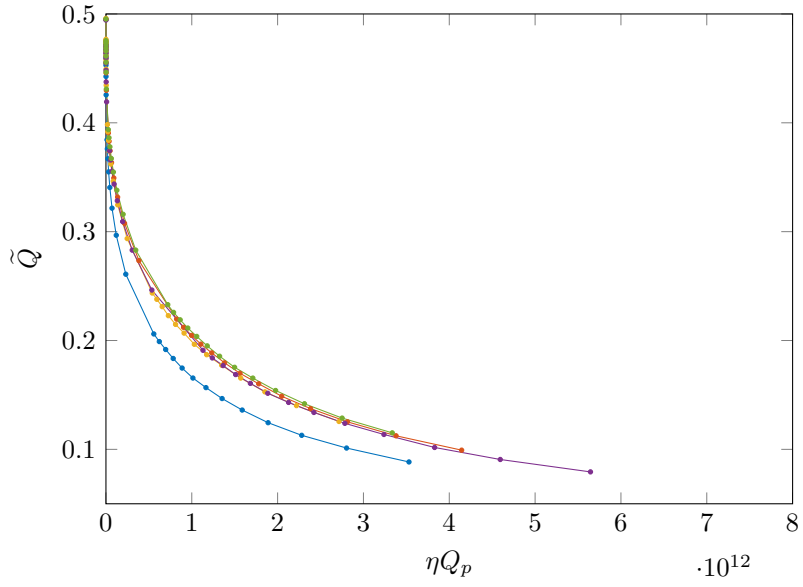

(b) $\upsilon = 0.5$

Figure 5.9: The ratio of the reduced mass flow rates $\widetilde{Q} = Q_T/Q_p$ against $\eta\, Q_p$ for various cross-sectional shapes: circular (—•—); hexagonal (—•—); rectangular (—•—); square (—•—); triangular (—•—). The packing density η is a function of Kn and υ.

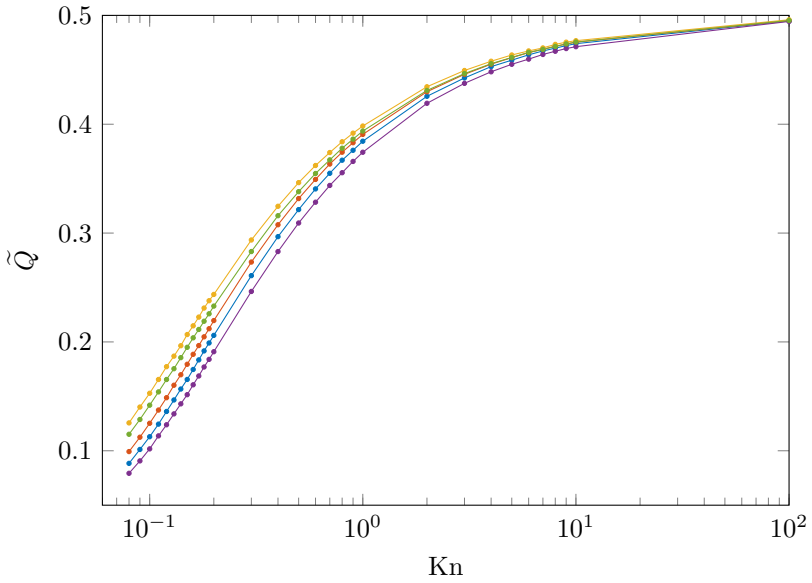

Figure 5.10: The ratio of the reduced mass flow rates $\widetilde{Q} = Q_T/Q_p$ against Kn for various cross-sectional shapes: circular (—•—); hexagonal (—•—); rectangular (—•—); square (—•—); triangular (—•—). The characteristic length is $L = 1\,\mu\text{m}$ for all cases.

As $\upsilon \to 0$ (the Knudsen number defined by the wall thickness γ), the packing density $\eta \to 0$. For a fixed value of A', circular cross sections are the least desirable for all values of υ. Furthermore, it is worth noting that as $\text{Kn} \to \infty$, $\widetilde{Q} \to 0.5$ holds irrespective of the cross-sectional shape [Sone, 2007]. The same is observed in Sharipov [1999]; Doi [2010] for rectangular cross sections.

The unsteady-IMM is used to verify the above steady-state analysis. Two values of υ are considered: 0.5, and ∞. The query points, at which values of Kn are found by spline interpolation on the data presented in Fig. 5.10, are $\widetilde{Q} = 0.15$, 0.25, and 0.35. These values are independent of υ. Input variables are derived from the interpolated value of Kn, and include the number of identical capillaries $N_{\texttt{cha.}}$, and the characteristic length L (and hence cross-sectional area A) of each capillary. With λ treated as an input, L can be found by equation (1.1). The number of capillaries is found by equation (5.16), where $A' = 0.0001\,\text{m}^2$ is fixed throughout. The packing density η is a function of the interpolated value of Kn and υ. All other parameters are constant. The initial pressure is $p_{\text{int.}} = 100\,\text{Pa}$ in both reservoirs, the volumes of which are $V_c = V_h = 0.0015\,\text{m}^3$. A linear temperature variation is prescribed, with the average temperature $\overline{T} = 323\,\text{K}$. The streamwise length of the capillary is $L_s = 0.05\,\text{m}$, and the number of subdomains is $\Pi = 8$ for all computations. Note, thermally-driven and pressure-driven flows develop simultaneously.

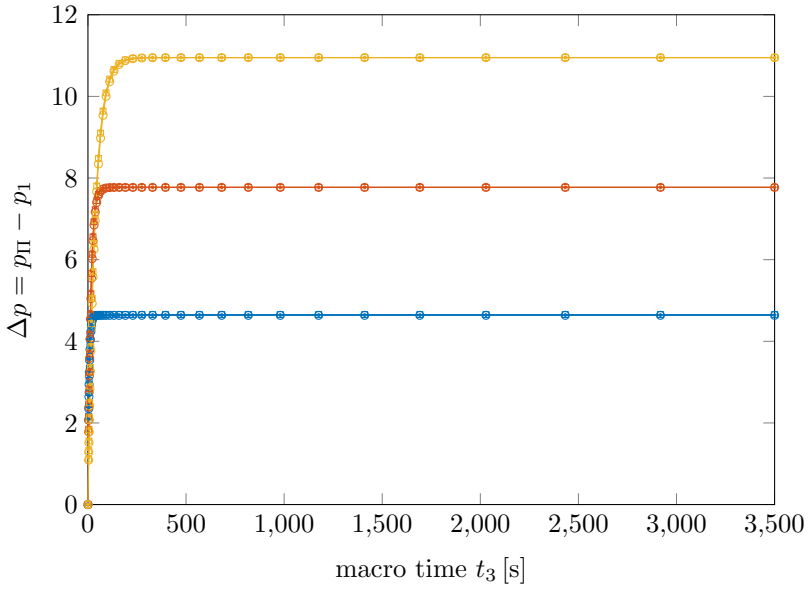

(a) $v = \infty$

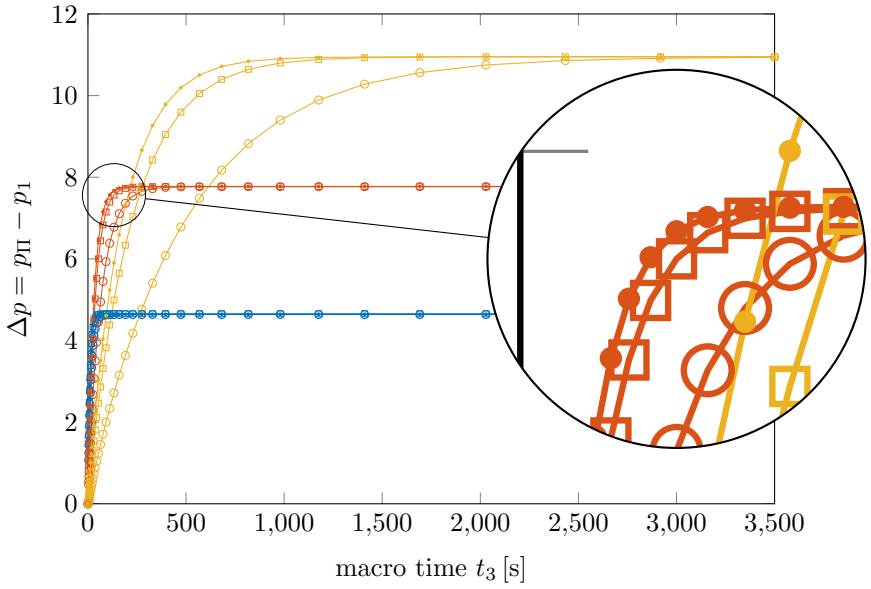

(b) $v = 0.5$

Figure 5.11: Time evolution of Δp for two values of v and $\widetilde{Q} = 1.5$ (circular (—○—); square (—□—); triangular (—•—)), $\widetilde{Q} = 2.5$ (circular (—○—); square (—□—); triangular (—•—)), and $\widetilde{Q} = 3.5$ (circular (—○—); square (—□—); triangular (—•—).

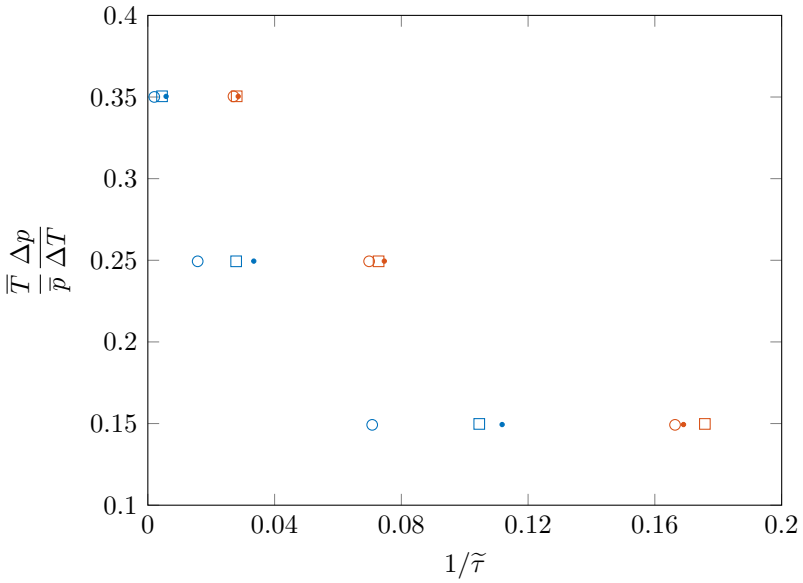

Figure 5.12: The relative performance ($\widetilde{Q}$ against $1/\widetilde{\tau}$) of circular (○); square (□); and triangular (•) cross sections for $\upsilon = \infty$ (red markers), and $\upsilon = 0.5$ (blue markers).

The time evolution of the pressure difference Δp computed by the unsteady-IMM is shown in Fig. 5.11. Only circular, square, and triangular cross-sectional shapes are considered. As expected, the relative performance is essentially unaffected by the cross-sectional geometry when $\upsilon = \infty$ (see Fig. 5.11a). When the wall thickness is vanishingly small ($\gamma \to 0$), it is possible to achieve the desired (maximum) pressure difference $\Delta\tilde{p}$ (in the stationary state where $\dot{M} = 0$) within approximately the same time, irrespective of the cross-sectional shape. The characteristic time is extracted by fitting equation (5.22) to the results presented in Fig. 5.11. Figure 5.12 shows the values of $\widetilde{\tau}^{-1}$ for $\widetilde{Q} = 0.15$, 0.25, and 0.35. The results are consistent with equation (5.23). Because the case where $\upsilon = \infty$ is not realistic (the gap size γ cannot physical be zero) the more realistic case where $\upsilon = 0.5$ (see Fig. 5.11b) is also considered. Since significantly fewer circular capillaries can be packed under such conditions, the development time is greater. In Fig. 5.11b, circular cross sections are shown to be sub-optimal (due to the lack of tessellation). Triangular cross sections offer the best performance. In the case of square cross sections, the development time is slightly greater, relative to triangular cross sections. Again, this holds for all values of $\widetilde{Q}$ considered. Interestingly, the percentage difference between $1/\widetilde{\tau}$ of triangular and square cross sections increases with $\widetilde{Q}$. When $\widetilde{Q} = 0.35$, 0.25, and 0.15, the percentage difference is 25 %, 18 %, 6.7 %, respectively; triangular cross sections become increasingly favourable as $\widetilde{Q} \to 0.5$.

		$\widetilde{Q}$		
	υ	0.15	0.25	0.35
circular	0.5	0.3860	0.2043	0.0679
	∞	0.9069	0.9069	0.9069
square	0.5	0.5950	0.3827	0.1597
	∞	1	1	1
triangular	0.5	0.6614	0.4480	0.2020
	∞	1	1	1

Table 5.1: The packing density η for circular, square, and triangular cross sections, as a function of $\upsilon\,(=\infty\,,0.5)$, and $\widetilde{Q}\,(=0.35\,,0.25\,,0.15)$.

These observations can be attributed two factors, the primary of which is the packing density η (smallest for circular cross sections due to the lack of tessellation). The secondary factor is the perimeter-area ratio (where a small value is favourable).

When $\gamma = 0$, i.e. when the wall thickness is zero ($\upsilon = \infty$), square and triangular cross sections tessellate with $\eta = 1$. The performance of square cross sections is slightly superior in the case of $\widetilde{Q} = 0.15$ due to the lower perimeter-area ratio of squares. However, as observed in Fig. 5.12, when $\upsilon = \infty$, triangular cross sections become increasingly favourable with increasing $\widetilde{Q}$. Because $\eta = 1$ for both square and triangular cross sections, this suggests that a third, less obvious factor may have an influence, since the perimeter-area ratio of triangles is highest. Assuming that this observation is not the result of numerical inaccuracies, further work should attempt to identify this third factor, if it exists. In the case of circular cross sections, performance is consistently poor due to the lack of tessellation.

When $\upsilon = 0.5$, triangular cross sections exhibit a higher packing density (the dominant factor) than that of square cross sections (as seen in Table 5.1), and thus provide better performance. This is likely to be the case for most non-ideal packing configurations. Further work should involve a thorough investigation of this result, and include the characterisation of hexagonal cross sections also.

Chapter 6

Conclusion

In this thesis, an efficient and highly accurate multiscale method has been developed for the accelerated solution of problems involving low-speed rarefied gas flows in high-aspect-ratio (i.e. are extremely long, relative to their cross section) conduits. The high aspect ratio creates a formidable multiscale problem: processes need to be resolved occurring over the smallest characteristic scale of the geometry (e.g. the height of the conduit), as well as over the largest characteristic scale of the geometry (e.g. the streamwise length of the conduit), simultaneously. The method, known as the internal-flow multiscale method (IMM) for gas flows (which is not be confused with that of Borg et al. [2013a] for dense-fluid flows), will (generally) dramatically outperform other methods for the simulation of rarefied gases. It allows for the solution of otherwise computationally intractable problems, and has been shown to provide performance improvements of orders of magnitude (relative to full molecular treatment). The applicability of the method is clearly defined and simply requires that a degree of spatial- or temporal-scale separation exists.

In addition to being highly efficient, the IMM for gas flows (which will be referred to simply as the IMM in this chapter) can treat multi-dimensional problems involving fluid compressibility, non-isothermal conditions, and transient flows, and, due to its use of pseudospectral methods, boasts excellent convergence characteristics and accuracy. It allows for the imposition of a variety of boundary conditions, and supports body-force-driven, pressure-driven, thermally-driven, and shear-driven flows. Molecular resolution is provided by the low-variance deviational simulation Monte Carlo (LVDSMC) method which is able to treat low-signal flows.

The IMM is designed to be general, and is most suitable when the problem is relatively complex with multiple degrees of freedom. Such problems (i.e. when the pre-calculation of data, for interpolation at runtime, is too computationally intensive) cannot be solved efficiently using a lookup table approach [Sharipov, 1999];

the tractability of this approach scales exponentially with the degrees of freedom.

The ease with which problems can be posed by the IMM is an important benefit; the complications associated with the use of pressure boundary conditions by particle-based methods are avoided. For example, using the direct simulation Monte Carlo (DSMC) method to simulate low-signal pressure-driven flows (for verification purposes) proved to be unreliable. Also, it essential that care is taken when initialising such problems, e.g. the sudden application of a pressure gradient (by pressure boundary conditions) in high-aspect-ratio conduits may produce non-physical behaviour. The IMM greatly simplified the set-up of these flow configurations, and does not require the user to carefully impose initial conditions (especially in the case of the steady-IMM). Furthermore, because the DSMC method is inherently unsteady (time marching), its efficiency, compared to that of the IMM, suffers when simulating steady problems with lengthy development times.

The unsteady-IMM has been validated by comparison with the experimental data of Rojas-Cárdenas et al. [2013]. In all cases, excellent agreement is observed, providing confidence that the IMM may be used to inform the design of thermal-transpiration compressors. In addition, the unsteady-IMM offers a speed-up (relative to a simulation where scale separation is not exploited) of at least five orders of magnitude: a saving that allows for the solution of problems that would otherwise not be possible using a non-hybrid simulation by the (particle-based) micro solver.

The efficiency and accuracy of the (steady- and unsteady-)IMM allows for the study of thermal-transpiration compressors (and implicitly Knudsen compressors), solid state devices that rely on the phenomenon of thermal transpiration to provide compression or pumping. This rarefied gas effect, like much of the science at small scales, presents many opportunities for the development of future technologies. For example, thermal transpiration has been discussed as a mechanism by which satellite-on-a-chip attitude and position can be controlled in low Earth orbit [White et al., 2013]. It has also been proposed as a means to separate a gaseous mixture [Takata et al., 2007]. The analysis presented in this thesis suggests that the performance of thermal-transpiration compressors is insensitive to some aspects of capillary design. Specifically, (moderate) modifications to the streamwise temperature gradient and cross-sectional geometry produced no change in the maximum pressure difference attainable (in the stationary state with zero net mass flow rate). This robustness is highly desirable, and may allow for increased geometric tolerances in manufacturing without adversely affecting function.

For the purposes of engineering design, the transient behaviour of thermal-transpiration (and Knudsen) compressors has been studied by applying the unsteady-

IMM, and an implementation of the LVDSMC method that allows for the simulation of arbitrary two-dimensional geometries on unstructured meshes. The development time required to maximise the pressure difference was characterised as a function of the number of (parallel) capillaries connecting two reservoirs, and the wall thickness between adjacent capillaries. It was found that the packing of these capillaries is the dominant factor in determining the performance of thermal-transpiration compressors (that make use of a bundle of capillaries). The perimeter-area ratio of the cross section of these (identical) capillaries is of secondary importance. In addition, for a Knudsen number (based on wall thickness) of 0.5, triangular cross sections provide the best overall performance (in terms of maximum pressure difference and shortest development time), compared to circular and square cross sections.

6.1 Future work

Following the work presented in this thesis, future research related to the use of the IMM to study thermal transpiration should involve:

- the investigate of the influence, if any, of the tangential momentum accommodation coefficient on thermal-transpiration compressor performance.
- the study of streamwise modifications in temperature and cross-sectional geometry as factors that affect the development time of the pressure-driven flow that opposes the thermally-driven flow in thermal-transpiration compressors.
- the study of thermal transpiration for fluid-based, chip-level cooling of microprocessors. Although, active microchannel cooling solutions have already been proposed [Koo et al., 2005; Kenny et al., 2006], the passive cooling of microprocessors using thermal transpiration has yet to be considered in literature.

In addition, recent work by de Beule et al. [2014] suggests that, at an average ambient pressure of 600 Pa, gas flow through the porous surface of Mars by thermal transpiration has an influence on the gas cycle and soil atmosphere interaction on Mars. With modifications to the IMM to support multispecies flows, this natural thermal-transpiration pump can be investigated numerically. Furthermore, on the subject of pumping, future research may involve the use of the IMM to study accommodation pumping [Young et al., 2005] in small-scale devices.

The steady-IMM has been used to study rarefied lubrication in a micro-gas journal bearing. Because the thickness (y-dimension) of lubricating gas films tends to be extremely small compared to the length scales in the lateral dimensions (x- and s-dimensions), the IMM is exceptionally well-suited to treat such problems.

Predicting the pressure distribution in rarefied lubrication films, which the IMM can efficiently compute, is necessary to determine its load-carrying capacity. Future work related to the use of the IMM to study rarefied lubrication should involve:

- the investigation of unsteady low-speed rarefied Taylor-Couette flows.
- the study of the phenomenon of velocity inversion [Einzel et al., 1990]. The flexibility of the IMM allows for the efficient study of this non-intuitive behaviour. The tangential momentum accommodation coefficient has been found to influence velocity inversion [Yuhong et al., 2005], and as such it would beneficial to gain additional insight into this behaviour using the IMM.
- the study of the lubricating gas layer (of micrometer thickness) that forms between an impacting droplet and a surface [Kolinski et al., 2012, 2014; de Ruiter et al., 2015]. Understanding drop impact behaviour is critical to a variety of processes, such as anti-icing, spray coating, and inkjet printing. The gas film, the aspect ratio of which is exceedingly large, remains intact if the impact speed is less than $0.5\,\mathrm{m\,s^{-1}}$ [de Ruiter et al., 2015].

In terms of general development, the IMM for gas flows should be extended to support multispecies flows (which are relevant to mixing applications) and chemistry modelling (for the simulation of micro reactors). Further extension of the method should incorporate machine learning approaches (e.g. neural networks or Gaussian processes) to accurately predict the output of micro-solver instances, limiting the invocation of the micro solver and increasing efficiency. In addition, the IMM should accommodate flow regions where scale separation cannot be exploited. Such regions must be fully described by the micro solver and are coupled to the scale-separated regions, as detailed in Borg et al. [2013b]; Stephenson et al. [2014].

Appendix A

Unstructured LVDSMC

The implementation and verified of a two-dimensional unstructured-mesh based low-variance deviational simulation Monte Carlo (LVDSMC) flow solver is presented. This implementation (referred to as the ULVDSMC method) provides much greater geometric flexibility. All preprocessing, including mesh generation, is currently handled by a standalone method: DistMesh [Persson, 2004]. It is important that the mesh is as uniform as possible. The degree of mesh refinement/smoothing, which is the responsibility of the user, will dictate mesh uniformity.

The main modifications to the LVDSMC source code are contained within the `intersection` and `locate` subroutines, since it is not possible to express an unstructured mesh simply as a two-dimensional array in computer memory. The Barycentric Technique [Ericson, 2005] can be used to test containment of a point P in a triangle ABC, i.e. it provides efficient point-in-triangle testing. For efficient simulation, the triangle ABC should not be found by bruteforce; it is computationally expensive and inefficient to simply consider every triangular element (cell) when indexing P within the unstructured mesh of cells. An efficient data structure, and an associated procedure for particle-in-cell location, are required. In terms of computational performance, structure is beneficial. Locating P within a structured (regular) mesh is a trivial task requiring little computational effort. To drastically reduce the number of unstructured cells that are tested, the cells of the unstructured mesh are sorted into (structured) super-cells. This 'binning' is a preprocessing procedure, and is only performed once. If a particle leaves the simulation domain, it is necessary to calculate the line-ray intersection of the boundary edge of the cell the particle escaped from and the particle's trajectory. It is from this intersection point that the particle is reintroduced into the domain. To avoid the need to test every boundary edge, the nearest edge to any super-cell is recorded during preprocessing. In what follows, the ULVDSMC implementation is verified.

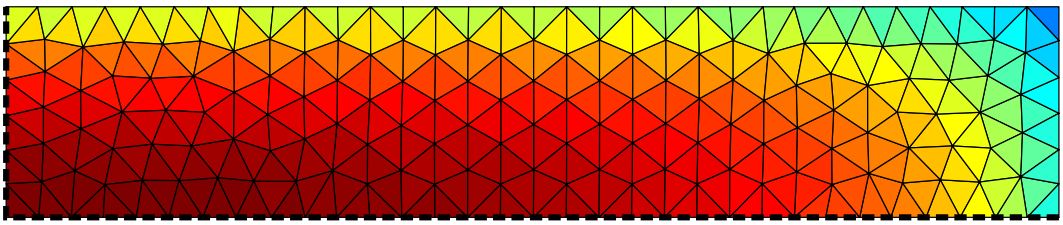

(a) Rectangular geometry with $l \approx 0.09$.

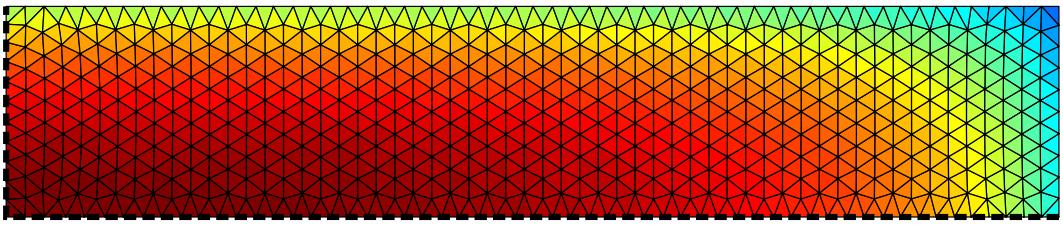

(b) Rectangular geometry with $l \approx 0.05$.

Figure A.1: Velocity profile $w(x, y)$ for rectangular cross section on approximately uniform unstructured meshes of variable resolution. For both simulations, the Knudsen number is $\mathrm{Kn} = 0.5$ and the viscosity index is $\omega = 0.5$. Owing to symmetries in the x- and y-directions, only a quarter of the cross section is simulated.

To verify the ULVDSMC method, the computed dimensionless mass flow rate is compared to that reported in literature. The following cases are considered:

1. a unit square on an approximately uniform unstructured mesh (Fig. A.2b);
2. a rectangle on an approximately uniform unstructured mesh:
   (a) edge length $l \approx 0.09$, $\mathrm{Kn} = 0.5$ (Fig. A.1a);
   (b) edge length $l \approx 0.05$, $\mathrm{Kn} = 0.5$ (Fig. A.1b);
3. a unit circle on an approximately uniform unstructured mesh:
   (a) edge length $l \approx 0.018$, $\mathrm{Kn} = 1$ (Fig. A.2a);
   (b) edge length $l \approx 0.011$, $\mathrm{Kn} = 10$ (Fig. A.3);

For a conduit of infinite streamwise length and rectangular (aspect ratio of 5) cross section, in which we model a hard sphere gas (viscosity index $\omega = 0.5$) with $\mathrm{Kn} = 0.5$, the dimensionless mass flow rate calculated on an unstructured mesh ($l \approx 0.09$, see Fig. A.1a) by the ULVDSMC method is $G_{\texttt{ULV}} = 0.673$. For comparison, the dimensionless mass flow rate reported by Doi [2010] is $G_{\texttt{Doi}} = 0.676$ (to the reported accuracy). A small percentage error of 0.49 % is observed. If we repeat the simulation with a finer mesh ($l \approx 0.05$, see Fig. A.1b), $G_{\texttt{ULV}} = 0.674$,

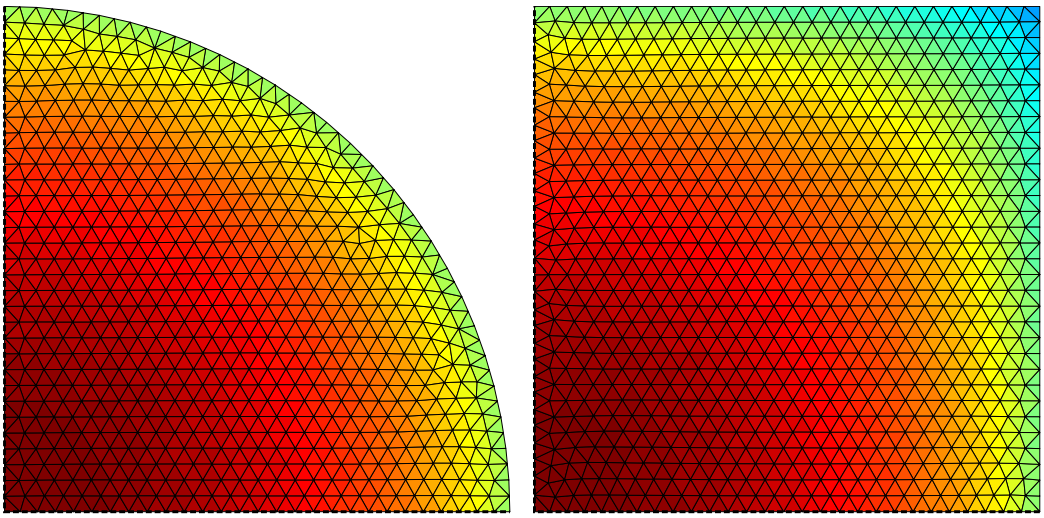

(a) Circular cross section with Kn = 1.0. (b) Square cross section with Kn = 0.5.

Figure A.2: Velocity profile $w(x, y)$ for square and circular cross sections on approximately uniform unstructured meshes with $l \approx 0.018$. Owing to symmetries in the x- and y-directions, only a quarter of the cross section is simulated.

which gives a percentage error of 0.26 %. As expected, the error is reduced; a finer mesh will give better agreement, as with the DSMC method.

For a unit circle (see Fig. A.2a) the dimensionless mass flow rate on an unstructured mesh $G_{\texttt{ULV}} = 1.377$ for Kn = 1 ($R = 0.451$, as defined by Loyalka and Hamoodi [1990]). This result agree to within 0.15 % (for $G_{\texttt{Loy.}} = 1.379$) of that reported in Loyalka and Hamoodi [1990]. If we repeat this simulation with a finer mesh ($l \approx 0.011$), as shown in Fig. A.3, and a higher Knudsen number Kn = 10 ($R = 0.0451$), the dimensionless mass flow rate on an unstructured mesh is $G_{\texttt{ULV}} = 1.4281$. This result agrees to within 0.0048 % (for $G_{\texttt{Loy.}} = 1.43$) of that reported in Loyalka and Hamoodi [1990]. The execution time is used to (approximately) assess the computational efficiency of the ULVDSMC. For the case of a circular cross section (on the mesh shown in Fig. A.3), where the total number of time steps, Knudsen number, scaled pressure gradient, and deperature from equilibrium are 102500, Kn = 10, $\phi_p = 1$, $\epsilon = 0.0001$, respectively, the execution time was 0.49 h.

For a unit square (on the mesh shown in Fig. A.2b) the dimensionless mass flow rate on an unstructured mesh $G_{\texttt{ULV}} = 0.39627$ for Kn = 0.5. The results agree with those of Doi [2010] ($G_{\texttt{Doi}} = 0.396$), to the reported accuracy.

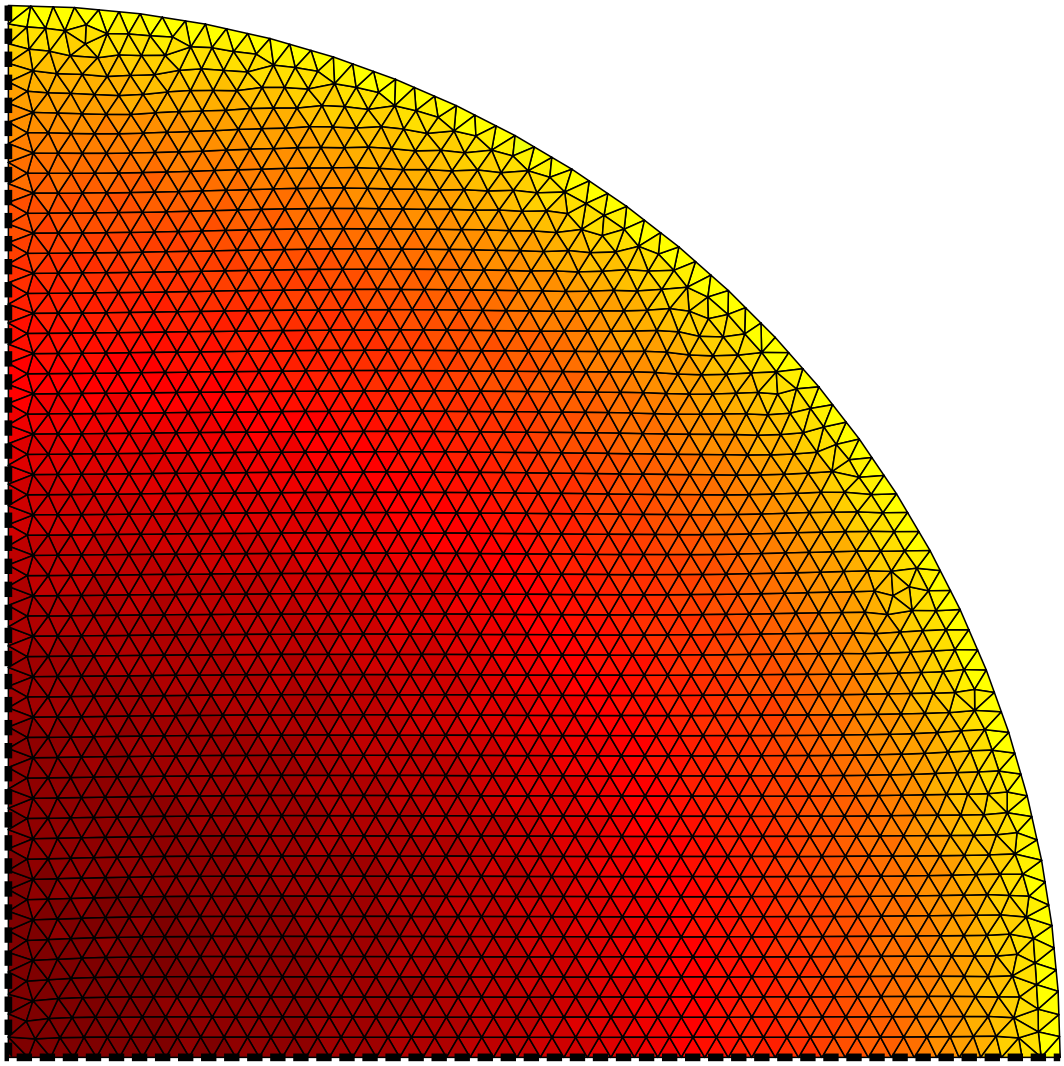

Figure A.3: Velocity profile $w(x, y)$ for circular cross section on an approximately uniform unstructured mesh with $l \approx 0.011$ and $\mathrm{Kn} = 10$. Owing to symmetries in the x- and y-directions, only a quarter of the cross section is simulated.

Appendix B

Derivation of τ_k

B.1 τ_1 – the characteristic micro time scale

We can obtain τ_1 simply by dimensional analysis. The kinematic viscosity

$$\nu = \frac{\mu}{\rho}\,, \tag{B.1}$$

where μ is the dynamic viscosity, and ρ is the mass density. With units of $\mathrm{m}^2\,\mathrm{s}^{-1}$, we multiply the kinematic viscosity by the square of the characteristic length scale, which we take to be the radius of the channel. This gives

$$\tau_1^{-1} = \frac{\bar{\mu}}{\bar{\rho} r^2}\,, \tag{B.2}$$

where $\bar{\mu}$ and $\bar{\rho}$ are the average dynamic viscosity and mass density.

B.2 τ_2 – the characteristic meso time scale

We can obtain τ_2 from mass conservation and by assuming an ideal gas:

$$\frac{\partial p}{\partial t} = -\frac{RT}{\pi r^2}\frac{\partial \dot{m}}{\partial s}\,. \tag{B.3}$$

If we assume a Hagen-Poiseuille flow in the channel:

$$\frac{\mathrm{d}p}{\mathrm{d}s} = \frac{8\mu\dot{m}}{\rho\pi r^4}\,. \tag{B.4}$$

Rearrange the above and find the spatial derivative of mass flow rate:

$$\frac{\mathrm{d}\dot{m}}{\mathrm{d}s} = \frac{\mathrm{d}^2 p}{\mathrm{d}s^2}\frac{\rho\pi r^4}{8\mu}\,. \tag{B.5}$$

We may then combine equations (B.3) and (B.5) to give

$$\frac{\mathrm{d}p}{\mathrm{d}t} = -\frac{RT}{\pi r^2}\frac{\mathrm{d}^2 p}{\mathrm{d}s^2}\frac{\rho\pi r^4}{8\mu}\,. \tag{B.6}$$

If we assume the form

$$\Delta p\,(t_2) = \exp\left(\beta x\right)\exp\left(-\widetilde{\tau}_2 t_2\right), \tag{B.7}$$

where $\beta = L_s^{-1}$, the characteristic time constant is

$$\widetilde{\tau}_2 = -\beta^2 RT\frac{\rho r^2}{8\mu}\,, \tag{B.8}$$

and since we are only interested in an order approximation:

$$\tau_2 = \frac{\bar{\mu}L_s^2}{\bar{p}r^2}\,. \tag{B.9}$$

B.3 τ_3 – the characteristic macro time scale

We can obtain τ_3 by assuming a Hagen-Poiseuille flow in the channel:

$$\Delta p = \frac{8\mu L_s \dot{m}}{\rho\pi r^4}\,. \tag{B.10}$$

The temporal variation of the pressure difference is

$$\frac{\mathrm{d}\left(\Delta p\right)}{\mathrm{d}t_3} = -\frac{RT}{V}\dot{m}\,, \tag{B.11}$$

$$= -\frac{RT}{V}\frac{\Delta p\rho\pi r^4}{8\mu L_s}\,. \tag{B.12}$$

If we assume the form

$$\Delta p\,(t_3) = \Delta\widetilde{p}\,\exp\left(-\widetilde{\tau}_3 t_3\right), \tag{B.13}$$

where $\Delta\widetilde{p}$ is the stationary pressure difference, the characteristic time constant is

$$\widetilde{\tau}_3 = -\frac{RT}{V}\frac{\rho\pi r^4}{8\mu L_s}\,, \tag{B.14}$$

and since we are only interested in an order approximation:

$$\tau_3 = \frac{\bar{\mu}L_s V}{\bar{p}r^4}\,. \tag{B.15}$$

Appendix C

Derivation of η

The derivation of formulations for the packing density η, where

$$\eta = \frac{\text{internal cross-sectional area}}{\text{tessellated area}} = \frac{A}{a'}\,, \tag{C.1}$$

is presented here. The packing density is derived for rectangular, square, and triangular cross sections. The wall thickness (between adjacent channels) γ is as defined for hexagonal cross sections in Chapter 5. The definition of γ is different in the case of circular cross sections, since circles do not tesselate.

C.1 Rectangular cross sections

The internal cross-sectional area A of a rectangle (2:1) is expressed as

$$A = \frac{L^2}{2}\,. \tag{C.2}$$

L is the length of the largest edge (parallel to the y-axis). The tessellated area is

$$a' = (L+\gamma)\left(\frac{L}{2}+\gamma\right)\,, \tag{C.3}$$

$$a' = \frac{L^2}{2} + \gamma^2 + 3\frac{L}{2}\gamma\,, \tag{C.4}$$

where γ is the wall thickness. Therefore, η is

$$\eta_{\texttt{rec.}} = \frac{A}{a'} = \frac{1}{2}\left(\frac{1}{2} + \left(\frac{\gamma}{L}\right)^2 + \frac{3}{2}\frac{\gamma}{L}\right)^{-1}\,, \tag{C.5}$$

$$\eta_{\texttt{rec.}} = \left(1 + 2\left(\frac{\mathrm{Kn}}{\upsilon}\right)^2 + 3\left(\frac{\mathrm{Kn}}{\upsilon}\right)\right)^{-1}\,, \tag{C.6}$$

where the Knudsen number based on wall thickness (γ) is $\upsilon = \lambda/\gamma$, or $\mathrm{Kn}/\upsilon = \gamma/L$.

C.2 Square cross sections

The above is repeated for square cross sections to give:

$$\eta_{\mathtt{squ.}} = \frac{A}{a'} = L^2 \left(L + \gamma\right)^{-2} , \tag{C.7}$$

$$\eta_{\mathtt{squ.}} = \left(1 + \frac{\gamma}{L}\right)^{-2} = \left(1 + \frac{\mathrm{Kn}}{\upsilon}\right)^{-2} . \tag{C.8}$$

C.3 Triangular cross sections

Finally, triangular cross sections are considered:

$$A = \frac{L^2}{\sqrt{3}} , \tag{C.9}$$

again, where L is the height of the triangular. The tessellated area is

$$a' = 3^{-1/2} \left(L + \frac{\gamma}{2} + \frac{\gamma}{\sqrt{3}}\right)^{-2} . \tag{C.10}$$

Therefore, the packing density is

$$\eta_{\mathtt{tri.}} = \frac{A}{a'} = \left(1 + \frac{\gamma}{2L} + \frac{\gamma}{\sqrt{3}L}\right)^{-2} , \tag{C.11}$$

$$\eta_{\mathtt{tri.}} = \left(1 + \frac{\mathrm{Kn}}{2\upsilon} + \frac{\mathrm{Kn}}{\sqrt{3}\upsilon}\right)^{-2} . \tag{C.12}$$

Bibliography

A. Abdulle, E. Weinan, B. Engquist, and E. Vanden-Eijnden. The heterogeneous multiscale method. *Acta Numerica*, 21:1–87, 2012.

R. K. Agarwal, K.-Y. Yun, and R. Balakrishnan. Beyond Navier-Stokes: Burnett equations for flows in the continuum-transition regime. *Physics of Fluids (1994-present)*, 13(10):3061–3085, 2001.

H. Akhlaghi and E. Roohi. Mass flow rate prediction of pressure-temperature-driven gas flows through micro/nanoscale channels. *Continuum Mechanics and Thermodynamics*, 26(1):67–78, 2014.

P. L. Bhatnagar, E. P. Gross, and M. Krook. A Model for Collision Processes in Gases. I. Small Amplitude Processes in Charged and Neutral One-Component Systems. *Physical Review*, 94:511–525, 1954.

G. A. Bird. Direct Simulation and the Boltzmann Equation. *Physics of Fluids (1958-1988)*, 13(11):2676–2681, 1970.

G. A. Bird. *Molecular Gas Dynamics and the Direct Simulation of Gas Flows*. Oxford Engineering Science Series 42. Clarendon Press, 1994. ISBN 978-0-19-856195-8.

G. A. Bird. *The DSMC Method*. CreateSpace Independent Publishing Platform, 2013. ISBN 978-1-49-211290-7.

L. Boltzmann. Weitere Studien über das Wärmegleichgewicht unter Gasmolekülen. *Sitzungsberichte der Akademie der Wissenschaften*, 66:275–370, 1872.

M. K. Borg, D. A. Lockerby, and J. M. Reese. A multiscale method for micro/nano flows of high aspect ratio. *Journal of Computational Physics*, 233:400–413, 2013a.

M. K. Borg, D. A. Lockerby, and J. M. Reese. A hybrid molecular-continuum simulation method for incompressible flows in micro/nanofluidic networks. *Microfluidics and Nanofluidics*, 15(4):541–557, 2013b.

J. P. Boyd. *Chebyshev and Fourier Spectral Methods*. Dover Publications, 2001. ISBN 978-0-48-641183-5.

D. Burnett. The Distribution of Molecular Velocities and the Mean Motion in a Non-Uniform Gas. *Proceedings of the London Mathematical Society*, s2-40(1): 382–435, 1936.

J. M. Burt and I. D. Boyd. Extension of a Multiscale Particle Scheme to Near-Equilibrium Viscous Flows. *AIAA Journal*, 47(6):1507–1517, 2009a.

J. M. Burt and I. D. Boyd. A hybrid particle approach for continuum and rarefied flow simulation. *Journal of Computational Physics*, 228(2):460–475, 2009b.

C. Cercignani and A. Daneri. Flow of a Rarefied Gas between Two Parallel Plates. *Journal of Applied Physics*, 34(12):3509–3513, 1963.

S. Chapman and T. G. Cowling. *The Mathematical Theory of Non-uniform Gases*. Cambridge University Press, 1991. ISBN 978-0-52-140844-8. An Account of the Kinetic Theory of Viscosity, Thermal Conduction and Diffusion in Gases.

C. de Beule, G. Wurm, T. Kelling, M. Küpper, T. Jankowski, and J. Teiser. The martian soil as a planetary gas pump. *Nature Physics*, 10(1):17–20, 2014.

J. de Ruiter, R. Lagraauw, D. van den Ende, and F. Mugele. Wettability-independent bouncing on flat surfaces mediated by thin air films. *Nature Physics*, 11(1):48–53, 2015.

T. Doi. Numerical analysis of the Poiseuille flow and the thermal transpiration of a rarefied gas through a pipe with a rectangular cross section based on the linearized Boltzmann equation for a hard sphere molecular gas. *Journal of Vacuum Science & Technology A*, 28(4):603–612, 2010.

W. E and X. Li. Analysis of the heterogeneous multiscale method for gas dynamics. *Methods and Applications of Analysis*, 11(4):557–572, 2004.

W. E, B. Engquist, X. Li, W. Ren, and E. Vanden-Eijnden. Heterogeneous multiscale methods: A review. *Communications in Computational Physics*, 2(3):367–450, 2007.

W. E, W. Ren, and E. Vanden-Eijnden. A general strategy for designing seamless multiscale methods. *Journal of Computational Physics*, 228(15):5437–5453, 2009.

D. Einzel, P. Panzer, and M. Liu. Boundary condition for fluid flow: Curved or rough surfaces. *Physical Review Letters*, 64:2269–2272, 1990.

C. Ericson. Chapter 3 - A Math and Geometry Primer. In *Real-Time Collision Detection*, The Morgan Kaufmann Series in Interactive 3D Technology, pages 23–73. Morgan Kaufmann, 2005. ISBN 978-1-55860-732-3.

M. Gad-el Hak. Flow Physics. In *MEMS: Introduction and Fundamentals*, The CRC Press Series in Mechanical and Aerospace Engineering, pages 4–1–4–36. CRC Press, 2005. ISBN 978-0-8493-9137-8.

A. L. Garcia and B. J. Alder. Generation of the Chapman-Enskog Distribution. *Journal of Computational Physics*, 140(1):66–70, 1998.

N. G. Hadjiconstantinou. Discussion of recent developments in hybrid atomistic-continuum methods for multiscale hydrodynamics. *Bulletin of the Polish Academy of Sciences: Technical Sciences*, 53(4):335–342, 2005.

N. G. Hadjiconstantinou, A. L. Garcia, M. Z. Bazant, and G. He. Statistical error in particle simulations of hydrodynamic phenomena. *Journal of Computational Physics*, 187(1):274–297, 2003.

N. G. Hadjiconstantinou, G. A. Radtke, and L. L. Baker. On Variance-Reduced Simulations of the Boltzmann Transport Equation for Small-Scale Heat Transfer Applications. *Journal of Heat Transfer*, 132(11):112401–112401, 2010.

D. B. Hash and H. A. Hassan. Assessment of schemes for coupling Monte Carlo and Navier-Stokes solution methods. *Journal of Thermophysics and Heat Transfer*, 10(2):242–249, 1996.

T. M. M. Homolle. Efficient particle methods for solving the Boltzmann equation. Master's thesis, Massachusetts Institute of Technology, 2007.

T. M. M. Homolle and N. G. Hadjiconstantinou. A low-variance deviational simulation Monte Carlo for the Boltzmann equation. *Journal of Computational Physics*, 226(2):2341–2358, 2007a.

T. M. M. Homolle and N. G. Hadjiconstantinou. Low-variance deviational simulation Monte Carlo. *Physics of Fluids (1994-present)*, 19(4), 2007b.

G. Karniadakis, A. Beskok, and N. Aluru. Thermal Effects in Microscales. In *Microflows and Nanoflows*, volume 29 of *Interdisciplinary Applied Mathematics*, pages 167–193. Springer New York, 2005. ISBN 978-0-387-22197-7.

T. W. Kenny, K. E. Goodson, J. G. Santiago, E. Wang, J.-M. Koo, L. Jiang, E. Pop, S. Sinha, L. Zhang, D. Fogg, S. Yao, R. Flynn, C.-H. Chang, and C. H. Hidrovo. Advanced Cooling Technologies for Microprocessors. *International Journal of High Speed Electronics and Systems*, 16(1):301–313, 2006.

D. A. Kessler, E. S. Oran, and C. R. Kaplan. Towards the development of a multiscale, multiphysics method for the simulation of rarefied gas flows. *Journal of Fluid Mechanics*, 661:262–293, 2010.

M. Knudsen. Die Gesetze der Molekularströmung und der inneren Reibungsströmung der Gase durch Röhren. *Annalen der Physik*, 333(1):75–130, 1909a.

M. Knudsen. Eine Revision der Gleichgewichtsbedingung der Gase. Thermische Molekularströmung. *Annalen der Physik*, 336(1):205–229, 1909b.

M. Knudsen. Thermischer Molekulardruck der Gase in Röhren. *Annalen der Physik*, 338(16):1435–1448, 1910.

J. M. Kolinski, L. Mahadevan, and S. M. Rubinstein. Drops can bounce from perfectly hydrophilic surfaces. *EPL (Europhysics Letters)*, 108(2):24001, 2014.

J. M. Kolinski, S. M. Rubinstein, S. Mandre, M. P. Brenner, D. A. Weitz, and L. Mahadevan. Skating on a Film of Air: Drops Impacting on a Surface. *Physical Review Letters*, 108:074503, 2012.

V. I. Kolobov, R. R. Arslanbekov, V. V. Aristov, A. A. Frolova, and S. A. Zabelok. Unified solver for rarefied and continuum flows with adaptive mesh and algorithm refinement. *Journal of Computational Physics*, 223(2):589–608, 2007.

J.-M. Koo, S. Im, L. Jiang, and K. E. Goodson. Integrated Microchannel Cooling for Three-Dimensional Electronic Circuit Architectures. *Journal of Heat Transfer*, 127(1):49–58, 2005.

P. Le Tallec and F. Mallinger. Coupling Boltzmann and NavierStokes Equations by Half Fluxes. *Journal of Computational Physics*, 136(1):51–67, 1997.

J. Liu, N. K. Gupta, K. D. Wise, Y. B. Gianchandani, and X. Fan. Demonstration of motionless Knudsen pump based micro-gas chromatography featuring microfabricated columns and on-column detectors. *Lab on a Chip*, 11:3487–3492, 2011.

D. A. Lockerby, J. M. Reese, D. R. Emerson, and R. W. Barber. Velocity boundary condition at solid walls in rarefied gas calculations. *Physical Review E*, 70:017303, 2004.

D. A. Lockerby, C. A. Duque-Daza, M. K. Borg, and J. M. Reese. Time-step coupling for hybrid simulations of multiscale flows. *Journal of Computational Physics*, 237: 344–365, 2013.

D. A. Lockerby, A. Patronis, M. K. Borg, and J. M. Reese. Asynchronous coupling of hybrid models for efficient simulation of multiscale systems. *Journal of Computational Physics*, 284:261–272, 2015.

S. K. Loyalka and S. A. Hamoodi. Poiseuille flow of a rarefied gas in a cylindrical tube: Solution of linearized Boltzmann equation. *Physics of Fluids A: Fluid Dynamics (1989-1993)*, 2(11):2061–2065, 1990.

S. McNamara and Y. B. Gianchandani. On-chip vacuum generated by a micromachined Knudsen pump. *Journal of Microelectromechanical Systems*, 14(4): 741–746, 2005.

A. B. Morris, P. L. Varghese, and D. B. Goldstein. Monte Carlo solution of the Boltzmann equation via a discrete velocity model. *Journal of Computational Physics*, 230(4):1265–1280, 2011.

C. Mouhot and L. Pareschi. Fast algorithms for computing the Boltzmann collision operator. *Mathematics of Computation*, 75:1833–1852, 2006.

E. P. Muntz, Y. Sone, K. Aoki, S. Vargo, and M. Young. Performance analysis and optimization considerations for a Knudsen compressor in transitional flow. *Journal of Vacuum Science & Technology A*, 20(1):214–224, 2002.

T. Ohwada. Higher Order Approximation Methods for the Boltzmann Equation. *Journal of Computational Physics*, 139(1):1–14, 1998.

A. Patronis and D. A. Lockerby. Multiscale simulation of non-isothermal microchannel gas flows. *Journal of Computational Physics*, 270:532–543, 2014.

A. Patronis, D. A. Lockerby, M. K. Borg, and J. M. Reese. Hybrid continuum-molecular modelling of multiscale internal gas flows. *Journal of Computational Physics*, 255:558–571, 2013.

P.-O. Persson. *Mesh Generation for Implicit Geometries*. PhD thesis, Massachusetts Institute of Technology, 2004.

G. A. Radtke. *Efficient simulation of molecular gas transport for micro- and nanoscale applications*. PhD thesis, Massachusetts Institute of Technology, 2011.

G. A. Radtke, N. G. Hadjiconstantinou, and W. Wagner. Low-noise Monte Carlo simulation of the variable hard sphere gas. *Physics of Fluids (1994-present)*, 23 (3), 2011.

G. A. Radtke, J.-P. M. Péraud, and N. G. Hadjiconstantinou. On efficient simulations of multiscale kinetic transport. *Philosophical Transactions of the Royal Society A: Mathematical, Physical and Engineering Sciences*, 371(1982), 2013.

J. M. Reese, M. A. Gallis, and D. A. Lockerby. New directions in fluid dynamics: non-equilibrium aerodynamic and microsystem flows. *Philosophical Transactions of the Royal Society of London A: Mathematical, Physical and Engineering Sciences*, 361(1813):2967–2988, 2003.

S. Reinecke and G. M. Kremer. Method of moments of Grad. *Physical Review A*, 42:815–820, 1990.

W. Ren and W. E. Heterogeneous multiscale method for the modeling of complex fluids and micro-fluidics. *Journal of Computational Physics*, 204(1):1–26, 2005.

O. Reynolds. On Certain Dimensional Properties of Matter in the Gaseous State. Part I. Experimental Researches on Thermal Transpiration of Gases through Porous Plates and on the Laws of Transpiration and Impulsion, Including an Experimental Proof That Gas is Not a Continuous Plenum. Part II. On an Extension of the Dynamical Theory of Gas, Which Includes the Stresses, Tangential and Normal, Caused by a Varying Condition of Gas, and Affords an Explanation of the Phenomena of Transpiration and Impulsion. *Philosophical Transactions of the Royal Society of London*, 170:727–845, 1879.

M. Rojas-Cárdenas, I. Graur, P. Perrier, and J. G. Méolans. Time-dependent experimental analysis of a thermal transpiration rarefied gas flow. *Physics of Fluids (1994-present)*, 25(7), 2013.

R. Roveda, D. B. Goldstein, and P. L. Varghese. Hybrid Euler/Particle Approach for Continuum/Rarefied Flows. *Journal of Spacecraft and Rockets*, 35(3):258–265, 1998.

C. Runge. Über empirische Funktionen und die Interpolation zwischen äquidistanten Ordinaten. *Zeitschrift für Mathematik und Physik*, 46:224–243, 1901.

L. Saint-Raymond. Introduction. In *Hydrodynamic Limits of the Boltzmann Equation*, volume 1971 of *Lecture Notes in Mathematics*, pages 1–11. Springer Berlin Heidelberg, 2009. ISBN 978-3-540-92846-1.

T. J. Scanlon, E. Roohi, C. White, M. Darbandi, and J. M. Reese. An open source, parallel DSMC code for rarefied gas flows in arbitrary geometries. *Computers & Fluids*, 39(10):2078–2089, 2010.

T. E. Schwartzentruber, L. C. Scalabrin, and B. I. D. A modular particle-continuum numerical method for hypersonic non-equilibrium gas flows. *Journal of Computational Physics*, 225(1):1159–1174, 2007.

E. M. Shakhov. Generalization of the Krook kinetic relaxation equation. *Fluid Dynamics*, 3(5):95–96, 1968.

F. Sharipov. Non-isothermal gas flow through rectangular microchannels. *Journal of Micromechanics and Microengineering*, 9(4):394, 1999.

M. S. Shavaliyev. Super-Burnett corrections to the stress tensor and the heat flux in a gas of Maxwellian molecules. *Journal of Applied Mathematics and Mechanics*, 57(3):573–576, 1993.

B. Shizgal. Polynomial Basis Functions and Quadratures. In *Spectral Methods in Chemistry and Physics*, Scientific Computation, pages 29–107. Springer Netherlands, 2015. ISBN 978-94-017-9453-4.

Y. Sone. Flows Induced by Temperature Fields in a Rarefied Gas and their Ghost Effect on the Behavior of a Gas in the Continuum Limit. *Annual Review of Fluid Mechanics*, 32(1):779–811, 2000.

Y. Sone. *Molecular Gas Dynamics*. Modeling and Simulation in Science, Engineering and Technology. Birkhäuser Basel, 2007. ISBN 978-0-8176-4573-1. Theory, Techniques, and Applications.

D. Stephenson, D. A. Lockerby, M. K. Borg, and J. M. Reese. Multiscale simulation of nanofluidic networks of arbitrary complexity. *Microfluidics and Nanofluidics*, pages 1–18, 2014.

H. Struchtrup. Introduction. In *Macroscopic Transport Equations for Rarefied Gas Flows*, Interaction of Mechanics and Mathematics, pages 1–13. Springer Berlin Heidelberg, 2005. ISBN 978-3-540-24542-1.

A. Z. Szeri. Gas Lubrication. In *Fluid Film Lubrication*, pages 392–408. Cambridge University Press, 1998. ISBN 978-0-511-62640-1.

S. Takata, H. Sugimoto, and S. Kosuge. Gas separation by means of the Knudsen compressor. *European Journal of Mechanics - B/Fluids*, 26(2):155–181, 2007.

S. Tiwari and A. Klar. An adaptive domain decomposition procedure for Boltzmann and Euler equations. *Journal of Computational and Applied Mathematics*, 90(2): 223–237, 1998.

W. Wagner. A convergence proof for Bird's direct simulation Monte Carlo method for the Boltzmann equation. *Journal of Statistical Physics*, 66(3-4):1011–1044, 1992.

J. A. C. Weideman. Numerical Integration of Periodic Functions: A Few Examples. *The American Mathematical Monthly*, 109(1):21–36, 2002.

C. White, C. Colombo, T. J. Scanlon, C. R. McInnes, and J. M. Reese. Rarefied gas effects on the aerodynamics of high area-to-mass ratio spacecraft in orbit. *Advances in Space Research*, 51(11):2112–2124, 2013.

H. S. Wijesinghe, R. D. Hornung, A. L. Garcia, and N. G. Hadjiconstantinou. Three-dimensional Hybrid Continuum-Atomistic Simulations For Multiscale Hydrodynamics. *Journal of Fluids Engineering*, 126(5):768–777, 2004.

H. S. Wijesinghe and N. G. Hadjiconstantinou. Discussion of Hybrid Atomistic-Continuum Methods for Multiscale Hydrodynamics. *International Journal for Multiscale Computational Engineering*, 2(2), 2004.

C. G. Wilson and Y. B. Gianchandani. Silicon micromachining using in situ DC microplasmas. *Journal of Microelectromechanical Systems*, 10(1):50–54, 2001.

J. S. Wu, Y. Y. Lian, G. Cheng, R. P. Koomullil, and K. C. Tseng. Development and verification of a coupled DSMC-NS scheme using unstructured mesh. *Journal of Computational Physics*, 219(2):579–607, 2006.

L. Wu, C. White, T. J. Scanlon, J. M. Reese, and Y. Zhang. Deterministic numerical solutions of the Boltzmann equation using the fast spectral method. *Journal of Computational Physics*, 250:27–52, 2013.

L. Wu, J. M. Reese, and Y. Zhang. Solving the Boltzmann equation deterministically by the fast spectral method: application to gas microflows. *Journal of Fluid Mechanics*, 746:53–84, 2014.

L. Wu, C. White, T. J. Scanlon, J. M. Reese, and Y. Zhang. A kinetic model of the Boltzmann equation for non-vibrating polyatomic gases. *Journal of Fluid Mechanics*, 763:24–50, 2015.

M. Young, E. P. Muntz, and S. E. Vargo. Microscale Vacuum Pumps. In *MEMS: Applications*, The CRC Press Series in Mechanical and Aerospace Engineering, pages 8–1–8–29. CRC Press, 2005. ISBN 978-0-8493-9139-2.

S. Yuhong, R. W. Barber, and D. R. Emerson. Inverted velocity profiles in rarefied cylindrical Couette gas flow and the impact of the accommodation coefficient. *Physics of Fluids (1994-present)*, 17(4), 2005.